VERLAG DER TECHNISCHEN UNIVERSITÄT GRAZ

Christoph Feichtinger

Racebike Dynamics

Aerodynamic Motorbike Model for the Dynamic Riding Limit on a Racetrack

FTG 9

MONOGRAPHIC SERIES TU GRAZ
REIHE FAHRZEUGTECHNIK

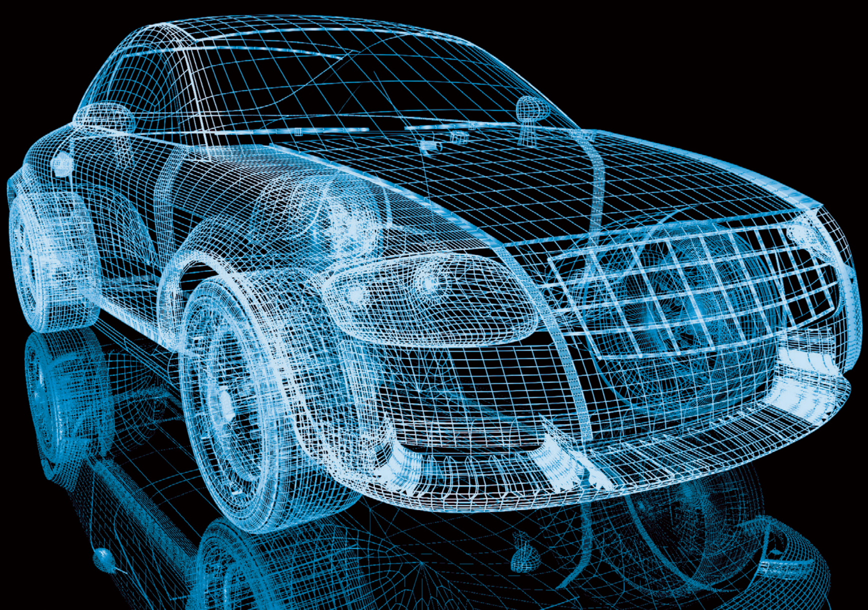

Christoph Feichtinger

Racebike Dynamics

Aerodynamic Motorbike Model for the Dynamic Riding Limit on a Racetrack

Monographic Series TU Graz

Reihe Fahrzeugtechnik

Series Editor:

Institute of Automotive Engineering

Monographic Series TU Graz

Reihe Fahrzeugtechnik Volume 9

Christoph Feichtinger

Racebike Dynamics

Aerodynamic Motorbike Model for the Dynamic Riding Limit on a Racetrack

---

This work is based on the dissertation *"Aerodynamic Motorbike Model for the Dynamic Riding Limit on a Racetrack"*, presented at Graz University of Technology, Institute of Automotive Engineering in 2021.

Supervision / Assessment:

Peter Fischer (Graz University of Technology)

Edoardo Sabbioni (Politecnico di Milano)

Cover photo	'concept car' by ArchMen (modified) Fotolia / Adobe Stock
Cover layout	Verlag der Technischen Universität Graz
Print	DATAFORM Media Ges.m.b.H.

www.tugraz-verlag.at

Print
ISBN 978-3-85125-860-8

E-Book
978-3-85125-861-5
DOI 10.3217/978-3-85125-860-8

"Data without a model is just noise"

– *unknown* –

Preface

This thesis is the conclusion of a long journey which has started with an idea in 2014 before joining a MotoGP world championship team. The need for a deeper and more accurate understanding of motorcycle aerodynamics has been confirmed more than once throughout the years.

Nonetheless, exclusively the enthusiastic support of my doctor father, Univ.-Prof. Dipl.-Ing. Dr.techn. Peter Fischer made this work possible. His character and professional competence have been a great asset to my personal and professional development over the last few years. I would like to express my sincere thanks to Peter Fischer for this.

At the same time I would like to thank Prof. Edoardo Sabbioni who agreed to do a second review of my work.

Throughout the writing of this dissertation I have received a great deal of support and assistance from the whole Institute of Automotive Engineering. In particular I would like to thank Univ.-Prof.i.R. Dr. Wolfgang Hirschberg, Assoc.Prof. Dr. Arno Eichberger, Assoc.Prof. Dr. Cornelia Lex and Dipl.-Ing. Dr. Andreas Hackl.

My special thanks goes to Alex Baumgärtel, owner and managing director of KALEX Engineering. Together with Rainhard Mandl, he supported the present thesis with measurement data of a Moto2 world championship race. Only then the work became complete and the developed methods could be applied to real measurement data. Many, many thanks therefore!

My greatest thanks go to my family, my mother and my father, who have made all this possible and have always supported me in all decisions.

Finally, I could not have completed this dissertation without the support of my Elke, who always provided me the best with advice and action. Especially in critical and difficult situations – *LGF*.

Graz in July 2021,

Christoph Simon Feichtinger

Abstract

The aerodynamics of a racebike is a relatively young field in professional motorcycle racing and in the field of aerodynamics itself. In recent years, aerodynamics has become more and more the focus of racing factories.

In motorcycle racing the rider plays an important role in terms of its riding style – the relative position of the rider in different riding situations on the racetrack. From an engineering point of view the riding style has a huge impact on the center of gravity position of the overall racebike and rider system. The different rider positions also have a strong impact on the aerodynamics of the overall racebike and rider system.

Additional changes during a race or test day due to external influences or internal signs of wear and tear must be considered – this applies to the rider as well as to components of the motorbike.

For a proper development process, a solid data analysis of the individual influences is enormously important. Data analysis needs models to understand and evaluate individual effects. The aim of the present work is to show a new approach to assess aerodynamic characteristics of a racebike and rider system for real-world racetrack riding situations. The approach is shown for race measurement data of a Moto2 world championship race.

A motorcycle model was built to replicate the influences of the tire, the aerodynamics and the dynamics of the rider's movement at the dynamic riding limits of the vehicle. The model was built as a multi-body system using Jourdain's principle. All transformation matrices as well as position and velocity vectors of the individual bodies were solved analytically. Thus the model computes very fast.

The unknown influence of the aerodynamics and the rider dynamics on the dynamic riding limit was determined by segmenting an average race lap from the measurements using the multibody model. This means that changes to the racebike can now be objectively evaluated for specific riders and specific racetracks.

With the very fast calculating, specific ”motorcycle-dynamic-riding-limit-model” a tool has been developed, which can be used in the racing development process – which differs significantly from series vehicle development. The tool can be used to support from pre-development to single race days as well as to analyse the motorcycle development, ongoing adaptations and setup changes.

Keywords: Aerodynamics, Racing, Mechanics of Solid Bodies, Jourdains Principle, Operational Domain, Tire Model, Real World Racetrack Scenarios, Race Track Validation

Kurzfassung

Die Aerodynamik eines Rennmotorrades ist ein relativ junges Feld im professionellen Motorradrennsport und im Bereich der Aerodynamik selbst. In den letzten Jahren ist die Aerodynamik mehr und mehr in den Fokus der Rennsportwerke gerückt.

Im Motorradrennsport spielt der Fahrer in Bezug auf seinen Fahrstil eine wichtige Rolle – die relative Position des Fahrers in verschiedenen Fahrsituationen auf der Rennstrecke. Aus technischer Sicht hat der Fahrstil einen großen Einfluss auf die Schwerpunktlage des Gesamtsystems Rennmotorrad und Fahrer. Die unterschiedlichen Fahrerpositionen haben ausserdem einen starken Einfluss auf die Aerodynamik des Gesamtsystems Rennmotorrad und Fahrer.

Zusätzliche Veränderungen während eines Renn- oder Testtages durch äußere Einflüsse oder Verschleißerscheinungen müssen berücksichtigt werden – das gilt für den Fahrer ebenso wie für Komponenten des Motorrads.

Für einen strukturierten Entwicklungsprozess ist eine solide Datenanalyse der einzelnen Einflüsse enorm wichtig. Die Datenanalyse benötigt Modelle, um die einzelnen Einflüsse zu verstehen und zu bewerten. Ziel der vorliegenden Arbeit ist es, einen neuen Ansatz zur Bewertung der aerodynamischen Eigenschaften des Systems Rennmotorrad und Fahrer für reale Fahrsituationen auf der Rennstrecke aufzuzeigen. Der Ansatz wird für Messdaten eines Moto2-Weltmeisterschaftslaufs gezeigt.

Ein Motorradmodell wurde gebaut, um die Einflüsse des Reifens, der Aerodynamik und der Bewegungsdynamik des Fahrers im fahrdynamischen Grenzbereich nachzubilden. Das Modell wurde als Mehrkörpersystem nach dem Jourdainschen Prinzip aufgebaut. Alle Transformationsmatrizen sowie die Positions- und Geschwindigkeitsvektoren der einzelnen Körper wurden analytisch gelöst. Dadurch rechnet das Modell sehr schnell.

Der unbekannte Einfluss der Aerodynamik und der Fahrerdynamik im Fahrdynamischen Grenzbereich wurde aus dem Mehrkörpermodell ermittelt, indem eine durchschnittliche Rennrunde aus den Messungen segmentiert wurde. Damit können Änderungen am Rennmotorrad nun objektiv für bestimmte Fahrer und bestimmte Rennstrecken bewertet werden.

Mit dem sehr schnell rechnenden, spezifischen "Motorrad-Grenzbereich-Modell" wurde ein Werkzeug entwickelt, das im Rennsport-Entwicklungsprozess – der sich deutlich von der Serienfahrzeugentwicklung unterscheidet – eingesetzt werden kann. Das Werkzeug kann von der Vorentwicklung bis zu einzelnen Renntagen sowie zur Analyse der Motorradentwicklung, laufenden Anpassungen und Setup-Änderungen eingesetzt werden.

Keywords: Aerodynamik, Rennsport, Festkörpermechanik, Prinzip von Jourdain, Einsatzumgebung, Reifenmodell, reale Rennstreckenszenarien, Rennstreckenvalidierung

Contents

Abbreviations

AC	Aerodynamic Center
AIM	Aerodynamic-Inertia-Mass Model
bhp	Brake Horsepower
CAD	Computer Aided Design
cc	Cubiccentimeter
CFD	Computational Fluid Dynamics
COG	Center of Gravity
DAE	Differential-Algebraic Equations
ECU	Electronic Control Unit
FIM	Fédération Internationale Motocycliste
IMU	Inertial Measurement Unit
RANS	Reynolds-Averaged Navier-Stokes
TT	Tourist Trophy

Symbols

Latin Symbols:

$\mathbf{A}$	Transformation Matrix
$\mathbf{a}$	Acceleration Vector
A_x	Projected Area in m^2
c	Speed of Propagation of Sound in m/s
c_D	Aerodynamic Drag Coefficient
c_L	Aerodynamic Lift Coefficient
$c_{\mathcal{L}}$	Aerodynamic Roll Moment Coefficient
$c_{\mathcal{M}}$	Aerodynamic Pitch Moment Coefficient
$c_{\mathcal{N}}$	Aerodynamic Yaw Moment Coefficient
c_Y	Aerodynamic Side Force Coefficient
d_i	Generalized Displacement
D	Aerodynamic Drag Force in N
$\mathbf{e}$	Unit Vector, Euler Parameters
F_{df}	Friction Force in N
F_{dp}	Pressure Force in N
f_i	Body Force per Unit Mass into the Direction x_i in N/kg
f_v	Vortex Shedding Frequency in Hz
g	Gravitational Acceleration in m/s^2
$\mathbf{G}$	Quaternion Transformation Matrix
$\mathbf{J}$	Jacobi Matrix
k_{turb}	Turbulent Kinetic Energy in m^2/s^2
L	Aerodynamic Lift Force in N
$\mathbf{L}$	Quaternion Transformation Matrix
$\mathcal{L}_{turb}$	Turbulent Length Scale in m
M	Mach Number
m	Mass in kg
$\mathbf{M}$	Generalized Mass Matrix
M	Moment, Torque in Nm
$\mathcal{L}$	Aerodynamic Roll Moment in Nm
$\mathcal{M}$	Aerodynamic Pitch Moment in Nm

$\mathcal{N}$	Aerodynamic Yaw Moment in Nm
p	Pressure in Pa
q_{dyn}	Dynamic Pressure in Pa
$\mathbf{q}$	Generalized Force Vector
q	Quaternion Number
r_c	Turning Radius in m
Re	Reynolds Number
$\mathbf{r}$	Position Vector
Sr	Strouhal Number
s_x	Tire Slip in x-Direction
s_y	Tire Slip in y-Direction
T	Temperature in K
t	Time in s
$\mathbf{T}$	Inertia Tensor
Tu	Turbulence Intensity
$\mathcal{U}_{turb}$	Turbulent Velocity Scale in m/s
u, v, w	Velocity Components in x-y-z Direction in m/s
v	Speed in m/s
$\mathbf{v}$	Velocity Vector
Y	Aerodynamic Side Force in N
$\mathbf{y}$	Generalized Coordinate Vector
$\mathbf{z}$	Generalized Velocity Vector

Greek Symbols:

α_{us}	Upstream Flow Angle of Attack in rad
β_{us}	Upstream Incident Flow Angle in rad
χ	Lean Angle Speed Derivative in $rad\,s/m$
δ	Steering Angle in rad
∂	Partial Derivative
ε	Turbulent Energy Dissipation in m^2/s^3
κ	Steering Head Angle in rad
λ	Sideslip Angle in °
μ_{lat}	Lateral Tire Friction Coefficient
μ_{long}	Longitudinal Tire Friction Coefficient
ν	Kinematic Viscosity in m^2/s
$\boldsymbol{\omega}$	Angular Velocity Vector in $1/s$
ω	Rotational Wheel Speed in $1/s$
ω_{turb}	Characteristic Frequency of a Flow Separation in $1/s$
φ	Racebike Lean Angle in rad

ψ	Yaw Angle in rad
ρ	Air Density in kg/m^3
τ_{ij}	Viscous Stress Tensor in Pa
τ_w	Wall Shear Stress in Pa
Θ	Inertia Moment in $kg\,m^2$
θ	Pitch Angle in rad
ξ	Spine Curve of the Road Trajectory

Indices:

act	Active
$aero$	Aerodynamic
app	Apparent
B	Arbitrary Fluid Element
b	Body Axis System
C	Chassis
G	Upper Front Assembly
$gyro$	Gyroscopic
H	Rear Wheel
i	General Index
$inert$	Inertial
I	Inertial Axis System
∞	Upstream
k	Arbitrary Particle
lat	Lateral
L	Lower Front Assembly
$long$	Longitudinal
$meas$	Measurement
p	Road Patch Axis System
ref	Reference Measure
SL	Sea Level
$susp$	Suspension
S	Swingarm
$tors$	Torsional
us	Upstream
V	Front Wheel
wh	Wheel Axis System
w	Wind Axis System

Notations:

$\bar{q}$	Averaged Value of Quantity q
$\mathbf{q}$	Vector Representation of Quantity q
$\dot{q}$	Time Derivative of Quantity q with Respect to Time
$\hat{q}$	Normalized Value of Quantity q
$\lvert q \rvert$	Magnitude of Quantity q
$q\prime$	Fluctuating Value of Quantity q

Chapter 1

Introduction

> *"If everything seems under control, you're just not going fast enough."*
>
> Mario Andretti

The very famous statement of Mario Andretti [39] counts for all types of race vehicles, whether with two, four or more wheels. The *Ride* on the physical limits of man and machine distinguishes a racebike from a roadbike. The roadbike is of course also designed for maximum riding performance and riding pleasure, but also must consider riding comfort and the compliance with road traffic regulations. The introductory and some other general sections refer to previous work by the author [21] and [23].

1.1 A Racebike on the Racetrack

A racebike is made for the competition against others. The crucial criteria for success are the fastest time or the crossing of the finish line in front of the competitors. On the way to the success, athletes and engineers must improve their own physical performance and the performance of the bike, respectively. The use of a racebike on a racetrack is a complex combination of bike and rider movements in a wide lean angle and speed range. Therefore, the riders must understand the functionality and technology of the bike, the engineers have to understand the needs and demands of the riders. Beside working on their physical fitness, professional race riders also must work on their optimum racing line, on their race strategy and on their mental strength.

Race engineers and racebike factories must understand every little detail of the racebike and its influence on the performance. This is the mandatory requirement to improve the performance of the racebike. In this context it is important to understand that every rider has its own riding style. Two different riders with different riding styles could do the same lap time with different setups of the same racebike. This means that there is no golden rule of how a motorbike must be designed and operated to reach the fastest lap time. Nevertheless, there are some general design guidelines how a typical racebike is realized, or how it is realized currently. The way to success is to understand the specific rider and racebike combination in every detail. Only then both can show their best performance.

Optimizing every little detail on a racebike means intensive detailed work in simulation, on test benches and on test- and racetracks. Every little detail, whether if it is a physical part, a specific mechanical setting or an electronic setting, has to be tested and has to show its benefit if it should be used in the final racebike specification. In an ideal world every small detail should be tested independent of all the others, resulting in a clear outcome about the performance from a perspective of time or speed. Fig. 1.1 shows recordings of a Moto2 lap section for the bike speed, the lean angle and the bike acceleration signal. It shows the permanent change of the lean angle φ_{bike} reaching maximum lean angle values of up to 56°. Assuming a point contact between the road and the tire, without any tire geometry shape and the center of gravity in the same location as the center of the apparent forces, and constant speed, the lean angle can be calculated using the following mathematical description

$$\tan\varphi = \mu_{lat}\,, \tag{1.1}$$

where φ is the lean angle and μ_{lat} is the required lateral tire friction coefficient. The equation shows that racebike tires must have road tire friction coefficients of greater than 1 to realize lean angles of up to 56°. The recordings from Fig. 1.1 show, that the racebike is operated at the physical limit from a lateral point of view. The same counts for the longitudinal dynamic of the racebike. The acceleration signal a_{bike} shows acceleration peaks of up to $10\,m/s^2$ and deceleration peaks of $-10\,m/s^2$.

The simplified relation between the representative acceleration of the racebike a_{bike} and the required longitudinal road tire friction coefficient μ_{long} is denoted as

$$a_{bike} = \mu_{long}\, g\,, \tag{1.2}$$

with g as the gravitational acceleration which is $\approx 9.81\,m/s^2$. Using Eq. 1.2 the longitudinal road tire friction coefficient for acceleration and braking is around 1, indicating the physical limit of a racebike in longitudinal direction. Typical for racebike track data is, that there are nearly no steady-state situations with constant speed or constant lean angle. The racebike is in permanent, highly dynamic movement. In simulation or on test benches the conditions are normally set constant to get reproducible results. Fig. 1.1 shows a horizontal line with a constant wind tunnel speed of 60 m/s. A wind tunnel is one of the common tools for aerodynamic racebike development, as it allows to assess the effect of single changes. In Fig. 1.1 there are five points of the speed signal intersecting the racetrack data and the constant wind tunnel speed. All five points indicate different riding situations with totally different rider positions on the racebike. This shows the importance of a holistic development approach which uses all tools available to evaluate racebike modifications and assess their influence on the performance.

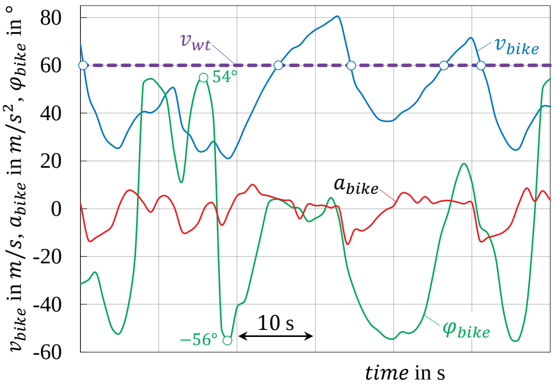

Figure 1.1: Racetrack data with identification of longitudinal and lateral riding limits. The figure shows also a typical, constant wind tunnel speed of 60 m/s *and the intersecting points with the bike speed measurement signal.*

Testing on racetracks is mandatory as it is the only place where the rider can operate the racebike in its real operational domain. Simulation and test benches have advantages for single functionalities or subassemblies of the racebike, but they cannot replace a real racetrack test. Tests on racetracks have a multitude of additional challenges. The first challenge is the permanently changing environmental conditions on a racetrack. Taking a typical track test day, like shown in Fig. 1.2, there are a lot of different influences which change permanently during one day. A big group of them are influenced by the weather and the time of day. The environmental conditions include the ambient temperature, the humidity, the air pressure, and the prevailing wind.

They are normally recorded at one point on the racetrack by a stationary weather station. One measurement point is not representative for the environmental conditions on the racetrack. Especially the wind can be completely different on different points on the racetrack due to the architecture of the racetrack. Additionally, other riders on the racetrack have an influence on the wind field in front of the racebike as well. Regardless of what is being tested, the boundary conditions are never the same at two different times. To still get a valid result of the tested configurations the single sensitivities of the changing environmental conditions must be known. The approach of the work is to combine all measured data of a racebike and the environmental conditions, combine them with a racebike model and derive describable riding situations for the holistic system. A typical riding situation could be for example the acceleration out of a corner on a long straight until reaching the breaking point.

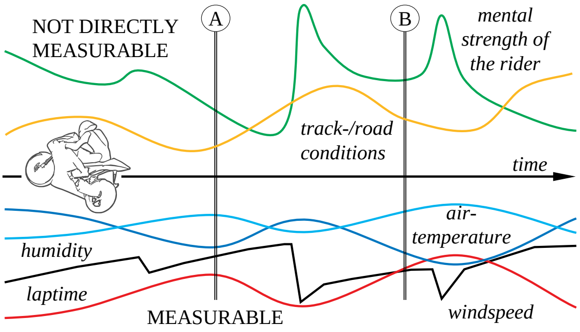

Figure 1.2: Typical track test day (by Christoph Feichtinger – own work).

1.2 Aerodynamics of the Racebike and the Rider

Within the present work the focus will be on the interaction of riding and aerodynamics of the racebike and the rider. Aerodynamics is a discipline of dynamics that deals with the motion of air and other gaseous fluids and with the forces acting on bodies in motion relative to such fluids [42]. There are different characteristics for the motion of air as well as for the motion of these bodies. The combination of different air and body motion characteristics lead to complex cases, like a moving racebike in windy on-track conditions.

The numerical modelling or measurement of such complex cases is a major challenge for engineers in motorbike, cycling and various sports industries. They all want to develop products to increase efficiency in terms of time (lap time, segment time) or speed (top speed, acceleration). The best known representatives of aerodynamics in terms of efficiency are the drag force and the drag coefficient

[51]. Additional aerodynamic characteristics are lift and side forces. Depending on where they act on the body the full aerodynamic characteristics need the description of the resulting aerodynamic acting point, hereinafter called the aerodynamic center AC. The aerodynamic center is the point where the total sum of the pressure and viscous forces acts on the body. Depending on the ratio of pressure to viscous forces the aerodynamic center is the point where the total sum of flow field forces acts on a body.

Alternatively, an artificial aerodynamic moment reference point, hereinafter called the moment reference point *M0*, could be chosen in a convenient place on the body of interest. The usage of the moment reference point requires the specification of three acting moments as representative of the drag, lift and side force with respect to the lever between the moment reference point and the aerodynamic center. Fig. 1.3 shows a typical position of both characteristic points. Grün et al. [27] used the mid-wheel base at ground level as moment reference point, which is conventionally used for cars. Within the present work an alternative reference point in the pivot point of the rear wheel swing arm is chosen, as it has less movement with respect to the large range of bike pitch and roll movements. The conventional, car reference point on the ground level is completely outside of the racebike geometry for lean angle cases. Modern racebikes can reach lean angles of up to 65°. The third reference point in terms of aerodynamics is the upstream reference point. This point is mandatory for the measurement and evaluation of the upstream flow conditions. The measurements in the upstream reference point are required for the input values of numerical flow simulations as well as for the load cases in the wind tunnel and the validity criteria for on-road tests and validations.

On real racebikes the upstream reference point can be for example the ram-air intake or additionally mounted flow probes in the front area of the racebike. Depending on the field of application the aerodynamic forces and moments are acting as a resistance or a thrust force. For a car or a motorbike, the drag force, which is acting against the direction of movement, by definition, is a pure resistance force, while for a sailing boat the vector sum of side force and drag acting in the direction of movement is the only thrust force driving the boat. Therefore, the aerodynamic models are classified regarding to (1) the body motion itself, (2) a gust field, in generalized form the environmental wind conditions and (3) a body deformation, e.g., in the form of a waving sail.

Body Motion ($\boldsymbol{v}_{bike}$, $\boldsymbol{\omega}_{bike}$) The body motion itself covers a riding situation without any wind. This case hardly ever occurs. Nevertheless, even a ride in completely windless environment can generate a dynamic wake area by the physics of the aerodynamic flow field. In this case the wake is a gust field for the following

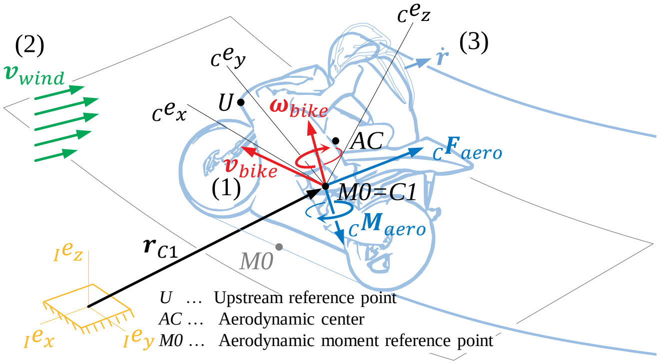

Figure 1.3: The operational domain of a racebike showing the aerodynamic model classification components (1) body motion, (2) gust field and (3) body deformation (by Christoph Feichtinger – own work).

riders.

Gust Field ($\boldsymbol{v}_{wind}$) The gust field represents all kinds of wind conditions which occur. Depending on the operational domain the gust field is a combination of environmental wind effects and a gust field induced by other road users or roadside obstacles. This leads to a gust field defined by different wind speeds, wind directions and turbulence levels. A test in a wind tunnel or a numerical flow simulation is a special case of a gust field, where the test body under investigation is stationary while the wind is blown against the test body.

Body Deformation ($\dot{\boldsymbol{r}}$) The body deformation is divided into a stiff and a flexible component. The stiff body deformation for its part covers all movements of internal elements like suspension and steering components, the wheels, and the human rider. The flexible part considers elastic movements of add-on parts like the fairing, high-frequency helmet movements or the clothing of the rider which is in permanent contact with the air in motion.

The above defined classification of aerodynamic models covers all types of tools like numerical flow simulations, wind tunnel tests and racetrack tests. Actual aerodynamic models cover mainly single criteria for varying characteristics. For example, incident flow angles at a constant oncoming wind speed for a fixed body orientation measured in a wind tunnel test. For the variation of a single criterion, this is quite easy. If a second criterion, like the body orientation is included in the aerodynamic model, the input is already a two-dimensional matrix. If all the input criteria would have a linear effect on the aerodynamic forces and moments acting on the body, a variety of different criteria would be no problem as they could be easily added by the principle of superposition. Unfortunately, aerodynamic effects are anything but linear. Even the drag coefficient for a bluff body like a car or a truck has a non-linear characteristic against the oncoming incident flow angle. If the aerodynamic models are extended by additional input parameters like the pitch angle or the driving speed, the combination of the single effects within the model needs special calculations and interpolations between the single characteristics. The effort to build and parameterize such kind of models is very high, as it needs the measurement and prediction of single effects and a model validation of the combined effects.

1.3 Research Aims

The research aim of the present work are tailored aerodynamic models. The models should be derived for defined riding situations at defined racetrack segments. Therefore, the tailored aerodynamic models must cover different complexities like

- the relative racebike positions on the racetrack and
- the relative rider positions on the racebike.

The focus of the present work is on a generalized aerodynamic drag model, where the lift and side force as well as the three aerodynamic moments are not neglected.

It is not a goal of the present work to develop new computational fluid dynamic models. It is also not planned to split the components of the generalized aerodynamic models into a pressure, frictional, induced and interference part.

The present work aims to improve and simplify the handling and understanding of complex body movements of a racebike with the involvement of aerodynamics.

Although motorsport is not the most important and sustainable thing in the world, in motorsport people still compete with the aim of winning. This is pushing athletes and engineers to peak performances. Therefore, motorsport applications are still well suited to test new developments and show their full potential. A faster motorcycle will not solve basic human problems, but a better understanding of real-world aerodynamics can, in the long term, contribute to increase the efficiency of private transport.

Chapter 2

State of the Art

The state of the art gives a review on motorcycle racing with the evolvement of racetracks and racebikes. The chapter gives an overview of motorsports aerodynamics with special focus on racebike aerodynamics. Finally, aerodynamic development tools and methodologies are presented.

2.1 Motorcycle Racing

There are many different types of motorcycle racing. The main types are road racing, motocross, rally, trials, drag racing, ice racing, hill climbs and sidecars. Road races are held on specially built racetracks or closed off road courses. In the early beginnings of motorcycle racing specially built racetracks were not existing. In 1904 the Fédération Internationale du Motocyclisme (renamed the Fédération Internationale Motocycliste [FIM] in 1949) created the international cup, uniting five nations: Austria, Denmark, France, Germany, and Britain (see Encyclopaedia Britannica [59]). The races were held under the name Tourist Trophy, hereinafter called TT. The first TT race took place in 1907 on the *Isle of Man*. After the first world war many new road racing courses were defined and tourist trophies were held all over the world. One of them was the Dutch Tourist Trophy in Assen. The different racetrack courses of the *Dutch TT* are shown in Fig. 2.1.

The history of the *Dutch TT* started 1925 with a 28.4 km long street circuit in the shape of a triangle between the towns of Borger, Schoonloo and Grolloo. From 1926 the races were held on a 16.536 km rectangular shaped street circuit through the towns of De Haar, Hooghalen, Laaghalen and Laaghalerveen. In 1955, a new 7.705 km circuit was created which still used public roads but more closely resembled a modern racetrack. From 1984 on the racetrack was again shortened to a track length of 6.100 km. In 1992, the racetrack became a permanent enclosed circuit. Since the last track layout change in 2006 the Dutch TT is held on the

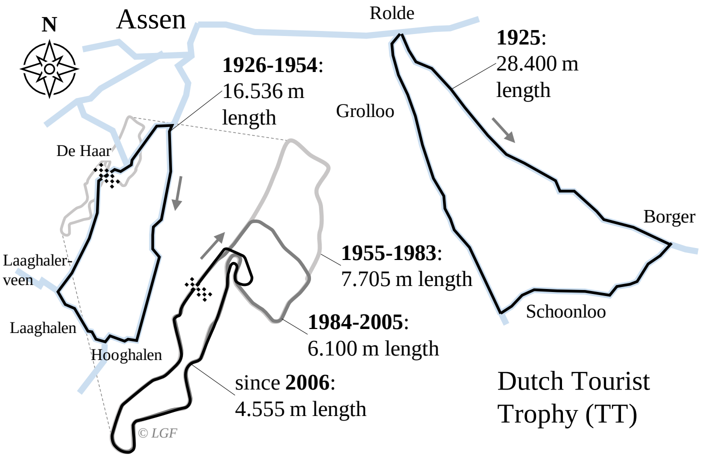

Figure 2.1: Different race track courses of the Dutch Tourist Trophy (by Christoph Feichtinger – own work).

4.555 km long racetrack. The evolvement of the racetrack in Assen is a good indicator of the increasing requirements to safety of the Motorcycle Federation FIM. Motorcycle Grand Prix are nowadays exclusively held on closed road racetracks.

The most famous public road races on which people are still racing today are the *North West 200* or the *Isle of Man*. The death statistics between public road races and races on closed road racetracks show two major things. First, that motorcycle racing is still very dangerous and second, that nearly double the people have died on public road racecourses in comparison to closed racetracks during official races.

Grand Prix Motorcycle Racing Grand Prix Motorcycle Racing marks the premier class of motorcycle road racing events with purpose-built racing machines, mainly prototypes. The premier class is split into three divisions: MotoGP, Moto2 and Moto3. All classes use four-stroke engines with a limited engine displacement of 1000 cc (cubiccentimeter), 765 cc and 250 cc, respectively. The most successful rider in Grand Prix history to date (2021) is Giacomo Agostini with 15 titles and 122 race wins. In the top-flight series, Agostini holds the title record with eight, followed by active riders Valentino Rossi with seven and Marc Márquez with six. The early years of Grand Prix racing saw several races at each event for various classes. The classes were based on engine size, ranging from 50 cc up to 500 cc, and extra classes for sidecars. Up till the end of the 1960s four-stroke engines dominated

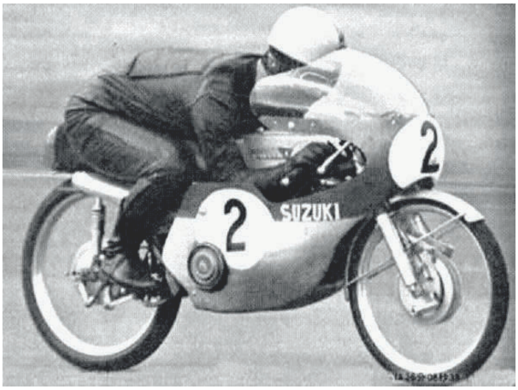

Figure 2.2: The 1967 Suzuki 50 cc, 14 speed Grand Prix racebike 'Suzuki RK67'.

in all classes. In the late 1960s two-stroke engines began to take over the lead due to advances in engine design and technology. The technological race has produced several amazing developments like the Suzuki RK67, a 50 cc 14-speed racebike, shown in Fig. 2.2. Therefore, in 1969 the FIM introduced new rules, restricting all classes to six gears and to a maximum number of cylinders. This led to the exit of numerous factory teams. Until the re-entry of Yamaha and Suzuki in 1973 and 1974, MV Augusta was the only remaining factory team in the premier class of Motorcycle Grand Prix racing. Giacomo Agostini won seven consecutive 500 cc championships with MV Augusta in that Period. Over the next years the smaller classes were sorted out or replaced by new classes. The top class of Grand Prix racing allowed a maximum displacement of 500 cc between the mid-1970s through 2001, regardless of whether the engine was a two-stroke or a four-stroke engine. Consequently, all championship winning racebikes were two-strokes in this period. In 2002 the rules change to ban two-stroke engines in the premier class, while the smaller classes still allowed two-strokes with 125 cc and 250 cc, respectively. The year 2010 marks the last major rule change, resulting in the actual race classes MotoGP, Moto2 and Moto3.

Moto2 class The Moto2 class is the middle class of the FIM motorcycle Grand Prix world championship. Engines are exclusively supplied by Triumph. The 765 cc inline-three cylinder, four-stroke engine has a peak power of around 140 bhp. The bikes have a power to weight ratio of approximately one kg/bhp, reaching a top speed of up to 300 km/h. The electronics and the tires are limited und supplied by FIM-sanctioned producers Magneti-Marelli and Dunlop, respectively. German motorcycle manufacturer KALEX engineering GmbH is the most successful manufacturer of the Moto2 class, winning nine of the last ten Moto2 world championships, with nowadays successful MotoGP riders Johann Zarco, Stefan Bradl, Pol Espagaro, Tito Rabat, Franco Morbidelli, Francesco Bagnaia, Alex Marquez and Enea Bastianini. KALEX supported the present work with measurement data from the 2019 Moto2 race in Aragon. For reasons of secrecy, the name of the rider is not mentioned here.

2.2 Motorsport Aerodynamics

In the early years of the automobile, aerodynamics played a minor role. Due to bad roads and low speeds, the benefits of aerodynamics were simply not needed. Only the expansion and improvement of the road network brought aerodynamics into the interest of vehicle developers. The goal was to improve the top speed for a given, limited engine power. In other words, the goal was a drag reduction of the bulky shapes of these times. Early attempts to apply aerodynamics to road vehicles were carried out by Kamm [33] and Klemperer [34] between 1922 and 1934. They transferred shapes from aeronautical and marine projects, resulting in unusual vehicle shapes compared to the state of the art at these times. The aerodynamic vehicle shapes were not accepted by the buying public. Perhaps these forms were ahead of their time, the revolutionary aerodynamic vehicles could not achieve a breakthrough. Therefore, it took until the two oil crises of the 1970s to bring aerodynamics back into the public interest of the automotive world. This time with the great pressure of improving fuel economy. Since then, the drag coefficients of production cars have been significantly reduced. The aerodynamic drag coefficient is defined as

$$c_D = \frac{D}{q_{dyn}\, A_x}\,, \tag{2.1}$$

with the drag force D, the dynamic pressure $q_{dyn} = \rho/2\, v^2$ and the projected area A_x. Driven by a customer demand of ever larger vehicles, the projected surface area has also grown considerably. This results in lower drag values, although the crucial drag force is growing. Therefore, a better comparable measure is the drag area, denoted as

$$c_D\, A_x = \frac{D}{q_{dyn}}\,, \tag{2.2}$$

which contains the size of the vehicles. Other aerodynamic measures like the lift or cross wind behaviour are of importance for production vehicles as well. The aerodynamic focus of lift forces in series development is largely on safety and stability. The focus of the drag force in series development is related to fuel economy and top speed.

Downforce in Motorsports In car racing the major criteria to increase the corner speed is downforce. In 1970 Formula One teams experimented with first downforce generating devices in the form of high mounted wings above the front and the rear axle. In 1977 the *Lotus '78* was the first Formula One racing car that uses ground effect to generate downforce. This was achieved by integrating an inverted wing profile into the overall vehicle concept. Additionally, mounted front and rear wings helped to increase the downforce even more. The wings were also used to change the aerodynamic balance – the equilibrium between the downforce on the front wheels and the downforce on the rear wheels.

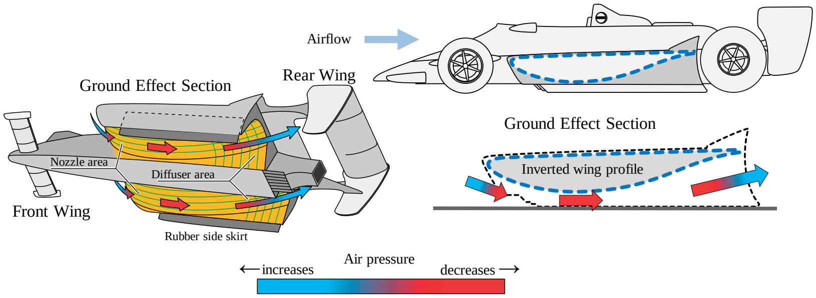

Figure 2.3: Downforce generation on the Lotus '78 (by Christoph Feichtinger – Own work, according to MagentaGreen [40]).

In a simplified case, without brake or drive torques, the influence of downforce to the corner speed can be estimated by the equilibrium of forces, denoted as

$$\mu_{lat}\left(mg - L\right) = \frac{mv^2}{r_c}\,, \tag{2.3}$$

where μ_{lat} is the required lateral tire friction coefficient, L is the lift force, m is the mass of the vehicle and r_c the actual turning radius. The lift force is defined as

$$L = \frac{\rho}{2} c_L A_x v^2\ , \tag{2.4}$$

where c_L is the lift coefficient. The lift is pointing upwards. The term downforce used here means a downward acting force. Thus, the downforce coefficient is the negative lift coefficient.

The Performance Envelope of a Racecar The acceleration capacity of a racecar in longitudinal and lateral direction can be visualized in the performance

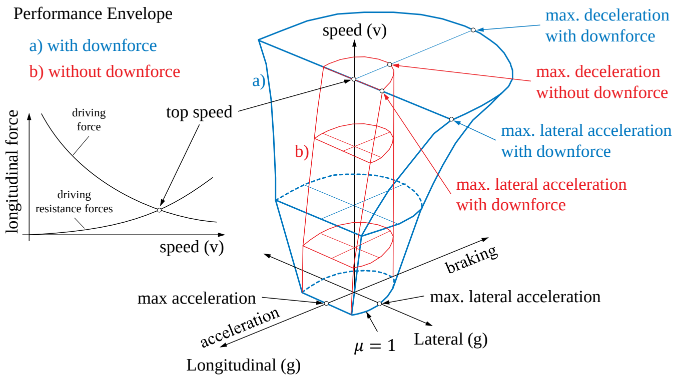

Figure 2.4: The performance envelope or g–g–v diagram for a racecar a) with and b) without downforce (by Christoph Feichtinger – own work).

envelope or g–g–v diagram. Fig. 2.4 shows the performance envelope with and without downforce. The performance envelope without downforce has approximately a cylindrical shape except the decreasing longitudinal acceleration capacity due to increasing driving resistance forces. The performance envelope with downforce has the shape of a funnel. The limitation is the lateral and longitudinal tire friction coefficient. The best performance can be reached when the racecar is operated on the boundaries of the performance envelope.

Downforce on Four– and Two–Wheelers Fig. 2.5 shows concepts of downforce generation on four- and two-wheelers and the resulting maximum speeds for constant velocity cornering. Subfigure d shows the maximum possible corner speed, based on Eq. 2.3, for a varying turning radius r_c and for lift coefficient values c_L between 0 and -2. In any case, the maximum possible corner speed increases with the turning radius. For higher downforce coefficients, the maximum cornering speed increases steeply, especially for larger turning radii. At a turning radius of $300\,m$ the maximum corner speed with a lift coefficient of $c_L = -2$ is nearly double the corner speed for the zero-downforce case. The corner speed turning radius relation holds for a four-wheeler shown in subfigure a, and a two-wheeler with a tilting wing displayed in subfigure b. A tilting wing assumes an always road-parallel wing, and therefore a downforce generation normal to the road surface plane. This is more a theoretical consideration than a practical development.

The more practical and allowed approach for a racebike is a fixed wing, shown in subfigure c. The wing leans with the bike, splitting up the downforce into a

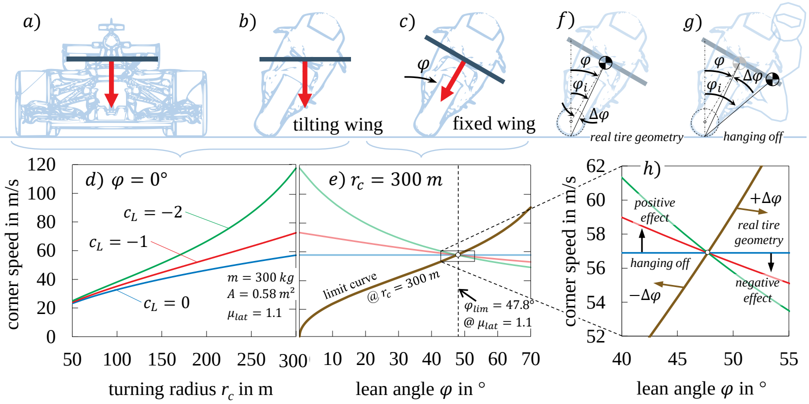

Figure 2.5: Downforce generation for (a) a four-wheeler, for (b) a two-wheeler with tilted wing and for (c) a two-wheeler with fixed wing concept. (d) shows the maximum possible corner speed vs. the turning radius r_c for different lift coefficients $c_L = 0, -1$ and -2 for the concepts (a) and (b). (e) shows the possible corner speed vs. the lean angle φ for the fixed wing concept. (f) and (g) show the influence of real tire geometry and the rider in hanging off. (h) shows a zoom section of (e) with the positive and negative influence of lean angle changes (by Christoph Feichtinger – own work).

vertical and a lateral component. For the fixed wing, Eq. 2.3 have to be extended by the lean angle components of the downforce, written as

$$\mu_{lat}\left(mg \underbrace{-L\,cos\varphi}_{vertical}\right) = \frac{mv^2}{r_c} \underbrace{-L\,sin\varphi}_{lateral}\ . \tag{2.5}$$

The vertical component $-L\,cos\varphi$ still increases the tire contact force and allows higher lateral tire forces and therefore, corner speeds. The lateral component $-L\,sin\varphi$ pushes the bike outwards. With reference to Eq. 1.1, the maximum lean angle can be calculated for a given lateral tire friction coefficient. Fig. 2.5 e shows the corner speed needed for the racebike in equilibrium cornering conditions against the lean angle.

Subfigure f shows the influence of a real tire geometry shape on the lean angle, where φ is the lean angle of the racebike, φ_i is the lean angle through the real road tire contact point and $\Delta\varphi$ is the lean angle increase. Considering the lean angle increase due to the real tire geometry, subfigure h shows a negative effect on the corner speed.

Subfigure g shows the influence of the rider in *hanging-off* on the effective lean angle φ. φ_i is the lean angle through the real road tire contact point and the center of gravity position of the overall racebike and rider system. The lean angle decrease is denoted by $\Delta\varphi$. The effective lean angle decrease has a positive impact on the corner speed, as can be seen in subfigure h on the upper left side. The rider can easily control the effective lean angle by body movements. A fixed wing cannot do that. Therefore, a low wing position is advantageous, as this generates downforces with less disturbing roll torque.

In reality both effects, the real tire geometry and the *hanging-off*, appear superimposed. To achieve an overall positive effect of a fixed wing on the corner speed, the rider has to overcome at least the lean angle decreases due to the tire geometry. In the shown lean angle range in subfigure h, the positive impact on the corner speed is in the range of 2 to $4\,m/s$.

The lean angle decreases due to *hanging-off* increases the vertical component of the downforce and reduces the lateral component at the same corner speed. This increases the vertical tire force. Therefore, the tire has more potential to transfer longitudinal forces for acceleration or braking at the same corner speed.

Early attempts in the 1970s and 1980s to establish aerodynamic wings to racebikes can be seen in Fig. 2.6 b and d. Due to unknown reasons they were not permanently used on racebikes – The assumptions are that

- the power was too low,
- the tire was able to transmit all longitudinal and lateral forces in more riding situations than today, and
- that the aerodynamic devices generated too much drag.

There might have been an advantage in corner acceleration potential, but the top speed loss was bigger. Thus, the wings obviously did not improve the overall performance of the racebike at these times.

Over the years the engine power in the premier class of Grand Prix racing increased up to $270\,bhp$. This results in the fact, that the winning factor for the top speed of a MotoGP racebike on the limited straights of road racetracks is not just the drag. Rather, the acceleration is important.

Ducati was a pioneer in modern racebike aerodynamics. In 2016 they reintroduced perfectly designed wings into the MotoGP world championship. The result was that they were nearly unbeatable in acceleration throughout the whole season. Nevertheless, an overall advantage on the lap time was not always visible. Thus, Marc Marquez with a Honda, without wings won the world championship this year. Andrea Dovizioso finished 5^{th} in the world championship as best Ducati rider.

Figure 2.6: Examples of Grand Prix racing motorcycle downforce devices. a) Honda RC213V and Ducati GP19 from 2019 [14], b) Rodger Freeth and his concept 'Aerofoil Vitko TZ750A' from 1977 [61], c) KTM RC16 from 2019 [35] (aerodynamic design by the author) and d) Barry Sheenes' Suzuki RG500 from 1979 [58].

In motorcycle racing, a lot happens in the mental performance of the riders. Professional racebike riders always want to be at the pulse of time and want to try out new things. So, it happened that all the teams entered the pre-season tests 2017 with wings. Wings have not triggered a revolution in motorcycle racing like the one in automobile racing in 1977 at this time. But nevertheless, they are a fixed part of the premier class of motorcycle racing since 2017. Actual downforce generating devices on racebikes are shown in subfigures 2.6 a and c.

Soon after, the smaller classes wanted to transfer the generation of downforce to their racebikes. The FIM immediately banned all kinds of downforce generating devices for the smaller classes to save development costs and to keep the competition simple.

Longitudinal Racebike Aerodynamics The biggest challenge of modern Grand Prix racing bikes is to put the engine power on the road. An effect when too much power is applied to the rear wheel is the lifting of the front wheel – a so called

Wheely. From a performance point of view the lifting of the front wheel during acceleration, means that available engine power is transferred into a vertical acceleration instead of a wanted longitudinal acceleration. Wings mounted in the front area of the racebike help to keep the front wheel on the track and improve the acceleration. Additional advantages of the wings are a better stability in high-speed sections and therefore, a better preparation for braking manoeuvres. To understand the principles of downforce on a racebike Fig. 2.7 shows a simplified representation of the aerodynamic forces acting on a racebike. The drag force and the overall lift force are acting in the aerodynamic center *AC*. They generate a pitching moment about the rear wheel contact point which is lifting the front of the racebike. Therefore, when talking about downforce on racebikes it means front lift avoidance. Front lift can be reduced by the general shape of the racebike or by Add-on parts like wings.

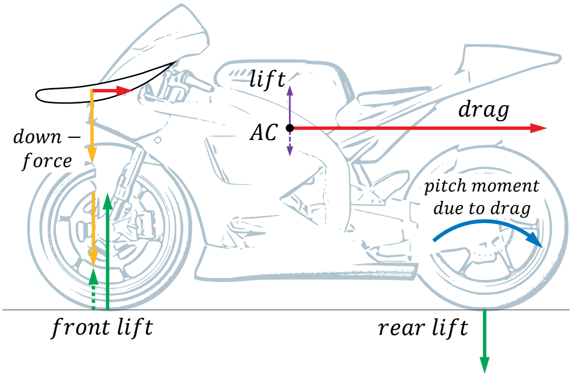

Figure 2.7: Longitudinal racebike aerodynamics (by Christoph Feichtinger – own work).

The wing position is quite sensitive to the overall performance in terms of front wheel lift and overall drag. Additional restrictions for the wing positions and shape are design space limitations as well as the necessary lean angle freedom. Saying this, the reduction of the front wheel lift by an optimization of the general racebike layout and design would be also an efficient way from an overall performance point of view.

Influence of the Rider The riding style describes the specific riding technique of racebike rider. This means the specific movement of the rider on the racebike in different riding situations. Fig. 2.8 shows different riding situations. They show

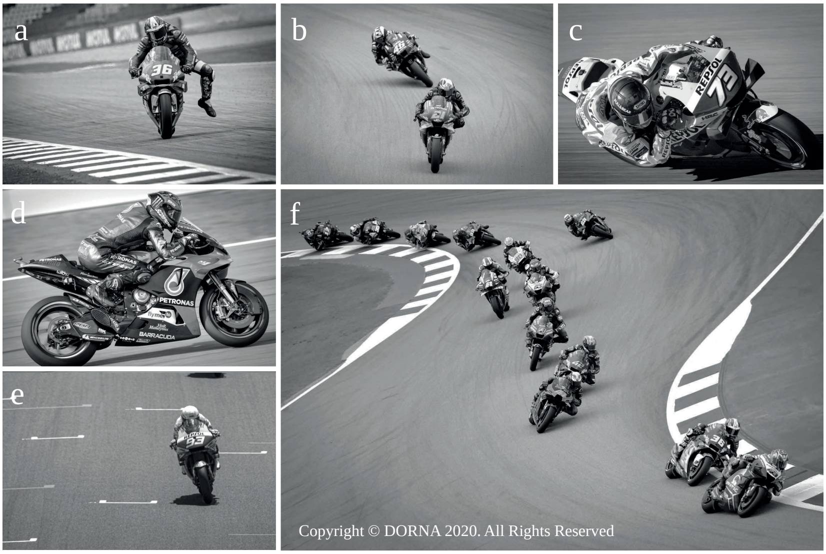

Figure 2.8: Racebike riding situations. a) braking with left foot facing out, b) change of direction, c) cornering situation, d) acceleration with body moved forward, e) top speed position and f) various riders during a change of direction.

the permanent movement of the rider on the racebike. The pictures illustrate the fact that the rider has an enormous influence on the riding dynamics of the racebike. The following list briefly describes the most important riding situations.

- On a long straight line the rider tries to make himself as small as possible to keep the aerodynamic drag as low as possible (see Fig. 2.8 e). The aim is maximum top speed.

- During straight line braking, the rider lifts himself up to give the air the maximum possible surface area to attack. This increases the drag force. A high drag force in the braking phase supports the deceleration and thus ensures a shorter braking phase. This means the motorcycle can go faster for a longer time.

- During braking into a corner, the rider lifts himself up and stretches the foot facing to the curve outwards (see Fig. 2.8 a). This gives the rider an additional braking drag force and helps him to go into the corner.

- During cornering the rider is leaning his body into the curve to move the center of gravity in lateral direction into the center of the curve – This riding situation is called *hanging-off* (see Fig. 2.8 c and f). With this the resulting center of gravity of the racebike and rider system is also moving into the direction of the center of the curve. This results in a lean angle which is bigger than the lean angle of the racebike itself. Thus, the tires can transform more longitudinal forces for the same cornering radius. This improves the longitudinal acceleration and deceleration capability and therefore the corner segment time.
- During acceleration out of a corner, the rider tries to bring the racebike as soon as possible into an upright position. The rider is using his own weight to change the balance between the front and the rear wheel to avoid wheely (see Fig. 2.8 d).

Aerodynamic related Areas There are some aerodynamic related areas which are mandatory for the operation of a racebike, like the cooling and the engine air intake. Some lower priority areas like the exhaust gas flow, the ergonomics or local flows and turbulences around the rider are important for the operation of the racebike as well, but they are not safety critical. The relation between the cooling air flow and the drag area is shown in Fig. 2.9 b. It shows two different cooling inlet openings. The small cooling inlet has a lower air volume flow, resulting in a lower drag but a higher coolant temperature. The bigger inlet increases the air volume flow, resulting in a lower coolant temperature but a higher drag area. Fig. 2.9 a shows the positive impact to the engine performance, by using the total pressure of the oncoming upstream speed as *Charger*. This type of engine charging is called the *Ram Air Effect*.

2.3 The Racebike State on a Racetrack

The lean angle and the speed of the racebike are the leading quantities to describe the racebike state on a racetrack. Therefore, the speed – lean angle plot is introduced here.

Speed – Lean Angle Plot Fig. 2.10 shows a generic speed – lean angle plot with the speed range of up to $300\,km/h$ for Moto2 racebikes. The plot contains the following information.

- **Maximum possible lean angle** ($\tan\varphi_{bike} = \mu_{lat}$) as limitation of the lateral tire friction coefficient – horizontal blue lines.

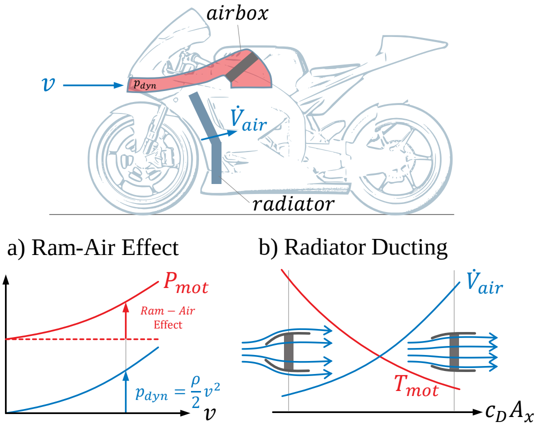

Figure 2.9: Aerodynamic related areas - a) ram-air effect, b) radiator ducting (by Christoph Feichtinger – own work).

- **Design space limitation** for the lean angle – horizontal green lines. This is the mechanical limit where any part of the racebike is touching the ground. Usually this is the footrest or the lower part of the swingarm. The maximum lean angle from the design space limitation must be bigger than the maximum lean angle from the lateral tire friction coefficient. Only then, the racebike can be moved at the dynamic riding limit without touching the ground – which normally results in a crash.

- Iso-lines for **constant cornering radii** between $r_c = 10 \cdots 500\,m$ for a given, constant lateral tire friction coefficient of $\mu_{lat} = 1$. The Iso-lines are calculated using the simple relation between the lean angle and the racebike speed $tan\,\varphi_{bike} = v_{bike}^2/(r_c\,g)$. They show the maximum possible lean angle φ_{bike} for a given corner radius r_c and a given racebike speed v_{bike}.

- The **motion profile** of a track segment when the racebike is accelerating out of a left-hand corner onto a long straight is shown in the lower right corner of the plot – red line. The marked points A, B and C are also marked in the main plot. The motion profile shows the individual speed – lean angle states along this track segment.

- In the shown motion profile the racebike starts at a lean angle of $-55°$. In the first part the racebike is raised at moderate longitudinal speed changes.

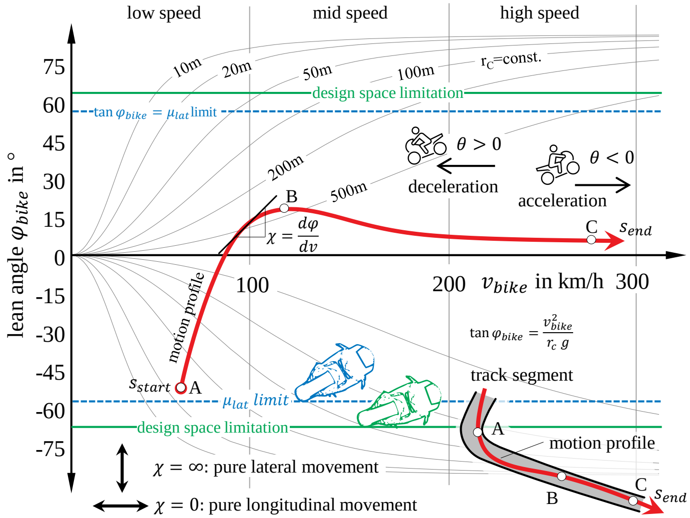

Figure 2.10: Speed – lean angle plot with lean angle limits of the lateral tire friction and by the available design space. The diagram shows Iso–lines for a constant cornering radius relation between the lean angle and the racebike speed. The red line shows a typical motion profile on a track segment when accelerating out of a left-hand corner onto a long straight (by Christoph Feichtinger – own work).

Then the racebike is rolling slightly in the opposite direction (+20° point B), before bringing the racebike in the final upright position. The section between points B and C shows mainly a longitudinal acceleration with small lean angle changes.

- The derivative of the lean angle according to the speed, is defined here. It is denoted with the quantity chi χ, just that $\chi = d\varphi/dv$. The **new introduced derivative quantity** χ shows the slope of the motion profile in the speed – lean angle plot.
  - Chi values of $\chi = \pm\infty$ show a **pure lateral movement** of the racebike – Rolling of the racebike without any speed change.
  - Chi values of $\chi = 0$ show a **pure longitudinal movement** of the racebike – Accelerating or braking without any lean angle change.
- It is task of the rider to optimize chi χ, such that the combination of side

forces and longitudinal forces on the grip level leads to a minimum lap time.

2.4 Aerodynamic Development Tools

Actually, there are three main aerodynamic development tools which are used in the automotive industry and in various sports and motorsports applications:

- numerical flow simulations,
- wind tunnel testing and
- road or track experiments.

In the past, alternative experimental methods were carried out by towing a model in still water. The so-called towing-tank technique was used among others by d'Alembert [3] in 1752. Another experimental method to determine the resistance of a body moving in a fluid was e.g. a swirling arm as used by Robins [54]. The method of the swirling arm was still used in modern times. The biggest disadvantage is that after a certain time the air begins to rotate and therefore the relative speed can no longer be clearly determined. Further interesting experimental methods at the beginning of the twentieth century were carried out by Newton [44] and Eiffel [18]. They dropped spheres and flat plates from the dome of St. Pauls' Cathedral and the Eiffel tower, measuring the time as a function of the displacement. The derived acceleration a_{drop} was compared with the acceleration due to gravity g. The drag force was then calculated using the following equation

$$D = m\left(g - a_{drop}\right), \tag{2.6}$$

with m as the mass of the dropped body. Some of these methods are still in use, but not widely applied or used by the aerodynamic community.

In the next paragraphs, the current tools are explained in more detail. The description of the numerical flow simulation is mainly adapted from previous work by Feichtinger [19].

Numerical Flow Simulations Numerical flow simulations or computational fluid dynamic methods, hereinafter called CFD methods, are based on solving the fundamental equations of fluid motion. The basic equations of fluid motion describe the conservation of mass, momentum, and energy. Assuming isothermal flow, the conservation of energy can be disregarded, so that the flow is only governed by the differential balance equations of mass and momentum, generally termed Navier-Stokes equations. The conservation principle follows the axiom:

> *Mass cannot neither be generated nor destroyed.*

This implies that the temporal change of mass inside a given volume must be balanced by the mass fluxes across the volumes surface. The corresponding balance equation reads in index notation

$$\frac{\partial \rho}{\partial t} + \frac{\partial (\rho u_i)}{\partial x_j} = 0 \ , \tag{2.7}$$

where ρ is the density, and u_i represents the component of the velocity vector into the direction x_i, wheras x_j denotes the derivative in the directions $j = x, y, z$ for a cartesian coordinate system. The conservation of momentum basically represents Newtons' second law stating the axiom:

> *The time rate of change of the momentum of a body is equal to the sum of all applied surface and body forces.*

The corresponding differential conservation equation reads

$$\frac{\partial (\rho u_i)}{\partial t} + \frac{\partial (\rho u_i u_j)}{\partial x_j} = -\frac{\partial p}{\partial x_i} + \rho f_i + \frac{\partial \tau_{ij}}{\partial x_j} \ , \tag{2.8}$$

where f_i is the body force per unit mass into the direction x_i, p is the pressure *acting in all directions*, and τ_{ij} is the viscous stress tensor. The viscous stresses are induced by the deformation of the fluid elements in motion. To solve the fluid motion equations two basic concepts can be distinguished: The Large Eddy Simulation method (LES), and the statistical model generally termed Reynolds-Averaged Navier-Stokes (RANS) models. The third possibility, a model-free approach of direct numerical simulation, which directly resolves all relevant scales of turbulent motion, is discarded in current applications due to its prohibitively high computational costs.

CFD methods are used to simulate the acting forces on single parts or the complete system as well as for a detailed analysis of the local flow fields, e.g., by visualization with streamlines or turbulence quantities. CFD methods have the advantage to replicate the same boundary conditions. Therefore, CFD methods are well suited to sort out general design principles by parameter studies. To ensure the meaningfulness and validity of the simulation forecasts, various validation, and verification setups for typical geometries like a sphere [37] or generic vehicle shapes like the Ahmed body [2] are well established. Most of the validation and verification projects were carried out against wind tunnel measurements. In general, no numerical flow simulation covers a generic flow situation for all types of geometries and for the complete Reynolds number und turbulence level range which might occur. Therefore, the CFD models always need a preliminary description of the operating environment of the test body, including the important upstream flow conditions. Depending on the expected flow field and vortex shedding behaviour the simulation must be set up based on best practice examples like presented by Drage et.al. [15], or by the experience of the simulation engineer. There are many possibilities for tuning the model, like different grid sizes, different turbulence models and different solver settings. The tuning parameters are usually chosen to replicate the occurring flow effects and the measured flow variables from the wind tunnel.

Wind Tunnel Testing The wind tunnel is the classical test rig for air flow experiments. In contrast to most real-life conditions, the test body stands still, and the fluid moves along the test body. The fluid is generally driven by a blower to obtain a certain flow velocity. For aerodynamic measurements of road vehicles, this implies that the reference system of the test body has changed, because the fluid is moving and the test body stands still, while the test body is moving. The wind tunnel design should always guarantee well controlled test conditions in the test section to ensure reliable results. There are several approaches to design a wind tunnel. Fig. 2.11 shows three different types of wind tunnels and their basic elements. Subfigure a show an open jet channel, subfigure b an Eiffel channel, and subfigure c a closed loop facility, often also called a Göttingen type wind tunnel. Latter one is used most nowadays, as this design has advantages in terms of energy consumption and flow quality with the drawback of higher installation costs and space requirements by the return channel. It is important

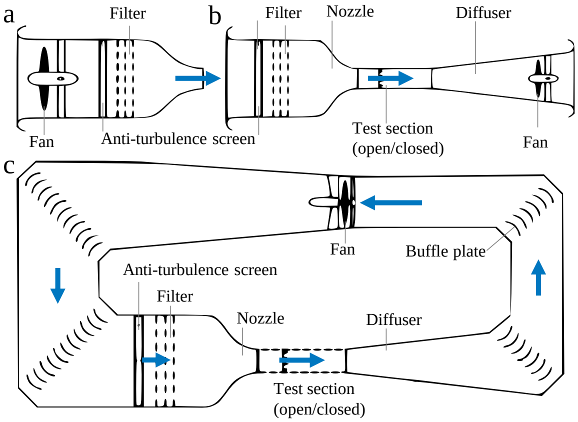

Figure 2.11: Wind tunnel types (Nitsche [46])

to be aware that also the wind tunnel is not the reality. The main reason for that is the turbulent flow regime, characterized by *scale providing* quantities like the turbulence intensity and the turbulence length scale. Details on the scale providing quantities are given in the Appendix C. The turbulence intensity and the turbulence length scale of the flow in the test section can be influenced by different anti-turbulence screens. The anti-turbulence screens divide the large-scale vortices generated by the fan into small ones. Nowadays wind tunnels are mainly designed towards low turbulence levels of $Tu \sim 0.1 \cdots 0.2\,\%$. Wordley et. al. [62] presented on-road measurements of the turbulence intensity for a freeway with road obstacles. The on-road measurement shows turbulence intensities up to $Tu = 18\%$. Thus, the on-road measurements show much higher turbulence intensities compared to the turbulence intensities in actual wind tunnels. Therefore, the operational domains are generally different, although the upstream flow angles and the velocity magnitudes are similar. This must be taken into account for the validation of wind tunnel results with real track measurements.

Track Experiments Wind tunnel measurements deliver directly forces and moments, while real racetrack riding situations deliver various measurement quantities, but generally not the aerodynamic forces and moments. Additional measurements on the test object can help to correlate real track measurements to wind tunnel measurements or CFD simulations.

Common tools are surface pressure tapings or a flow visualization with fluorescent paint, colloquially called flow-vis. It is a mixture of a fluorescent powdered dye suspended in paraffin/kerosine oil. The oil has a low viscosity allowing it to flow over the surfaces before drying and revealing the direction and state of flow on the surface. The pictures captured after a constant speed drive with flow-vis or the surface pressure readings for defined test speeds can be used for a detailed correlation between track and wind tunnel measurements as well as for surface streamline pictures from numerical flow simulations.

2.5 Aerodynamic Development Methodology

Classical development methodologies in the engineering world are:

- **Agile** development methodologies like Scrum or Kanban. They are based on iterative development steps. The requirements and solutions are worked on by self-organizing cross-functional teams.
- **Rapid** prototyping development methodology. It is based on an iterative development and the rapid construction of prototypes. This method deliberately avoids long advance planning.

- **Waterfall** development is a sequential development approach. The development phases are requirements analysis, system design, implementation, testing, integration, deployment and maintenance. The development phases are sequential phases with some overlap and feedback control loops.

- **Spiral** development methodology combines some key aspects of the waterfall methodology and the rapid prototyping methodology. The focus of this methodology is on the risk assessment. The project risks are minimized by breaking a project down into smaller segments. Therefore, changes are easier to implement during the development process. This also reduces the risk of the overall project.

- **V-Model** is a graphical representation of a systems development lifecycle with reference to VDI [32], shown in Fig. 2.12. The left side of the 'V' represents the project definition. The right side of the 'V' represents the project test and integration. The verification and validation is done at the different system levels (list from low level to high level).
  - Integration tests against detail design.
  - System verification and validation against the system requirements and architecture.
  - Operation and maintenance against the concept of operations.

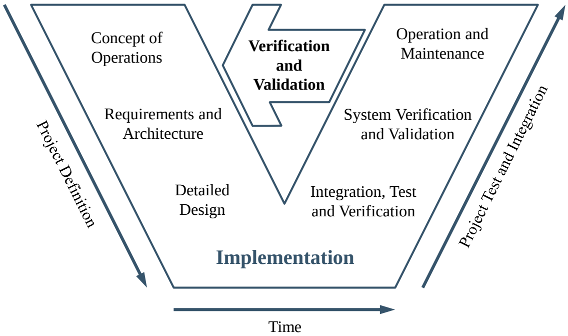

Figure 2.12: The V-Model of the systems engineering process (VDI [32]).

The development of a racebike is most like the rapid prototyping development methodology – The constant search for the smallest improvements and the immediate realization. Fig. 2.13 shows the aerodynamic development process of a

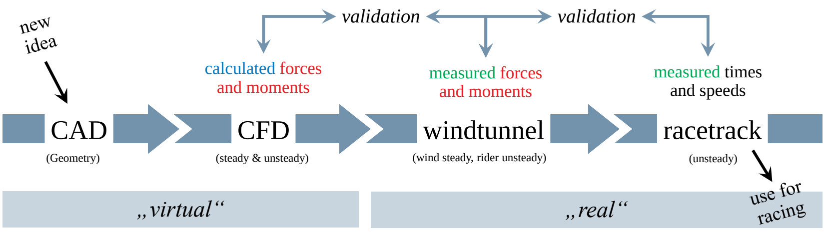

Figure 2.13: Aerodynamic development process of a MotoGP factory racing team from author experience (by Christoph Feichtinger – own work).

MotoGP factory racing team from author experience. New design ideas are first drawn with Computer Aided Design (CAD) Methods. The CAD geometry of the whole racebike and the rider is then prepared for the following CFD simulation. The CFD simulation is used for pre-selections and detail-studies of the design ideas. The best designs are built as prototypes for windtunnel tests. The windtunnel is used for a check of the pre-selected design ideas. The wind tunnel is also used for the optimization of the racebike geometry to the rider and vice versa. The final check of new design ideas is made on the racetrack before the new parts are released for racing.

In racing, the straight forward development process from Fig. 2.13 is a loop or, if adding the development progress, a spiral. Fig. 2.14 shows the aerodynamic development loop and spiral.

Validation The development process needs a permanent validation between CFD, windtunnel and racetrack. A major challenge in the validation of the single development steps is that every development tool calculates or measures different quantities.

- In **CFD** simulations aerodynamic forces and moments acting on the racebike and rider are **calculated**.

- In **windtunnel** test aerodynamic forces and moments acting on the racebike and rider are **measured**.

- On **racetracks** lap times, speeds, suspension strokes and some more quantities of the racebike are **measured**. Forces can be measured on selected components (e.g. the wheel forces and torques).

Therefore, the forces and moments must be converted into lap times and speeds or vice versa for comparability. A common approach are vehicle dynamics models which use the forces and moments from CFD simulations and windtunnel tests for lap time simulations. This approach is well established in car racing. Lap time simulations for car racing have a high validity and can accurately predict the lap time. Lap time simulations for racebikes do exist, but they are not as accurate as for racing cars. This is mainly due to the great influence of the rider and the much higher complexity of the riding dynamics.

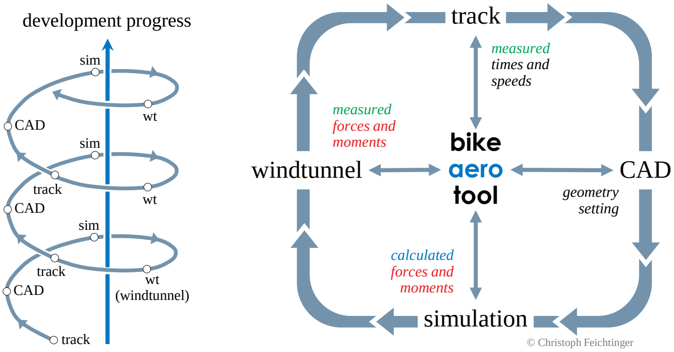

© Christoph Feichtinger

Figure 2.14: Aerodynamic development tools – bike aero tool (by Christoph Feichtinger – own work)

- The rider can make a lap time difference of $1-2\,s$ through its willingness to take risks.
- The rider position on the racebike constantly changes and has a big impact on the acting weight, inertia and aerodynamic forces.
- The vehicle is stabilized by gyroscopic forces and includes lean angle dynamics.
- The center of gravity is typically much higher, leading to large wheel force variations and pitching dynamics.

The present work aims at a development tool, which is used in the center of the aerodynamic development loop and which directly covers all disciplines. The tool is named *bike aero tool*. The tool should be used

- to **validate** CFD simulations and windtunnel tests against each other,

- to validate CFD simulations and windtunnel tests against racetrack measurements,
- to check the **plausibility** of racetrack measurements and
- to **monitor** and track the development progress.

For future applications, the complex vehicle dynamics model of the racebike from the *bike aero tool* can be used for vehicle dynamic simulations. In the long term, the model and the tool can be the base for lap time simulations of racebikes. The *bike aero tool* is not a replacement of a single aerodynamic development tool. Rather, it is a meaningful and necessary addition.

Chapter 3

Theoretical Framework

The theoretical framework gives an overview of the mechanics of solid bodies, describes the operational domain of a racebike and gives a more detailed insight into motorbike aerodynamics. Finally, the theoretical framework for tire modelling is presented.

3.1 The Mechanics of Solid Bodies

The mechanics of solid bodies is a branch of mechanics that deals with the investigation of movements of bodies and with the forces resulting from those movements. A body is defined as a continuum filled with matter (mass).

3.1.1 Frames of Reference and Axis Systems

Frames of Reference The description of kinematic quantities like the position of a body, the velocity or the angular velocity requires a frame of reference. The choice of the frame of reference is initially completely arbitrary. For a racebike, two distinct frames of reference are useful:

- An inertial *Earth* frame of reference, which is fixed to the Earth (Tab. 3.1 a). Knowing that also the earth itself is in permanent motion around the sun, nevertheless the earth fixed frame of reference is handled as a inertial frame of reference.

- The non-inertial *body* frame of reference, which is fixed to the racebike (Tab. 3.1 c). Moving frames of reference are used for different observation views. Especially the treatment of the environmental wind conditions on a body in motion requires a change of the frame of reference.

Axis Systems The orientation of the axis system is used to quantify any vector or tensor. The choice of the axis system orientation is arbitrary. If the body has a huge movement range and is rotating around different axis, then two axis systems are naturally obvious:

- *Earth* or inertial axes ${}_Ie_x$, ${}_Ie_y$, ${}_Ie_z$ fixed to the ground (Tab. 3.1 b). The *Earth* axes are non-rotating, assuming that the earths' rotation is neglected.
- *Body* axes ${}_be_x$, ${}_be_y$, ${}_be_z$ fixed to the body (Tab. 3.1 d). These axes translate and rotate along with the body relative to the inertial axes.

Tab. 3.1 shows that the *frame of reference* and the *axis system* are two distinct concepts. The index of an arbitrary vector on the lower left denotes the axis system. The frame of reference is not specified separately in the vector notification.

Table 3.1: Racebike moving on a racetrack at velocity v_{bike} as seen in the earth and body frame of reference and the stationary and moving axis systems.

(a) Observer in **earth frame** of reference

(c) Observer in **body frame** of reference

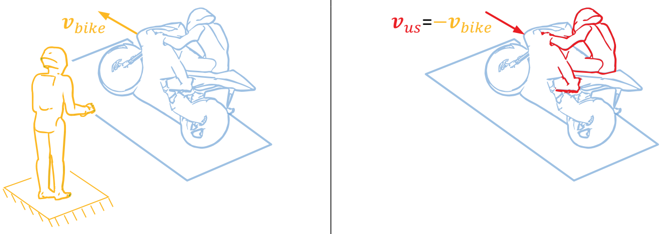

(b) **Earth axis** system I

(d) **Body axis** system b

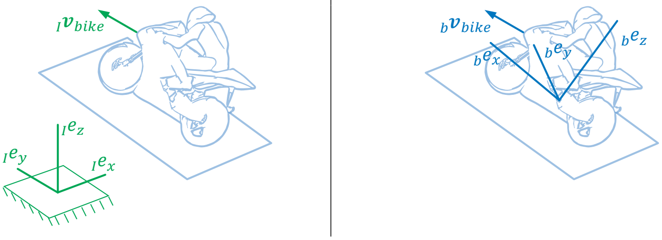

The velocity ${}_I\mathbf{v}_{bike}$ of the racebike is defined in the earth frame of reference, in the earth axis system. The angular velocity vector ${}_b\boldsymbol{\omega}_C$ of the chassis is defined in the earth frame of reference, in the body axis system. The upstream flow vector ${}_b\mathbf{v}_{us} = -{}_b\mathbf{v}_{bike}$ which equals the racebike reference speed for completely wind-free conditions is defined in the body frame of reference and in the body axis system. All relative vectors e.g., the position of the wheel points with respect to the racebike reference point $C1$ are expressed in the body frame of reference in body axes.

3.1.2 Kinematics of Relative Motion

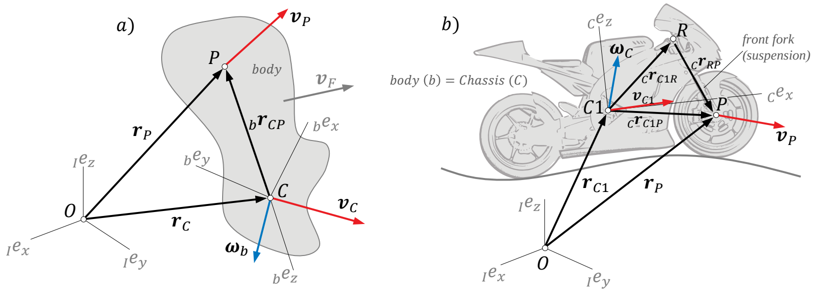

Figure 3.1: Kinematics of relative motion of a) a generic body and b) a racebike (by Christoph Feichtinger – own work).

Referring to Fig. 3.1 a, the absolute position vector of a point of interest on the body P is defined as

$$\mathbf{r}_P = \mathbf{r}_C + \mathbf{r}_{CP}\,, \tag{3.1}$$

with $\mathbf{r}_C$ as the absolute position vector of the body reference point C and $\mathbf{r}_{CP}$ the relative position vector of the local point P. Typically, the absolute position vector is defined in the inertial frame of reference I whereas the relative position vector is often defined in the moving frame of reference b. In this case the local position vector ${}_b\mathbf{r}_{CP}$ has to be transformed into the inertial frame of reference I as follows

$$\mathbf{r}_{CP} = \mathbf{A}_{Ib}\,{}_b\mathbf{r}_{CP}\,, \tag{3.2}$$

with the transformation matrix $\mathbf{A}_{Ib}$ defining the orientation of the body. If no indexing is specified, the frame of reference here and in the following is the inertial frame of reference.

In the context of a racebike, the local position vector (see Fig. 3.1 b) is used in different ways, e.g.

- The local position vector ${}_C\mathbf{r}_{C1R}$ is for example a fixed geometric position of the point R in the chassis axis system.
- The local position vector ${}_C\mathbf{r}_{RP}$ is the simplified representation of the front suspension stroke.
- Therefore, the local position vector ${}_C\mathbf{r}_{C1P} = {}_C\mathbf{r}_{C1R} + {}_C\mathbf{r}_{RP}$ contains the relative movement of the front suspension stroke.

The transformation matrix for the Euler angles according to the common automotive standard axis notation (DIN ISO 8855) from the inertial frame of reference I into the body fixed frame of reference b, is defined as

$$\mathbf{A}_{Ib} = \mathbf{R}_x^T(\varphi)\,\mathbf{R}_y^T(\theta)\,\mathbf{R}_z^T(\psi)\,, \tag{3.3}$$

where the order of rotations is $x-y-z$ with φ as the lean angle, θ as the pitch angle and ψ as the yaw angle. Using the elementary rotations, the transformation matrix can be written as

$$\mathbf{A}_{Ib} = \begin{bmatrix} c_\theta\, c_\psi & s_\varphi\, s_\theta\, c_\psi - c_\varphi\, s_\psi & c_\varphi\, s_\theta\, c_\psi + s_\varphi\, s_\psi \\ c_\theta\, s_\psi & s_\varphi\, s_\theta\, s_\psi + c_\varphi\, c_\psi & c_\varphi\, s_\theta\, s_\psi - s_\varphi\, c_\psi \\ -s_\theta & s_\varphi\, c_\theta & c_\varphi\, c_\theta \end{bmatrix}. \tag{3.4}$$

The angular functions $sin\varphi$, $cos\varphi$, $sin\theta$, $cos\theta$ and $sin\psi$, $cos\psi$ were abbreviated by s_φ, c_φ, s_θ, c_θ and s_ψ, c_ψ. The transformation matrix is converted into the corresponding unit quaternion representation using the method of Bar-Itzhack [4], written as $q_{Ib} = rotm2quat(\mathbf{A}_{Ib})$. A quaternion number is a four-part hypercomplex number represented in the form of

$$q = e_0 + e_1\, i + e_2\, j + e_3\, k\,, \tag{3.5}$$

where $e_{0\cdots3}$ are real numbers, also called the Euler parameters and i, j, k are the basic elements, satisfying the equation

$$i^2 = j^2 = k^2 = ijk = -1\,. \tag{3.6}$$

Thus, the four Euler parameters can be written in vector notation as

$$\mathbf{p}_E = \begin{Bmatrix} e_0 & e_1 & e_2 & e_3 \end{Bmatrix}^T\,. \tag{3.7}$$

The transformation matrix $\mathbf{A}_{Ib}$ can be alternatively represented as product of two matrices

$$\mathbf{A}_{Ib} = \mathbf{G}_{Ib}\,\mathbf{L}_{Ib}^T\,, \tag{3.8}$$

where $\mathbf{G}_{Ib}$ and $\mathbf{L}_{Ib}$ are defined according to Nikravesh [45] as

$$\mathbf{G} = \begin{bmatrix} -e_1 & e_0 & -e_3 & e_2 \\ -e_2 & e_3 & e_0 & -e_1 \\ -e_3 & -e_2 & e_1 & e_0 \end{bmatrix} \text{ and } \mathbf{L} = \begin{bmatrix} -e_1 & e_0 & e_3 & -e_2 \\ -e_2 & -e_3 & e_0 & e_1 \\ -e_3 & e_2 & -e_1 & e_0 \end{bmatrix} . \tag{3.9}$$

There is an excellent textbook on the derivation of the angular velocity vector using Euler parameters by Rill [53]. Without any further explanation here, the angular velocity vector can be written as

$${}_I\boldsymbol{\omega}_b = 2\,\mathbf{G}_{Ib}\,\dot{\mathbf{p}}_E \quad\text{and}\quad {}_b\boldsymbol{\omega}_b = 2\,\mathbf{L}_{Ib}\,\dot{\mathbf{p}}_E\,, \tag{3.10}$$

for the inertial frame of reference I and the body fixed frame of reference b, respectively. With this the time derivative of the position vector $\mathbf{r}_P$ is written as

$$\mathbf{v}_P = \frac{d\mathbf{r}_P}{dt} = \mathbf{v}_C + \mathbf{v}_{CP} + \boldsymbol{\omega}_b \times \mathbf{r}_{CP}\,, \tag{3.11}$$

with $\mathbf{v}_C$ as the velocity vector of the moving body, $\mathbf{v}_{CP}$ the relative velocity of the local point P and $\boldsymbol{\omega}_b$ as the rotation-rate vector of the body. The latter term $\boldsymbol{\omega}_b \times \mathbf{r}_{CP}$ results from the rotation of the body around the body reference point C. Alternatively, the velocity of the moving body and the velocity resulting from the rotation of the body are often summarized into the guidance velocity $\mathbf{v}_F$. With this, the velocity of the point P can be written as

$$\mathbf{v}_P = \mathbf{v}_F + \mathbf{v}_{CP}\,. \tag{3.12}$$

The time derivative of Eq. 3.11 leads to the acceleration of the point P denoted as

$$\mathbf{a}_P = \frac{d\mathbf{v}_P}{dt} = \underbrace{\mathbf{a}_C + \frac{d\boldsymbol{\omega}_b}{dt} \times \mathbf{r}_{CP} + \boldsymbol{\omega}_b \times (\boldsymbol{\omega}_b \times \mathbf{r}_{CP})}_{\textit{Guidance}} + \underbrace{\mathbf{a}_{CP}}_{\textit{Relative}} + \underbrace{2\boldsymbol{\omega}_b \times \mathbf{v}_{CP}}_{\textit{Coriolis}}\ , \tag{3.13}$$

where the first term is the guidance acceleration, covering the acceleration of the moving body, the acceleration due to angular velocity change and the centrifugal acceleration of the local point. The second term covers the relative acceleration of the local point P. The third term is the Coriolis acceleration.

3.1.3 Types of Constraints

There are different types of constraints for mechanical systems. Without constraints, a three-dimensional body in three-dimensional space can move without any limitation of its position or velocity. One speaks of a body with 6 degrees of freedom. As soon as only one of these degree of freedoms is restricted, the body is called a constrained mechanical system. There are different types of constraints, which can be formally expressed by mathematical equations or inequalities:

- **Geometric** constraints are restricting the position in one or more directions. An example for this is a pendulum, which has only one geometrical degree of freedom, the swing angle.
- The freedom of movement of a body can be restricted by a velocity constraint. An example for a **Kinematic** constraint is a skate blade on ice.
- A constraint without explicit time dependency is called a fixed or **Sceleronom** constraint. The corresponding example is a pendulum.
- A constraint with explicit time dependency is called a floating or **Rheonomous** constraint. An example is a sphere rolling down a moving inclined plane.
- **Holonomic** constraints can be expressed as geometric constraints or as integrable kinematic constraints. An example is a rigid wheel rolling on a two-dimensional plane (see Fig. 3.2 a).
- **Non-holonomic** constraints are not integrable kinematic constraints or single-sided constraints. An example is a rigid wheel rolling in three- dimensional space on a plane (see Fig. 3.2 b).

Non-holonomic constraints are often constraints which are defined by mathematical inequalities. These forced-constraints often lead to differential-algebraic equations (DAE) when describing multibody systems. DAE means that in addition to the differential equations, algebraic constraint equations must be fulfilled. Often this leads to numerical difficulties. Within the present work this topic is especially important for the kinematically correct description of the road-tire contact.

3.1.4 Forces and Force Groups

Newtons first law states that in an inertial frame of reference, an object either remains at rest or continues to move at a constant velocity, unless acted upon by a force [10]. The foundation of the mechanics of a single particle k is *Newtons second law of motion*

$$\mathbf{F}_k = \frac{d\mathbf{p_k}}{dt} = \dot{\mathbf{p}}_k \,, \tag{3.14}$$

where $\mathbf{F}_k$ is the total force acting on the particle and $\mathbf{p}_k$ is the linear momentum of the particle. The dot on $\mathbf{p}_k$ indicates the time derivative of the linear momentum of the particle. The linear momentum of the particle is denoted by

$$\mathbf{p}_k = m_k \, \mathbf{v}_k \,, \tag{3.15}$$

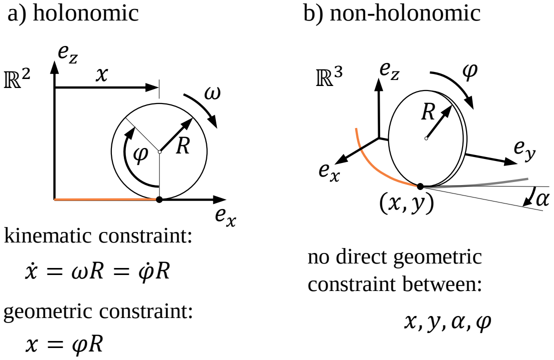

Figure 3.2: (a) Holonomic constraint of rigid wheel rolling in a two-dimensional plane. (b) Non-holonomic constraint of a rigid wheel rolling in three-dimensional space on a plane.

with the mass m_k and the velocity $\mathbf{v}_k$. A solid body is a system of N particles k. When applying this law to a solid body, it is necessary to distinguish the acting forces into external and internal forces acting on the particles k. The external forces $\mathbf{F}_k^{(e)}$ are forces acting from outside to the system boundaries. The internal forces $\mathbf{F}_k^{(i)}$ are forces between the particles of the system within the boundary. Thus, the equation of motion for the k^{th} particle is written as

$$\sum_{j=1}^{N}{}' \mathbf{F}_{kj} + \mathbf{F}_k^{(e)} = \mathbf{F}_k^{(i)} + \mathbf{F}_k^{(e)} = \dot{\mathbf{p}}_k \qquad (k = 1, 2, \cdot \cdot \cdot, N)\,, \tag{3.16}$$

where $\mathbf{F}_{kj}$ is the internal force on the k^{th} particle due the j^{th} particle. Under the assumption that $\mathbf{F}_{kj}$ (like $\mathbf{F}_k^{(e)}$) is subject to the *third Newtonian law*, the forces of the two particles k and j have the same magnitude and act in opposite directions. The prime over the summation sign indicates that the term $j = k$ must be excluded from the sum. By summing the equation of motion Eq. 3.16 of all particles of the system, it can be shown corresponding to Fung [24] that:

- The mass moves as if the sum of all external forces act on the whole mass at the center of gravity.
- The time derivative of the total angular momentum around a defined center of rotation is equal to the moment of the sum of the external force around the same point.

In the same way the kinetic energy of the system consists of two parts: the kinetic energy concentrated at the center of mass plus the kinetic energy of motion around the center of mass. The center of mass coincides with the center of gravity (COG). One could say that any force applied to the body in the center of gravity results in a linear acceleration of the body without an angular acceleration. An easy-to-understand example is a falling sphere. The gravity force acts in the center of gravity resulting in an acceleration of the body which equals the gravitational acceleration g. Such a punctiform point of action is rarely occurring in nature. There are rather spatially distributed forces, volume forces and area-distributed forces, surface forces [49]. For engineering applications volume and surface forces of single solid bodies are usually expressed by forces and moments in and around a fixed point.

A classification of body forces can be done by

(1) internal and external forces,

(2) active and reactive forces and

(3) forces that do work and forces that do no work.

Internal forces are forces which are acting between single bodies of a multibody system. External forces are applied from outside to the multi-body system. The mechanisms of internal and external forces on a body within a multibody system can be directly compared to a particle within a system from Eq. 3.16. Therefore, the distinction between internal and external forces depends on the choice of the system boundaries. A favourable choice of system boundaries can reduce model complexity.

The **active forces** denotes all forces and moments from physical interactions like springs, dampers, sliding friction, air resistance and electrical or magnetic fields. Active forces tend to set a body in motion, that means these are mostly external forces. The other type of forces are the reactive forces. They tend to prevent the motion of the body due to constraints or supports.

The **reactive forces** between two rigidly connected bodies i and j do perform mechanical work, $\mathbf{F}_{ij}\delta\mathbf{r}_i$ on the body i and $\mathbf{F}_{ji}\delta\mathbf{r}_j$ on the body j. Due to the rigid connection $\mathbf{F}_{ij}\delta\mathbf{r}_i = -\mathbf{F}_{ji}\delta\mathbf{r}_j$ holds and confirms that reactive forces do not perform mechanical work from a overall system point of view. Nevertheless, the reactive forces need to be calculated in some connections to calculate the active forces, like for example the calculation of any friction forces with Amontons [8] second law, written as $F_R = \mu F_N$, where μ is the coefficient of friction and F_N the reactive or contact force.

Generalized Forces In practical applications the system usually consists of several connected bodies (e.g. chain, motorbike multibody model, ...) as well as different connecting elements (e.g. ball joints, linear bearing, pivot bearing, ...) and force elements (e.g. springs, dampers, friction, aerodynamic drag, electrical and magnetic fields, ...). The forces of constraints between the single bodies within a multibody system are the reactive forces. They are not known a priori. Therefore, they are unknown quantitates which increase the modelling and calculation effort. In some cases, they are of no direct interest (e.g. the bearing forces of a pivot joint). To overcome these problems, the Lagrangian formulation (see e.g. Lanczos [36]) uses the principle of virtual work. The Lagrangian formulation uses independent coordinates to calculate the virtual work at force or moment acting points. Therefore, the active forces do perform work. The forces of constraint do not perform any work and do not appear in the virtual work of the overall system. The independent coordinates are used as generalized displacement coordinates.

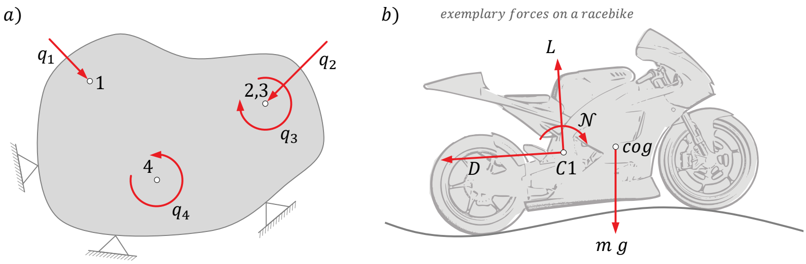

Figure 3.3: Generalized forces on a generic body and forces acting on a racebike (by Christoph Feichtinger – own work).

The generalized displacement d_i is the result of the acting generalized force q_i, just that

$$d_i \sim q_i \,. \tag{3.17}$$

Fig. 3.3 a show a generic body with linear (q_1, q_2) and angular (q_3, q_4) generalized forces resulting in linear and angular displacements $d_1 \cdots d_4$. In a general case the generalized displacements can be expressed by the sum of the generalized forces multiplied with the corresponding *influence coefficients* c_{ij}, written as

$$d_i = \sum_{j=1}^{n} c_{ij} q_j \quad (i = 1, 2, \cdot \cdot \cdot, n) \,. \tag{3.18}$$

The *influence coefficients* c_{ij} define the magnitude of the generalized displacement at i due to a generalized force at j. Fig. 3.3 b shows exemplary forces acting on a racebike. The aerodynamic lift force (L), the aerodynamic drag force (D) and the aerodynamic pitch moment ($\mathcal{N}$) are acting in the defined reference point $C1$. The weight force ($m\,g$) acts in the center of gravity (cog). These forces are not a priori generalized forces. The forces must first be transferred to a generalized view. This is done by using Jourdain's principle, explained in the following section.

3.1.5 Equation of Motion

The equation of motion is derived based on Jourdains principle [53] as

$$\mathbf{M}_{(\mathbf{y})}\dot{\mathbf{z}} = \mathbf{q}_{(\mathbf{y},\mathbf{z})}\,, \tag{3.19}$$

where $\mathbf{M}_{(\mathbf{y})}$ is the generalized mass matrix, $\dot{\mathbf{z}}$ the generalized acceleration vector and $\mathbf{q}_{(\mathbf{y},\mathbf{z})}$ denotes the generalized forces and moments vector. The mass matrix depends on the generalized coordinate vector $\mathbf{y}$ and is defined as the sum of the translational and rotational mass and inertias of the single bodies b as follows

$$\mathbf{M}_{(\mathbf{y})} = \sum_{b=1}^{n} \left\{ \underbrace{\frac{\partial_I \mathbf{v}_{0b}^T}{\partial \mathbf{z}} m_b \frac{\partial_I \mathbf{v}_{0b}}{\partial \mathbf{z}}}_{translation} + \underbrace{\frac{\partial_b \boldsymbol{\omega}_{0b}^T}{\partial \mathbf{z}}\, {}_b\mathbf{T}_{Sb} \frac{\partial_b \boldsymbol{\omega}_{0b}}{\partial \mathbf{z}}}_{rotation} \right\}, \tag{3.20}$$

where ${}_I\mathbf{v}_{0b}$ is the velocity of the center of gravity, indicated by the index 0, defined in the inertial axis system I and ${}_b\boldsymbol{\omega}_{0b}$ is the angular velocity vector defined in the body axis system b. Both velocity vectors and their transposed vectors are derived over the generalized velocity vector $\mathbf{z}$. The mass of the body m_b and the inertia tensor ${}_b\mathbf{T}_{Sb}$ contain the mass and inertia properties. The generalized forces and moments include the active forces and moments as well as the apparent forces and moments and the gyroscopic moments. The vector of the generalized forces and moments is written as

$$\begin{aligned} \mathbf{q}_{(\mathbf{y},\mathbf{z})} = \sum_{b=1}^{n} \Bigg\{ & \frac{\partial_I \mathbf{v}_{0b}^T}{\partial \mathbf{z}} \left[{}_I\mathbf{F}_b^{(a)} - m_b\, {}_I\dot{\mathbf{v}}_{0b}^S \right] \\ & + \frac{\partial_b \boldsymbol{\omega}_{0b}^T}{\partial \mathbf{z}} \left[{}_b\mathbf{M}_{Sb}^{(a)} - {}_b\mathbf{T}_{Sb}\, {}_b\dot{\boldsymbol{\omega}}_{0b}^S - {}_b\boldsymbol{\omega}_{0b} \times {}_b\mathbf{T}_{Sb}\, {}_b\boldsymbol{\omega}_{0b} \right] \Bigg\}, \end{aligned} \tag{3.21}$$

with the active force ${}_I\mathbf{F}_b^{(a)}$ in the inertial frame of reference and the active moments ${}_b\mathbf{M}_{Sb}^{(a)}$ in the body frame of reference. The last term in 3.21 denotes the gyroscopic moments. The apparent accelerations ${}_I\dot{\mathbf{v}}_{0b}^S$ and ${}_b\dot{\boldsymbol{\omega}}_{0b}^S$ are calculated from the directional derivates of the translational and rotational velocity over the generalized coordinates and the time derivate of the generalized coordinate $\dot{\mathbf{y}}$ as follows

$$\begin{aligned} {}_I\dot{\mathbf{v}}^S_{0b} &= \frac{\partial_I \mathbf{v}_{0b(\mathbf{y},\mathbf{z})}}{\partial \mathbf{y}}\,\dot{\mathbf{y}}\,, \\ {}_b\dot{\boldsymbol{\omega}}^S_{0b} &= \frac{\partial_b \boldsymbol{\omega}_{0b(\mathbf{y},\mathbf{z})}}{\partial \mathbf{y}}\,\dot{\mathbf{y}}\,. \end{aligned} \tag{3.22}$$

With the generalized mass matrix and the generalized force vector the generalized acceleration state of the multibody system can be calculated from Eq. 3.19.

3.2 The Operational Domain of a Racebike

The racebike must deal with two external impact factors. The contact to the ground, which is the mandatory requirement for the drive of a wheel driven object. And the air environment that is generating pressure and friction forces on all surfaces which are in contact with the air in any manner.

3.2.1 Racetrack Representation

The macroscopic racetrack is represented by a three-dimensional surface. An exemplary racetrack is shown in Fig. 3.4. The racetrack is defined by the spine curve ξ with the arc length s and the normal lateral offset n. The position of the spine curve in the inertial frame of reference is given by the position vector $\mathbf{r}_{pi}$. The position vector marks the position of the rear wheel contact point $H4$ on the racetrack surface in chapter 5 (From Measurement to Model). The x- and y-position

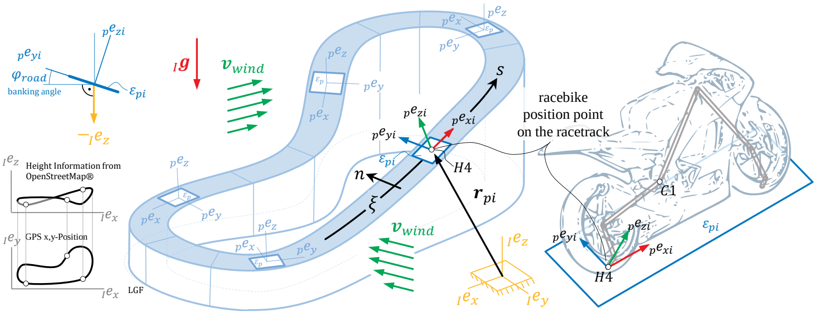

Figure 3.4: Exemplary racetrack representation with local road surface patches ε_{pi} (by Christoph Feichtinger – own work).

of the racebike in the inertial frame of reference is taken from GPS measurements of the racebike. The altitude information (z-coordinate in the inertial frame of reference) is taken from OpenStreetMap® [47].

The orientation of the local racetrack surface patch is needed for the positioning of the racebike on the racetrack. The task of the racetrack representation is to deliver the orientation of the local racetrack surface patch for each point on the racetrack. This is realized by an accompanying tripod, represented by the tangent ($\hat{\mathbf{t}}$), normal ($\hat{\mathbf{n}}$) and binormal ($\hat{\mathbf{b}}$) unit vectors. They form an orthonormal basis.

The tangent vector $\hat{\mathbf{t}}$ or ${}_p\mathbf{e}_{xi}$ is calculated by the central difference quotient at the discrete point i of the spine curve ξ, written as

$$\hat{\mathbf{t}} = {}_p\mathbf{e}_{xi} = \frac{d\xi_i}{ds} \simeq \frac{\xi_{i+1} - \xi_{i-1}}{2\,\Delta s}\,. \tag{3.23}$$

The normal vector is assumed to be horizontal. With this, the normal vector $\hat{\mathbf{n}}$ or ${}_p\mathbf{e}_{yi}$ is rectangular to the inertial z-axis ${}_I\mathbf{e}_z$, denoted as

$$\hat{\mathbf{n}} = {}_p\mathbf{e}_{yi} = {}_p\mathbf{e}_{xi} \times (-{}_I\mathbf{e}_z)\,. \tag{3.24}$$

The binormal vector $\hat{\mathbf{b}}$ or ${}_p\mathbf{e}_{zi}$ is defined as the cross product of the tangent and the normal vector, written as

$$\hat{\mathbf{b}} = {}_p\mathbf{e}_{zi} = {}_p\mathbf{e}_{xi} \times {}_p\mathbf{e}_{yi}\,. \tag{3.25}$$

A banking angle φ_{road} of the racetrack surface is considered with a rotation of the accompanying tripod around the ${}_p\mathbf{e}_{xi}$ vector. At this point it should be mentioned that the representation of the local moving track axis system is similar to the *Frenet-Serret* formulas introduced by Bartels et. al. [5], Piegl [50] and Shen [56]. The major difference is the definition of the normal vector $\hat{\mathbf{n}}$ which is pointing in the center of the local curvature in the osculating plane for the *Frenet-Serret* formulas, while within the present work it is defined in reference to the inertial z-axis ${}_I\mathbf{e}_z$.

3.2.2 Environment Model

The environment model defines the ambient air conditions of the operational domain. These can be split into two main groups:

(1) Wind- and weather-related influences like temperature, ambient pressure, humidity, precipitation, wind speed, wind direction and turbulences, hereinafter called the ambient state conditions.

(2) The ambient conditions related to the competitors or surrounding obstacles which are changing the ambient conditions in different ways.

The temperature and the ambient pressure are relatively uniformly distributed in the limited operational domain of a racetrack. They are needed to derive the density ρ_{air} and the kinematic viscosity ν_{air}. The US Standard Atmosphere [26] defines the following values for air at sea level:

- Temperature: $t_{air} = 15°C$
- Pressure: $p_{air} = 1.0132 \times 10^5 \, Pa$
- Density: $\rho_{air} = 1.225 \, kg/m^3$
- Viscosity: $\nu_{air} = 1.79 \times 10^{-5} \, kg/m - s$

Environmental Wind The environmental wind can be completely different at different locations on the racetrack. The environmental wind field is in general a turbulent wind field. Thus, for a complete description of the wind conditions a three-dimensional representation of the environment is needed. Feichtinger et. al. [21] showed the influence of the environmental wind conditions on the top speed of a racebike. They modelled a three-dimensional turbulent wind field for a straight-line acceleration of a racebike. The simulations carried out show a big effect of the wind speed and the wind direction on the top speed. Influences of environmental turbulence (1) show no worth mentioning effect on the straight-line performance.

The author is convinced that turbulence has an influence on the performance of a racebike as well, especially when caused by (2), like competitors or obstacles. Nevertheless, the effects on the driving performance of a racebike have not yet been proven or found. It is expected that the influence of turbulence will be easier to analyse with the here presented aerodynamic models. Further details of the research on turbulence carried out by the author to date can be found in the Appendix C. Turbulent flow conditions are not considered further in the context of this work.

3.2.3 Upstream Flow Condition Model

The upstream flow velocity vector $\mathbf{v}_{us}$ is the vector sum of the direct opposite of the bike velocity $\mathbf{v}_{bike}$ and the ambient wind speed vector $\mathbf{v}_{wind}$, such that

$$\mathbf{v}_{us} = -\mathbf{v}_{bike} + \mathbf{v}_{wind} \, . \tag{3.26}$$

Fig. 3.5 shows the upstream flow velocity vector in the upstream reference point U of a racebike in leaning conditions. The upstream flow vector can be represented by a vector with the corresponding three velocity components in the body frame

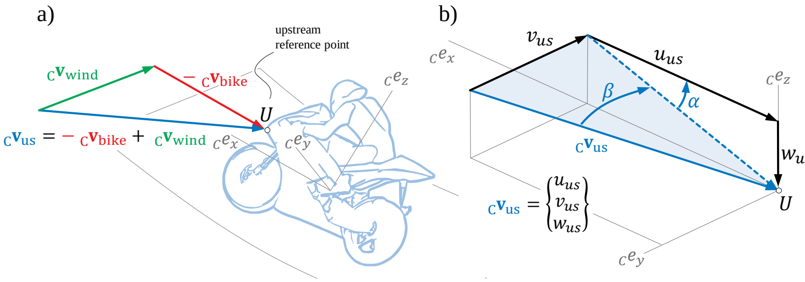

Figure 3.5: Subfigure (a) shows the upstream flow velocity vector as the vector sum of the racebike velocity vector $\mathbf{v}_{bike}$ *and the environmental wind speed vector* $\mathbf{v}_{wind}$*. Subfigure (b) shows the upstream flow velocity vector with its three velocity components in the xyz-direction of the chassis axes and the aerodynamic flow angles* α *and* β *(by Christoph Feichtinger – own work).*

C of reference in body axis, just that

$$_C\mathbf{v}_{us} = \begin{Bmatrix} u_{us} \\ v_{us} \\ w_{us} \end{Bmatrix} . \tag{3.27}$$

Alternatively, the upstream flow vector can be expressed by the magnitude $|\mathbf{v}_{us}|$ often used as v_∞, and the two aerodynamic flow angles α and β, denoted as

$$_C\mathbf{v}_{us} = v_\infty \begin{Bmatrix} -cos\,\alpha\ cos\,\beta \\ sin\,\beta \\ -sin\,\alpha\ cos\,\beta \end{Bmatrix} , \tag{3.28}$$

$$v_\infty = |_C\mathbf{v}_{us}| = \sqrt{u_{us}^2 + v_{us}^2 + w_{us}^2} , \tag{3.29}$$

$$\alpha = arctan\frac{-w_{us}}{u_{us}} \quad \text{and} \quad \beta = arctan\frac{v_{us}}{\sqrt{u_{us}^2 + w_{us}^2}} . \tag{3.30}$$

Thereby α is the angle of attack – from the racebike point of view this means if the upstream flow velocity is coming from above or below. The second aerodynamic flow angle β means the incident flow angle – this means whether the upstream flow velocity is coming from left or right. For completely windless conditions ($\mathbf{v}_{wind} = 0$), the upstream flow vector simplifies to

$$_C\mathbf{v}_{us} = -_C\mathbf{v}_{bike} . \tag{3.31}$$

3.3 Elementary Aerodynamics

The word *Aerodynamic* is derived from the two Greek words for air (*aerios*) and force (*dynami*). Aerodynamics is a subfield of fluid dynamics that deals with moving, gaseous fluids. A fluid, like air, in general is viscous and compressible. Depending on the flow velocity, some aerodynamic flows can be considered incompressible. The air speed of interest from an aerodynamic perspective is the relative flow velocity v_∞. The Mach number is the ratio of the flow velocity to the speed of propagation of sound c, just that

$$Ma = \frac{v_\infty}{c}\,. \tag{3.32}$$

With a maximum flow velocity which is actually achievable for racebikes, of $v_\infty \sim 100\,m/s$ and the speed of propagation of sound at $20°C$ of $c = 343\,m/s$, the Mach number results in

$$Ma = \frac{100}{343} = 0.29 < 0.3\,. \tag{3.33}$$

In normal cases, compressible effects do not play a role for $Ma < 0.3$, which is why the flows considered in the present thesis can be treated as incompressible.

Fig. 3.6 shows the upstream flow velocity and the flow around a body. The flow field around a body can be divided into two main regions.

- The region close to the solid walls of the body which is called the **boundary layer** or the near-wall region, and
- the far field or **free-stream region**, where the air can be considered as non-viscous.

Within the boundary layer the air must be accelerated from zero velocity at the wall to the surrounding far field air speed. In this region viscosity plays a major role. The total aerodynamic forces and moments acting on the body are the sum of the surface pressure p and the wall shear stress τ_w. As sketched in Fig. 3.6, p acts normal to the surface and τ_w acts tangential to the surface. No matter how complex the body shape may be, the basic mechanisms of the acting aerodynamic forces and moments are due to the pressure and shear stress distribution over the body surface. The pressure p and the shear stress τ_w have the dimensions of a force per unit area. The pressure is a scalar point quantity of the fluid which is by definition directionless – or in other words: *acting in all directions*. The pressure should not be interpreted in the same way as the generally accepted understanding of the pressure force, which turns into a directional vector quantity when projected on a surface element. Using the example of the drag force, the total drag of a profile

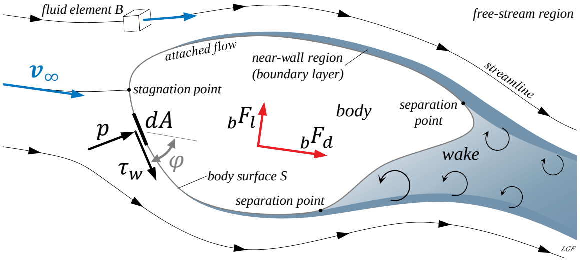

Figure 3.6: Aerodynamic mechanisms for the flow around a bluff body with corresponding streamlines. The figure shows the pressure p and shear stress τ_w for a surface element dA on the body. The boundary layer is attached at the forefront part of the body and separates at the rear edges of the body resulting in the wake area (by Christoph Feichtinger – own work).

or a body is obtained as the sum of the projections of both drag forces into the direction of the oncoming flow velocity v_∞ written as

$$F_d = F_{dp} + F_{df}, \tag{3.34}$$

with the pressure force component F_{dp} and the friction force component F_{df}. They are defined as

$$F_{dp} = \oint p\, cos\varphi\, dA \quad \text{and} \quad F_{df} = \oint \tau_w\, sin\varphi\, dA\,, \tag{3.35}$$

where dA denotes an infinitesimal surface element area on the body and φ is the angle between the surface normal direction and the direction of the upstream flow velocity v_∞. The contribution of each component strongly depends on the shape of the considered body and the body orientation relative to the direction of the free stream velocity. Fig. 3.7 exemplary shows the contributions of the pressure drag and the viscous drag for six different types of bodies.

The jagged geometry of a racebike is shown in Fig. 3.8. With the rider on it, the overall racebike and rider system has rarely smooth surfaces to generate viscous forces. Thus, it is mainly causing pressure forces. Therefore, a racebike (subfigure b) could be classified between the transverse flow on a flat plate (subfigure a) and a sphere (subfigure c) shown in Fig. 3.7.

For the use of aerodynamic forces in mechanical analyses, a dimensionless representation of the forces has become widely accepted. The forces depend on the geometry of the body and its orientation relative to the oncoming flow. The geometric representatives are the projected area A_x or a reference length l_{ref}, which

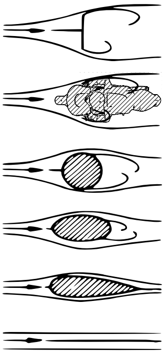

		pressure drag	viscous drag
a)	cross-flow plane plate	100%	0%
b)	racebike	95%	5%
c)	sphere	90%	10%
d)	ellipsoid	60%	40%
e)	airfoil	10%	90%
f)	long-flow plane plate	0%	100%

Figure 3.7: Contributions of the pressure drag and the viscous drag for different bodies (a, c, d, e and f by Hucho [31], racebike b added by Christoph Feichtinger – own work).

is typically the wheelbase for ground-based vehicles. The aerodynamic forces are strongly influenced by the acting pressure at the rear surface area as a result of the oscillations of the wake area due to separations and mixing mechanism between the low-pressure wake region, the boundary layer and the free-stream speed. The wake areas of two distinct riding situations are shown in the lower pictures in Fig. 3.8. For a straight upstream flow, the wake area tends to be small. For an incident flow angle β the wake area is getting bigger, as the flow separates on the outer edges of the racebike and the rider.

A characterization for the nonstationary features and the oscillation mechanisms is the vortex shedding frequency f_v. Therefore, the force experienced by a solid body may be written in dependence of the following variables:

$$A_x,\ l_{ref},\ v_\infty,\ \alpha,\ \beta,\ \rho_{air},\ \nu_{air},\ f_v\,. \tag{3.36}$$

These variables are used to define dimensionless quantities for the characterization of the aerodynamic forces and moments (see Eq. 4.50). The flow field itself can be characterized by the Reynolds number and the Strouhal number. The Reynolds number is the ratio of inertial forces to viscous forces within a fluid defined as

$$Re_\infty = \frac{v_\infty\, l_{ref}}{\nu_{air}} \quad \dots \quad \frac{\text{Inertial Forces}}{\text{Viscous Forces}}\,. \tag{3.37}$$

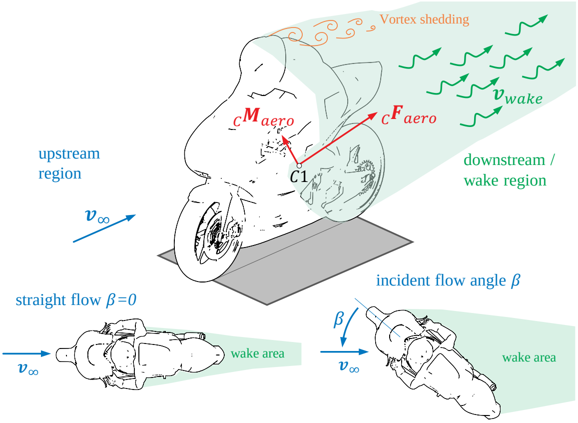

Figure 3.8: Aerodynamic areas of interest showing the upstream flow velocity, the racebike with the aerodynamic forces and moments and the downstream or wake speed. The lower pictures show the wake areas of two distinct riding situations for straight line and for a incident flow angle β (by Christoph Feichtinger – own work).

For comparability with literature values the Reynolds number can be used as representative of the bike speed for a defined reference length l_{ref} and kinematic viscosity of the air ν_{air}. A sphere is a good analogy in terms of the generally bad aerodynamic characteristics of a racebike. Fig. 3.9 shows the drag coefficient of a sphere presented by Hoerner [30] for varying Reynolds numbers. The figure shows the so called *drag crisis*, the characteristic drop of the drag coefficient when reaching the critical Reynolds number, see Fung [24]. This corresponds to the point where the flow pattern changes, leaving a narrower turbulent wake. The behaviour is highly dependent on small differences in the condition of the surface of the sphere.

The *drag crisis* on a sphere goes along with a rise of the vortex shedding frequency f_v. The dimensionless frequency is called the Strouhal number [57], denoted as

$$Sr = \frac{f_v\, l_{ref}}{v_\infty} \quad \dots \quad \frac{\text{Local Acceleration Forces}}{\text{Convective Forces}}\,. \tag{3.38}$$

The Strouhal number is useful for analysing unsteady, oscillating flow problems. The principle of the vortex shedding can be for example observed behind a stone in a river. For a racebike the vortex shedding in straight line motion is mainly driven

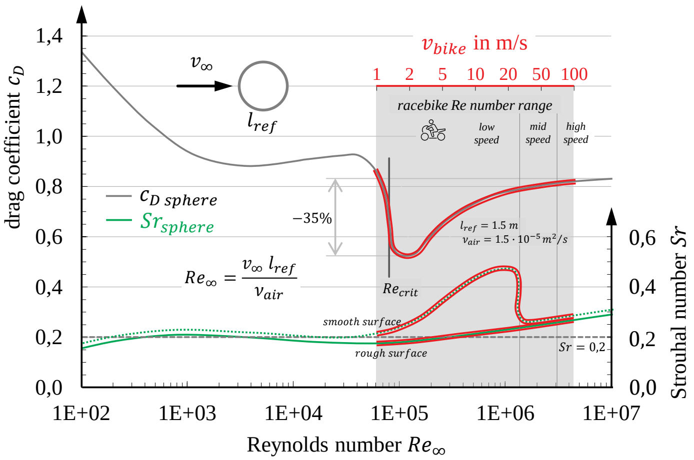

Figure 3.9: Drag coefficient and Strouhal number versus Reynolds number for a long cylinder or a sphere. Data from Hoerner [30], Lienhard [37], Achenbach and Heinecke [1] and Roshko [55]. The grey box shows overlayed the Reynolds number range of a racebike (by Christoph Feichtinger – own work).

by the separation edges of the fairing and the rider. Different flow situations can occur under varying lean angles or incident flow angles, where the vortex shedding can occur on the smooth shapes of the top fairing and the lower fairing, see Fig. 3.8. Fig. 3.9 additionally shows measurements of the Strouhal number on spheres, carried out by Hoerner [30]. For most applications, a Strouhal number value of $Sr = 0.2$ can be used to estimate the vortex shedding frequency f_v for a given reference length and upstream speed. This is often used to define the simulation time for unsteady, numerical flow simulations (e.g. Large Eddy Simulations), to capture at least one complete period of vortex shedding, see Feichtinger [19]. For racebikes there are no Strouhal number measurements available. The Reynolds numbers of the racebike can be calculated with a speed range of $v_{bike} = 0 \cdots 100\,m/s$, the wheelbase of the racebike as reference length ($l_{ref} = 1.5\,m$) and the kinematic viscosity $\nu_{air} = 1.5 \cdot 10^{-5}\,m^2/s$. The Reynolds number range of a racebike is displayed in the grey box in Fig. 3.9. The drag characteristic of a racebike is expected to be similar to that of a sphere, as the ratio of pressure and frictional drag is in a similar range. Using this assumption, the red lines in Fig. 3.9 should make it clear that the drag characteristics and the vortex shedding behaviour varies significantly in the Reynolds number range shown for racebikes.

3.4 Tire Model

The tire provides the only contact to the ground. Therefore, it is responsible to drive the motorbike, to transfer side forces and to transmit road unevenness.

3.4.1 Tire Geometry and the Position of the Contact Patch

The road-tire contact point W is the idealized connection between the road and the tire, and respectively, the racebike. The tire geometry is shown in Fig. 3.10 with the tire velocities and the tire lean angle φ. The rotational velocity is denoted as ω. The longitudinal and lateral velocities in the road-tire contact point W are indicated by v_x and v_y. The slip angle λ is the angle between v_x and v_y. The effective tire radius of the free rolling wheel can be approximated by (see Eichberger [17])

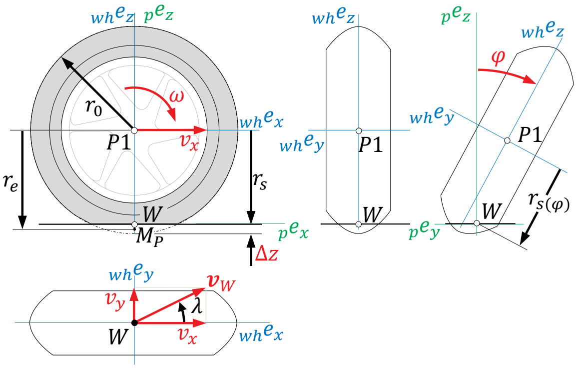

Figure 3.10: Tire geometry and tire velocities.

$$r_e \approx \frac{2}{3} r_0 + \frac{1}{3} r_s \,, \tag{3.39}$$

where r_0 is the undeformed tire radius and r_s is the static tire radius. With the relation $r_0 = r_s + \Delta z$, the effective tire radius results in

$$r_e \approx r_0 - \frac{1}{3} \Delta z \,, \tag{3.40}$$

where Δz is the radial deflection.

3.4.2 Wheel slip calculation

Longitudinal slip For a rolling wheel without brake or drive torques, the relation between the longitudinal and rotational speed can be written as

$$v_x = r_e \, \omega \, . \tag{3.41}$$

For a driven wheel, the statement of Eq. 3.41 is no longer valid. Instead, the following applies:

$$v_x < r_e \, \omega \, . \tag{3.42}$$

With this the longitudinal drive slip is denoted as

$$s_{x\,drive} = \frac{r_e \, \omega - v_x}{r_e \, |\omega|} = 0 \cdots 1 \, . \tag{3.43}$$

For a rolling wheel, the drive slip results in a value of $s_{x\,drive} = 0$ by using Eq. 3.41. For a spinning wheel, the longitudinal velocity $v_x = 0$. Thus, the drive slip has a value of $s_{x\,drive} = 1$.

For a braked wheel the longitudinal velocity is bigger than the rotational velocity, just that

$$v_x > r_e \, \omega \, . \tag{3.44}$$

Therefore, the longitudinal brake slip is defined as

$$s_{x\,brake} = \frac{r_e \, \omega - v_x}{|v_x|} = -1 \cdots 0 \, . \tag{3.45}$$

For a blocked wheel, the rotational speed $\omega = 0$. This results in a brake slip value of $s_{x\,brake} = -1$.

Lateral slip In principle, the frictional connection in the transverse direction behaves in a similar way to that in the longitudinal direction. For a driven wheel, the lateral slip is written as

$$s_{y\,drive} = \frac{v_y}{r_e \, |\omega|} \, , \tag{3.46}$$

with the lateral velocity of the tire v_y. In the same way, the lateral slip for a braked wheel is denoted as

$$s_{y\,brake} = \frac{v_y}{|v_x|} \, . \tag{3.47}$$

The lateral slip can be alternatively represented by the lateral slip angle λ, just that

$$\lambda = \arctan \, s_y \, , \tag{3.48}$$

by using the corresponding lateral drive or brake slip.

3.4.3 Contact Forces between the Tire and the Road

The interaction of the tire with the road can be represented by a system of three forces and three moments. Fig. 3.11 shows the following acting forces and moments

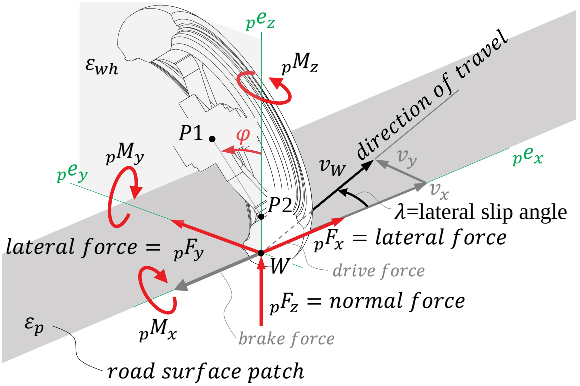

Figure 3.11: Contact forces and moments between the tire and the road acting in the road-tire contact point W.

acting in the idealized road-tire contact W:

- a longitudinal force $F_x = {}_pF_x$ in x-direction, responsible to transmit drive and brake forces through the road surface patch;
- a lateral force $F_y = {}_pF_y$ in y-direction, orthogonal to the longitudinal force in y-direction;
- a vertical force $F_z = {}_pF_z$ orthogonal to the road surface patch along the z-axis;
- an overturning moment $M_x = {}_pM_x$ around the x-axis;
- the wheel torque $M_y = {}_pM_y$ around the y-axis;
- a restoring moment $M_z = {}_pM_z$ around the z-axis.

The longitudinal and lateral tire forces are acting in the road surface patch plane. They are often normalized by the vertical force F_z, just that

$$F_{x\,norm} = \frac{F_x}{F_z} \quad \text{and} \quad F_{y\,norm} = \frac{F_y}{F_z}\,. \tag{3.49}$$

3.4.4 Tire modelling in vehicle dynamics

For the use in vehicle dynamics, the tire forces and moments have to be calculated based on the kinematic input parameters of the tire. The following Tab. 3.2 shows the necessary kinematic input parameters and the calculated dynamic tire forces and moments as output of handling tire models, with respect to Eichberger [17].

Table 3.2: Input and output parameters of the tire model (see Eichberger [17])

input (kinematic)				**output (dynamic)**
radial deflection	Δz		F_x	longitudinal force
longitudinal velocity	v_x		F_y	lateral force
lateral velocity	v_y	$\Rightarrow$	F_z	contact/vertical force
rotational speed	ω		M_x	overturning moment
effective tire radius	r_e		M_y	wheel torque
local lean angle	φ		M_z	restoring torque

Additional effects like tire temperature and tire pressure are not considered within the present work. In general, there are two main types of tire models available:

- physical tire models and
- mathematical tire models.

Physical tire models approximate the contact force mechanisms by a physical modelling of the adhesion and deformation effects. Although, physical models can give a deep insight into the physical mechanisms, they are mainly used in tire research. Mathematical tire models approximate measured forces and moments by suitable approximation functions. For vehicle dynamics, mainly mathematical tire models are used.

Longitudinal Tire Forces Fig. 3.12 shows a typical normalized longitudinal force characteristics $F_{x\,norm}$ plotted against the longitudinal slip s_x with reference to Eichberger [17]. The longitudinal tire force characteristic shows three areas.

a) The linear force-slip area,

b) the transition area, where the longitudinal force reaches its maximum and the tire increasingly starts to slide, and

c) the saturation area which is characterized by a sliding of the tire on the road.

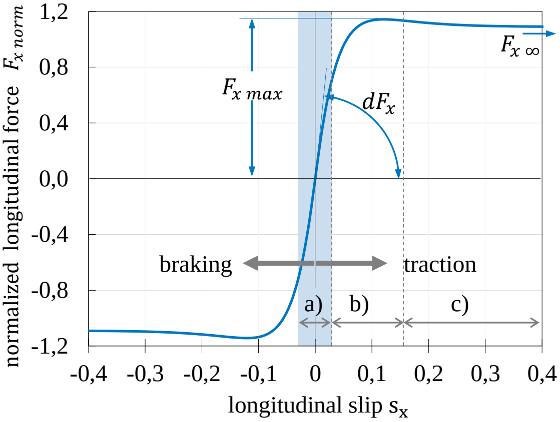

Figure 3.12: Mathematical approximation function of the normalized longitudinal tire force $F_{x\,norm}$ plotted against the longitudinal slip s_x with reference to Eichberger [17].

The most widely used tire model is the *Magic Formula* model from Pacejka [48]. The approach of Pacejka is based on a empirical fit of approximation functions to tire force measurements. The Model was named *Magic Formula*, because there is no particular physical basis existing for the structure of the equations. The popularity of the model is because it is available for a wide range of automotive tires. No sufficient Pacejka model parametrization exists for motorbike tyres at high lean angles.

Alternative tire models are TMeasy by Rill [25] and TMsimple presented by Hirschberg [29]. Both models are mathematical models. In contrast to the *Magic Formula*, these models are based on easier and simpler to understand tire parameters. With reference to Fig. 3.12 the physical tire parameters are:

- the initial gradient dF_x,
- the maximum longitudinal tire force $F_{x\,max}$ and
- the longitudinal saturation force $F_{x\,\infty}$.

The parameters are used to calculate the coefficients of the tire model TMsimple

$$F_x = K\,sin\left[B\left(1 - e^{\frac{-|s_x|}{A}}\right)sign\,s_x\right]. \tag{3.50}$$

With

$$K = F_{x\,max},\ B = \pi - \arcsin\frac{F_{x\,\infty}}{F_{x\,max}},\ A = \frac{1}{dF_x}KB;\ (F_{x\,\infty} \leq F_{x\,max})\,. \qquad (3.51)$$

Lateral Tire Forces The lateral tire force of a motorcycle tire depends on both the lateral slip angle λ and the lean angle φ. Cossalter [12] provides a deep insight into the lateral dynamics of motorcycle tires. He investigated the effects of lateral tire forces separately. Fig. 3.13 shows measurements of the normalized lateral force carried out by [12] for a superbike front tire (SBK 120/75R17) and rear tire (SBK 190/65R17).

- left subfigure: Lateral force as a function of the lateral slip angle at a lean angle $\varphi = 0$.
- right subfigure: Lateral force as a function of the lean angle φ at a lateral slip angle $\lambda = 0$.

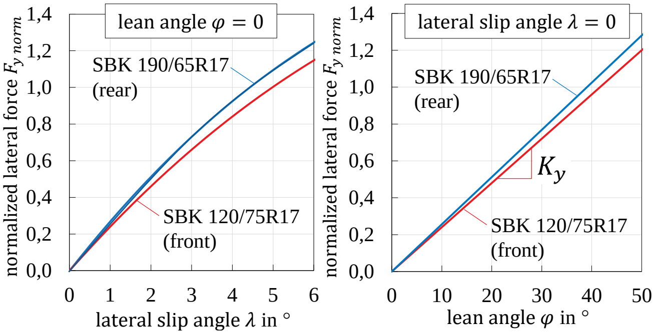

Figure 3.13: Lateral tire force as a function of the lean angle φ (right) and of the lateral slip angle λ (left) for a front and a rear tire. Measurements carried out by Cossalter [12] for a superbike front tire (SBK 120/75R17) and rear tire (SBK 190/65R17).

Furthermore, Cossalter investigated the lateral tire force needed for motorcycle equilibrium in a curve. Without any further details, the key message for the present work is that:

> *The tire's ideal behaviour occurs when the slip angle is zero, that is, when the lateral force necessary for equilibrium is produced by the lean angle alone* (Cossalter [12] page 54).

It is assumed that a racebike, ridden by a professional racerider, is always close to the optimum or at the limit of the tires.

Within the present work, the lean angle is used for the calculation of the lateral tire force. The measurements of Cossalter for superbike tires are like the Dunlop tires used in Moto2. Assuming a linear relation like shown in Fig. 3.13, the normalized lateral force can be written as

$$F_{y\,norm} = K_y\,\varphi\,. \tag{3.52}$$

K_y is the slope of the lateral tire force over the lean angle.

Combined longitudinal and lateral tire forces The combined tire forces can be displayed in the tire friction ellipse, see Fig. 3.14. It shows the longitudinal and lateral tire force limits. The resultant of the longitudinal and lateral tire forces must be within the friction ellipse. The maximum values of the longitudinal force F_{x0} and of the lateral force F_{y0} show the maximum tire forces when they act alone in longitudinal and lateral direction. To take the friction ellipse limit into account the maximum admissible lateral force is obtained by a scaling coefficient. With reference to Cossalter [12], the correction coefficient depends on the longitudinal force applied, just that

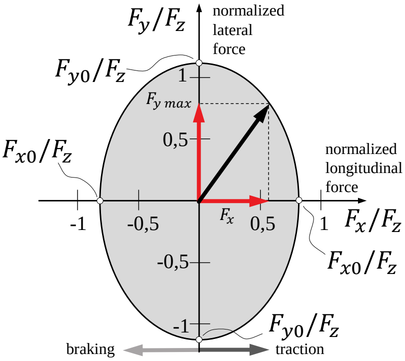

Figure 3.14: Tire friction ellipse.

$$C_{Lat} = \sqrt{1 - \left(\frac{F_x}{F_{x0}}\right)^2}\,. \tag{3.53}$$

With this the maximum available lateral tire force is denoted as

$$F_y = F_{y\,max} = C_{Lat}\,F_{y0}\,. \tag{3.54}$$

This ensures that the resulting force vector lies on the friction ellipse.

Chapter 4

Physical Racebike Model

4.1 Racebike and Rider Description

The racebike is modelled as a multibody system of six rigid bodies. Fig. 4.1 shows the physical racebike model with the single bodies. The bodies have mass and inertia and are connected with massless coupling elements (springs, dampers, active elements) as well as idealized connections (joints, guides). The six mass bodies are:

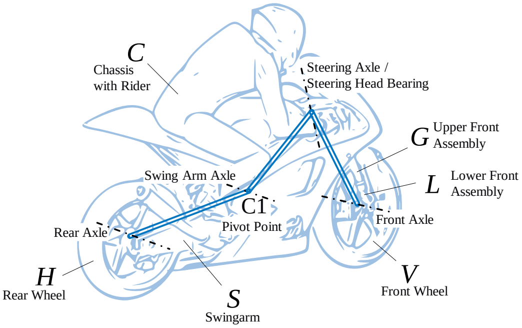

Figure 4.1: The Components of the physical racebike model (by Christoph Feichtinger – own work).

Chassis (C) The chassis is the main part of the motorbike, which holds the engine, the airbox, the fairing, the cooling system, and the seat together via a frame. The rider is attached to the chassis. The dynamic influence of the rider movement on the racebike is modelled by specific parameters for different, segmented riding situations.

Swingarm (S) The swing arm is mounted to the chassis in the pivot point $C1$ and is additionally connected to the chassis with a suspension system. The simulation model of the swingarm considers the swingarm, the suspension system and the rear brake calliper from a mass and inertia point of view. The reaction moments from braking and engine torques on the swingarm are not considered.

Upper Front Assembly (G) The upper front assembly is the part which is mounted to the chassis by the steering head bearing. The steering head bearing also holds the lower and upper triple clamp which is the connection to the fork and the handlebars. The fork is split up into the fork tubes and the slider tubes. The common fork type in racebikes is the upside-down fork [9] where the upper fork tubes (fixed to the triple clamp), have a larger diameter than the lower slider tubes. Therefore, the fork tubes, the triple clamps and the steering head bearing are the parts of the upper front assembly.

Lower Front Assembly (L) The lower front assembly are the slider tubes of the fork, the fork fists, and the front brake callipers.

Wheels (V,H) The wheel assemblies include the axles, the rims, the tires, and the brake discs. The front and rear wheel are mounted to the swingarm and the fork fists with the axles.

Stiffness Modelling of the individual Bodies The flexibility and stiffness of single components is essential for the race rider to get the right feeling for its individual riding style. Small changes of the stiffness of single components can have a big influence for professional race rider from a lap time point of view.

Previous works of Cossalter [12] and Limembeer [38] modelled the single components as flexible elements. Cossalter [12] presented numbers for torsional and lateral stiffness of rear and front assemblies of a motorcycle. The lateral and torsional stiffness, are defined by the ratios

$$K_{lat} = \frac{F}{\triangle y} \quad and \quad K_{tors} = \frac{F}{\alpha}\,, \tag{4.1}$$

where F is the lateral load in the wheel point, $\triangle y$ the lateral deformation of the wheel point and α the wheel plane deflection. The measurements on the rear assembly were carried out with a locked steering head and a lateral and torsional load on a stiff rear wheel.

- The lateral load is a force acting in y-direction.
- The torsional load is a moment applied around the x-axis.

The measurements on the front assembly were carried out with a blocked steering head, with a lateral and torsional load applied to a stiff front wheel. The stiffness measurements on the swingarm were made with a locked swingarm pivot axle and a lateral and torsional load applied to the rear wheel axle. The stiffness measurements of the front fork were carried out with a locked steering head and a lateral and torsional load applied to the front wheel axle. Tab. 4.1 shows stiffness value ranges for a modern motorcycle (sport $1000\,cc$), without the compliance of the tire.

Table 4.1: Stiffness value ranges for assembly groups of a modern motorcycle (sport $1000\,cc$), without the compliance of the tire (Cossalter [12]).

assembly	**lateral stiffness** K_{lat} in kN/mm	**torsional stiffness** K_{tors} in $kN/°$
rear assembly	$0.10 - 0.20$	$1.50 - 3.00$
front assembly	$0.08 - 0.16$	$0.70 - 1.40$
swingarm	$0.80 - 1.60$	$1.00 - 2.00$
front fork	$0.07 - 0.18$	$0.10 - 0.30$

The influence of the flexibility on the position and orientation of the single racebike components is assumed to be much smaller than the position and orientation values itself. The focus of the present work is on the aerodynamics of the racebike in real riding situations. Therefore, the single mass bodies are modelled as rigid components with defined mass and inertia properties.

4.2 Racebike Orientation and Position

Fig. 4.2 shows the racebike orientation and position in the inertial frame of reference I. The orientation of the chassis-fixed axis system C in the inertial frame of reference I is defined by the transformation matrix $\mathbf{A}_{IC}$ or $\mathbf{A}_{CI}$. The transformation matrix can be formed as the product of three simple rotation matrices for the individual Euler angles (Eqs. 3.4 and 3.8). A transformation matrix with Euler angles can have singular values for specific combinations of the single Euler angles. Therefore, a problem-free description of any three-dimensional rotary movement is not possible with the Euler angles.

Singularities do not occur when using Euler parameters of the quaternion representation (Eq. 3.5). The four Euler parameters in vector notation are given

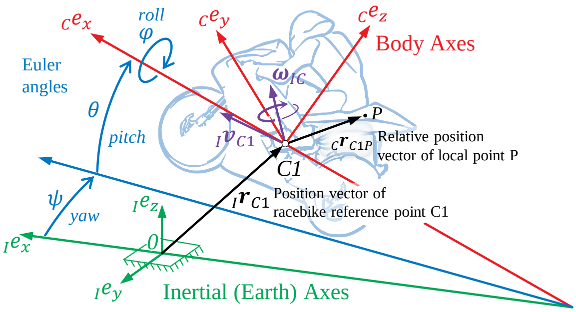

Figure 4.2: Racebike orientation and position. Euler angles define the transformation matrix $\mathbf{A}_{IC}$ or $\mathbf{A}_{CI}$ between racebike (C) and inertial (I) axis system. The translational and rotational velocity vectors ${}_I\mathbf{v}_{C1}$ and $\boldsymbol{\omega}_{IC}$. Racebike velocities and relative position vector of a local point P are also shown (by Christoph Feichtinger – own work).

by

$$\mathbf{p}_{EIC}^T = \left\{e_{0IC} \quad e_{1IC} \quad e_{2IC} \quad e_{3IC}\right\}^T . \tag{4.2}$$

By using Eq. 3.9 and Eq. 3.8, the transformation matrix with the Euler parameters results in

$$\mathbf{A}_{IC} = \begin{bmatrix} e_0^2 + e_1^2 - e_2^2 - e_3^2 & 2\,e_1\,e_2 - 2\,e_0\,e_3 & 2\,e_0\,e_2 + 2\,e_1\,e_3 \\ 2\,e_0\,e_3 + 2\,e_1\,e_2 & e_0^2 - e_1^2 + e_2^2 - e_3^2 & 2\,e_2\,e_3 - 2\,e_0\,e_1 \\ 2\,e_1\,e_3 - 2\,e_0\,e_2 & 2\,e_0\,e_1 + 2\,e_2\,e_3 & e_0^2 - e_1^2 - e_2^2 + e_3^2 \end{bmatrix} . \tag{4.3}$$

The position of the racebike reference point $C1$ with respect to the inertial frame of reference is defined by the longitudinal, lateral, and vertical position, just that

$${}_I\mathbf{r}_{C1} = \left\{x_C \quad y_C \quad z_C\right\}^T . \tag{4.4}$$

An arbitrary point on the racebike (P) is known in the chassis axis system C. The position of the point P in the inertial frame of reference needs to be evaluated as

$${}_I\mathbf{r}_P = {}_I\mathbf{r}_{C1} + \mathbf{A}_{IC}\,{}_C\mathbf{r}_{C1P} . \tag{4.5}$$

4.3 Racebike Velocities

The angular velocity vector of the racebike reference axis system C with respect to the inertial frame of reference is defined by three angular velocities, written as

$$\boldsymbol{\omega}_{IC} = \left\{\omega_{xC} \quad \omega_{yC} \quad \omega_{zC}\right\}^T . \tag{4.6}$$

The angular velocity vector in the body frame of reference can be calculated from the time derivative of the Euler parameter vector $\dot{\mathbf{p}}_{EpC}$ and the Euler parameter matrix $\mathbf{L}_{IC(\mathbf{p}_{EIC})}$ with reference to Eq. 3.9, just that

$$\boldsymbol{\omega}_{IC} = 2\,\mathbf{L}_{IC(\mathbf{p}_{EIC})}\,\dot{\mathbf{p}}_{EIC}\,. \tag{4.7}$$

The velocity vector of the reference point $C1$ in the inertial frame of reference is defined by the three velocity components in longitudinal, lateral, and vertical direction. Thus, the velocity vector can be denoted as

$$_{I}\mathbf{v}_{C1} = \begin{Bmatrix} u_C & v_C & w_C \end{Bmatrix}^T\,. \tag{4.8}$$

The velocity of point P in the inertial frame of reference is defined as

$$_{I}\mathbf{v}_{P} = {}_{I}\mathbf{v}_{C1} + \boldsymbol{\omega}_{IC} \times {}_{I}\mathbf{r}_{C1P}\,. \tag{4.9}$$

4.4 Racebike Geometry and Kinematic

Fig. 4.3 shows the physical racebike model geometry and the kinematic relations. There is no flexibility within the single bodies. A body-fixed axis system is attached to each rigid body. The movements are represented by the following coupling elements and connections:

- The swingarm and the chassis are connected via a bearing in the pivot point $C1$ with the rear shock and linkage, represented by a torsion spring and a torsion damper unit around the swing arm axis $_{C}e_{y}$. The swing arm axis system is rotated around the y-axis $_{C}e_{y}$ by the angle θ_S.
- The rear wheel is attached to the swingarm in the rear wheel axle $_{S}e_{y}$ through the point $H1$.
- The rear wheel axis system F is rotated around the rear wheel axle $_{S}e_{y}$ by the angel θ_H.
- The rear wheel road normal axis system H is rotated around the x-axis $_{F}e_{x}$ by the local lean angle φ_H.
- The rear wheel deflection normal to the road surface in the contact point is defined by s_H.
- The steering head bearing is placed in the chassis fixed point $C2$. The steering head bearing axis system L is rotated by the angle κ around the y-axis of the chassis $_{C}e_{y}$.

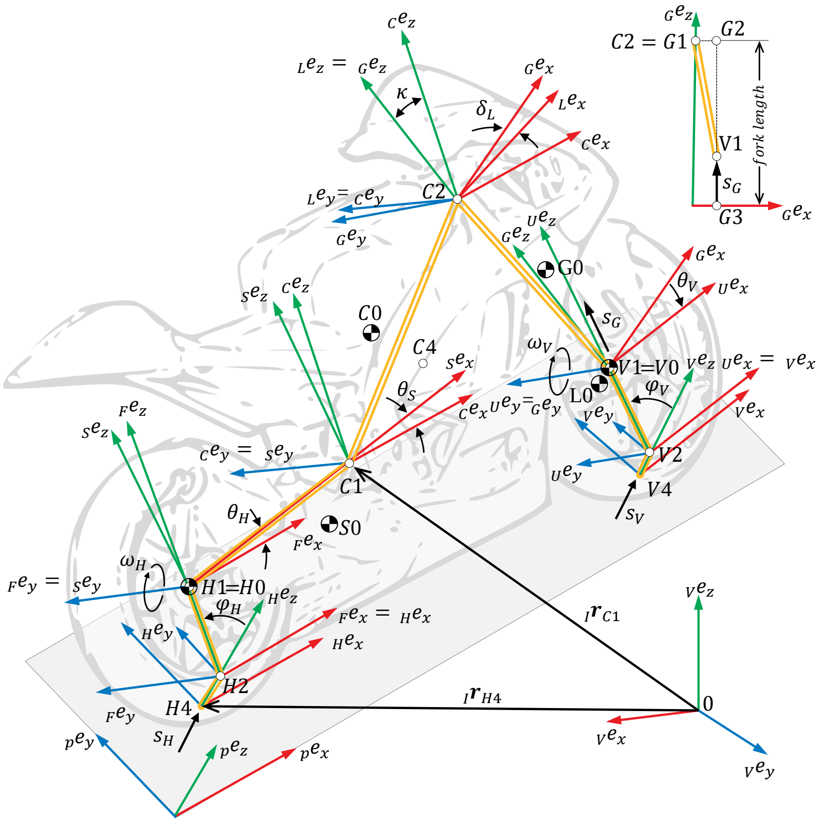

Figure 4.3: Racebike model geometry and kinematic (by Christoph Feichtinger – own work).

- The upper front assembly is mounted to the chassis with the steering head bearing in point $C2$ and is rotating with the angle δ_L around the steering axis $_Le_z$. The front assembly axis system is denoted by G.

- The lower front assembly is attached to the upper front assembly via the front fork. The front fork length defines the point $G3$ – This is the fully extended front fork.

- The front suspension stroke s_G defines the compression of the front fork acting in the z-direction ${}_Ge_z$.
- The front wheel is attached to the lower front assembly in the point $V1$ and is rotating around the front wheel axle ${}_Ge_y$. The front wheel axis system U is rotated around the front wheel axle ${}_Ge_y$ by the angle θ_V.
- The front wheel road normal axis system V is rotated around the x-axis ${}_Ue_x$ by the local lean angle φ_V.
- The front wheel deflection normal to the road surface in the contact point is defined by s_V.

4.5 Equation of Motion – Jourdain Principle

The equation of motion of the racebike model was developed using Jourdains principle [53]. Jourdains principle is using generalized coordinates, generalized velocities and generalized accelerations.

Generalized Coordinate Vector The generalized coordinate vector for the racebike model is denoted as

$$\mathbf{y} = \{\underbrace{x_C\ y_C\ z_C}_{position}\ \underbrace{e_{0IC}\ e_{1IC}\ e_{2IC}\ e_{3IC}}_{orientation}\ \underbrace{\theta_S\ \delta_L\ s_G\ \theta_V\ \theta_H}_{kinematic}\}^{\mathrm{T}}, \tag{4.10}$$

with the position, the orientation, and the kinematic quantities.

Generalized Velocity Vector The generalized velocity vector of the racebike model reads

$$\mathbf{z} = \{\underbrace{u_C\ v_C\ w_C}_{translation}\ \underbrace{\omega_{xC}\ \omega_{yC}\ \omega_{zC}}_{rotation}\ \underbrace{\dot\theta_S\ \dot\delta_L\ \dot s_G\ \omega_V\ \omega_H}_{kinematic}\}^{\mathrm{T}}. \tag{4.11}$$

Time Derivative of the Generalized Coordinate Vector The time derivative of the generalized coordinate vector reads

$$\dot{\mathbf{y}} = \{\underbrace{u_C\ v_C\ w_C}_{translation}\ \underbrace{\dot e_{0IC}\ \dot e_{1IC}\ \dot e_{2IC}\ \dot e_{3IC}}_{rotation}\ \underbrace{\dot\theta_S\ \dot\delta_L\ \dot s_G\ \omega_V\ \omega_H}_{kinematic}\}^{\mathrm{T}}. \tag{4.12}$$

Although $\dot{\mathbf{y}}$ is a generalized velocity vector, it has a different length than the generalized velocity vector. This is through the fact, that the three-dimensional orientation of the racebike is represented by four Euler parameters, while the three-dimensional rotation is represented by three angular velocities.

Generalized Acceleration Vector The generalized acceleration vector of the racebike model reads

$$\dot{\mathbf{z}} = \{\underbrace{a_{Cx} \;\; a_{Cy} \;\; a_{Cz}}_{translation} \;\; \underbrace{\dot{\omega}_{xC} \;\; \dot{\omega}_{yC} \;\; \dot{\omega}_{zC}}_{rotation} \;\; \underbrace{\ddot{\theta}_S \;\; \ddot{\delta}_L \;\; \ddot{s}_G \;\; \dot{\omega}_V \;\; \dot{\omega}_H}_{kinematic}\}^{\mathrm{T}} , \tag{4.13}$$

with the translational, rotational, and kinematic acceleration quantities.

4.5.1 Center of Gravity Position Vectors

The center of gravity position vector of every single body is calculated using Eq. 4.5. The single center of gravity position vectors in the inertial frame of reference are denoted in the following paragraphs.

Chassis The chassis center of gravity position in the inertial frame of reference is denoted as

$$_I\mathbf{r}_{C0(\mathbf{y})} = {_I\mathbf{r}_{C1}} + \mathbf{A}_{IC}\, {_C\mathbf{r}_{C1C0}} \, . \tag{4.14}$$

$_C\mathbf{r}_{C1C0}$ is the center of gravity position of the chassis in the chassis axis system, written as

$$_C\mathbf{r}_{C1C0} = \begin{Bmatrix} x_{C1C0} \\ 0 \\ z_{C1C0} \end{Bmatrix} . \tag{4.15}$$

Swingarm The swingarm center of gravity position in the inertial frame of reference is given by

$$_I\mathbf{r}_{S0(\mathbf{y})} = {_I\mathbf{r}_{C1}} + \mathbf{A}_{IS}\, {_S\mathbf{r}_{S1S0}} \, . \tag{4.16}$$

$_S\mathbf{r}_{S1S0}$ is the center of gravity position of the swingarm in the swingarm axis system, written as

$$_S\mathbf{r}_{S1S0} = \begin{Bmatrix} x_{S1S0} \\ 0 \\ z_{S1S0} \end{Bmatrix} . \tag{4.17}$$

The transformation matrix $\mathbf{A}_{IS}$ reads

$$\mathbf{A}_{IS} = \mathbf{A}_{IC}\, \mathbf{A}_{CS} \, , \tag{4.18}$$

where $\mathbf{A}_{CS}$ is defined by a y-rotation around the swing arm axle just that

$$\mathbf{A}_{CS} = \begin{bmatrix} \cos\theta_S & 0 & \sin\theta_S \\ 0 & 1 & 0 \\ -\sin\theta_S & 0 & \cos\theta_S \end{bmatrix} . \tag{4.19}$$

Rear Wheel It is assumed that the rear wheel is balanced and therefore the center of gravity is in the middle of the axle. Thus, the rear wheel center of gravity position is denoted as

$$ {}_I\mathbf{r}_{H0(\mathbf{y})} = {}_I\mathbf{r}_{C1} + \mathbf{A}_{IS}\, {}_S\mathbf{r}_{S1S2} \,. \tag{4.20}$$

${}_S\mathbf{r}_{S1S2}$ is the rear wheel axle position in the swingarm axis system, written as

$$ {}_S\mathbf{r}_{S1S2} = \begin{Bmatrix} x_{S1S2} \\ 0 \\ 0 \end{Bmatrix} , \tag{4.21}$$

where x_{S1S2} is called the *swingarm length*.

Upper and Lower Front Assembly, Front Wheel The center of gravity positions of the upper and lower front assembly as well as for the front wheel are complicated mathematical expressions. Therefore, they are not listed here.

The single vectors are defined as symbolic functions using the MATLAB SYMBOLIC TOOLBOX [41]. For further use, the position vectors are derived as functions of the generalized coordinate vector, written as:

- ${}_I\mathbf{r}_{C0(\mathbf{y})}$ = f_rC0I($\mathbf{y}$) – Chassis (C)
- ${}_I\mathbf{r}_{S0(\mathbf{y})}$ = f_rS0I($\mathbf{y}$) – Swingarm (S)
- ${}_I\mathbf{r}_{G0(\mathbf{y})}$ = f_rG0I($\mathbf{y}$) – Upper Front Assembly (G)
- ${}_I\mathbf{r}_{L0(\mathbf{y})}$ = f_rL0I($\mathbf{y}$) – Lower Front Assembly (L)
- ${}_I\mathbf{r}_{H0(\mathbf{y})}$ = f_rH0I($\mathbf{y}$) – Rear Wheel (H)
- ${}_I\mathbf{r}_{V0(\mathbf{y})}$ = f_rV0I($\mathbf{y}$) – Front Wheel (V)

4.5.2 Center of Gravity Velocity Vectors

The velocity vector of every single body is calculated using Eq. 4.9. For the chassis, the center of gravity velocity vector is denoted as

$$ {}_I\mathbf{v}_{0C(\mathbf{y},\mathbf{z})} = {}_I\mathbf{v}_{0C1} + \mathbf{A}_{IC}\left({}_C\boldsymbol{\omega}_{IC} \times {}_C\mathbf{r}_{C1C0}\right) . \tag{4.22}$$

The center of gravity velocity vectors of the other bodies are complicated mathematical expressions. Therefore, they were derived symbolically using the MATLAB SYMBOLIC TOOLBOX [41]. For further use, the velocity vectors are derived as functions of the generalized coordinate and velocity vectors. Thus, the single center of gravity velocity vectors in the inertial frame of reference are denoted as:

- ${}_{I}\mathbf{v}_{0C(\mathbf{y},\mathbf{z})} =$ f_vC0I$(\mathbf{y},\mathbf{z})$ – Chassis (C)
- ${}_{I}\mathbf{v}_{0S(\mathbf{y},\mathbf{z})} =$ f_vS0I$(\mathbf{y},\mathbf{z})$ – Swingarm (S)
- ${}_{I}\mathbf{v}_{0G(\mathbf{y},\mathbf{z})} =$ f_vG0I$(\mathbf{y},\mathbf{z})$ – Upper Front Assembly (G)
- ${}_{I}\mathbf{v}_{0L(\mathbf{y},\mathbf{z})} =$ f_vL0I$(\mathbf{y},\mathbf{z})$ – Lower Front Assembly (L)
- ${}_{I}\mathbf{v}_{0H(\mathbf{y},\mathbf{z})} =$ f_vH0I$(\mathbf{y},\mathbf{z})$ – Rear Wheel (H)
- ${}_{I}\mathbf{v}_{0V(\mathbf{y},\mathbf{z})} =$ f_vV0I$(\mathbf{y},\mathbf{z})$ – Front Wheel (V)

4.5.3 Body Angular Velocity Vectors

The angular velocity vector of the chassis is denoted as

$${}_{C}\boldsymbol{\omega}_{IC(\mathbf{y},\mathbf{z})} = \begin{Bmatrix} \omega_{xC} \\ \omega_{yC} \\ \omega_{zC} \end{Bmatrix} . \tag{4.23}$$

The angular velocity vectors of the single bodies are derived as symbolic functions as well. The single angular velocity vectors in the respective body reference system are denoted as:

- ${}_{C}\boldsymbol{\omega}_{IC(\mathbf{y},\mathbf{z})} =$ f_omICC$(\mathbf{y},\mathbf{z})$ – Chassis (C)
- ${}_{S}\boldsymbol{\omega}_{IS(\mathbf{y},\mathbf{z})} =$ f_omISS$(\mathbf{y},\mathbf{z})$ – Swingarm (S)
- ${}_{G}\boldsymbol{\omega}_{IG(\mathbf{y},\mathbf{z})} =$ f_omIGG$(\mathbf{y},\mathbf{z})$ – Upper Front Assembly (G)
- ${}_{L}\boldsymbol{\omega}_{IL(\mathbf{y},\mathbf{z})} =$ f_omILL$(\mathbf{y},\mathbf{z})$ – Lower Front Assembly (L)
- ${}_{H}\boldsymbol{\omega}_{IH(\mathbf{y},\mathbf{z})} =$ f_omIHH$(\mathbf{y},\mathbf{z})$ – Rear Wheel (H)
- ${}_{V}\boldsymbol{\omega}_{IV(\mathbf{y},\mathbf{z})} =$ f_omIVV$(\mathbf{y},\mathbf{z})$ – Front Wheel (V)

4.5.4 Partial Derivatives (Jacobi Matrices)

Jourdains principle includes partial derivatives for the calculation of the generalized mass matrix as well as for the calculation of the generalized forces and moments. The result of the partial derivatives is called the Jacobi matrix J_f, just that

$$\mathbf{J}_f := \left(\frac{\partial f_i}{\partial x_j}\right)_{i=1,\dots,m;\ j=1,\dots,n} = \begin{pmatrix} \frac{\partial f_1}{\partial x_1} & \frac{\partial f_1}{\partial x_2} & \cdots & \frac{\partial f_1}{\partial x_n} \\ \vdots & \vdots & \ddots & \vdots \\ \frac{\partial f_m}{\partial x_1} & \frac{\partial f_m}{\partial x_2} & \cdots & \frac{\partial f_m}{\partial x_n} \end{pmatrix} . \tag{4.24}$$

The Jacobi matrix has a size of $m \times n$, where m is the length of the function vector f_i and n is the length of the derivative vector x_j. The specific Jacobi matrices for the racebike model are:

$\partial\mathbf{v}/\partial\mathbf{y}$: The partial derivative of the center of gravity velocity vector with respect to the generalized coordinate vector, just that

$$\mathbf{J}_{vy\,b(\mathbf{y},\mathbf{z})} = \frac{\partial_I \mathbf{v}_{b0(\mathbf{y},\mathbf{z})}}{\partial \mathbf{y}} \quad \cdots \quad \text{for } b = C, S, G, L, H, V\,. \tag{4.25}$$

$\partial\mathbf{v}/\partial\mathbf{z}$: The partial derivative of the center of gravity velocity vector with respect to the generalized velocity vector, just that

$$\mathbf{J}_{vz\,b(\mathbf{y},\mathbf{z})} = \frac{\partial_I \mathbf{v}_{b0(\mathbf{y},\mathbf{z})}}{\partial \mathbf{z}} \quad \cdots \quad \text{for } b = C, S, G, L, H, V\,. \tag{4.26}$$

$\partial\boldsymbol{\omega}/\partial\mathbf{y}$: The partial derivative of the body angular velocity vector with respect to the generalized coordinate vector, just that

$$\mathbf{J}_{\omega y\,b(\mathbf{y},\mathbf{z})} = \frac{\partial_b \boldsymbol{\omega}_{0b(\mathbf{y},\mathbf{z})}}{\partial \mathbf{y}} \quad \cdots \quad \text{for } b = C, S, G, L, H, V\,. \tag{4.27}$$

$\partial\boldsymbol{\omega}/\partial\mathbf{z}$: The partial derivative of the body angular velocity vector with respect to the generalized velocity vector, just that

$$\mathbf{J}_{\omega z\,b(\mathbf{y},\mathbf{z})} = \frac{\partial_b \boldsymbol{\omega}_{0b(\mathbf{y},\mathbf{z})}}{\partial \mathbf{z}} \quad \cdots \quad \text{for } b = C, S, G, L, H, V\,. \tag{4.28}$$

The Jacobi matrices are derived as symbolic functions with the MATLAB SYMBOLIC TOOLBOX for further use.

4.5.5 Apparent Accelerations

The translational and angular apparent acceleration vectors with reference to Eq. 3.22 are denoted for the single bodies as

$${}_I\dot{\mathbf{v}}^S_{0b} = \mathbf{J}_{vy\,b(\mathbf{y},\mathbf{z})}\,\dot{\mathbf{y}} \quad \textit{and} \quad {}_b\dot{\boldsymbol{\omega}}^S_{0b} = \mathbf{J}_{\omega y\,b(\mathbf{y},\mathbf{z})}\,\dot{\mathbf{y}}\,, \tag{4.29}$$

for $b = C, S, G, L, H, V$.

4.5.6 Generalized Mass Matrix

The generalized mass matrix for the motorbike, according to Eq. 4.30 is denoted as

$$\begin{aligned}
\mathbf{M}_{(\mathbf{y},\mathbf{z})} = \quad & \frac{\partial_I \mathbf{v}_{0C}^T}{\partial \mathbf{z}} \, m_C \, \frac{\partial_I \mathbf{v}_{0C}}{\partial \mathbf{z}} + \frac{\partial_C \boldsymbol{\omega}_{0C}^T}{\partial \mathbf{z}} \, {}_C\mathbf{T}_{SC} \, \frac{\partial_C \boldsymbol{\omega}_{0C}}{\partial \mathbf{z}} \\
& + \frac{\partial_I \mathbf{v}_{0S}^T}{\partial \mathbf{z}} \, m_S \, \frac{\partial_I \mathbf{v}_{0S}}{\partial \mathbf{z}} + \frac{\partial_S \boldsymbol{\omega}_{0S}^T}{\partial \mathbf{z}} \, {}_S\mathbf{T}_{SS} \, \frac{\partial_S \boldsymbol{\omega}_{0S}}{\partial \mathbf{z}} \\
& + \frac{\partial_I \mathbf{v}_{0G}^T}{\partial \mathbf{z}} \, m_G \, \frac{\partial_I \mathbf{v}_{0G}}{\partial \mathbf{z}} + \frac{\partial_G \boldsymbol{\omega}_{0G}^T}{\partial \mathbf{z}} \, {}_G\mathbf{T}_{SG} \, \frac{\partial_G \boldsymbol{\omega}_{0G}}{\partial \mathbf{z}} \\
& + \frac{\partial_I \mathbf{v}_{0L}^T}{\partial \mathbf{z}} \, m_L \, \frac{\partial_I \mathbf{v}_{0L}}{\partial \mathbf{z}} + \frac{\partial_L \boldsymbol{\omega}_{0L}^T}{\partial \mathbf{z}} \, {}_L\mathbf{T}_{SL} \, \frac{\partial_L \boldsymbol{\omega}_{0L}}{\partial \mathbf{z}} \\
& + \frac{\partial_I \mathbf{v}_{0H}^T}{\partial \mathbf{z}} \, m_H \, \frac{\partial_I \mathbf{v}_{0H}}{\partial \mathbf{z}} + \frac{\partial_H \boldsymbol{\omega}_{0H}^T}{\partial \mathbf{z}} \, {}_H\mathbf{T}_{SH} \, \frac{\partial_H \boldsymbol{\omega}_{0H}}{\partial \mathbf{z}} \\
& + \frac{\partial_I \mathbf{v}_{0V}^T}{\partial \mathbf{z}} \, m_V \, \frac{\partial_I \mathbf{v}_{0V}}{\partial \mathbf{z}} + \frac{\partial_V \boldsymbol{\omega}_{0V}^T}{\partial \mathbf{z}} \, {}_V\mathbf{T}_{SV} \, \frac{\partial_V \boldsymbol{\omega}_{0V}}{\partial \mathbf{z}} \, ,
\end{aligned} \tag{4.30}$$

where m_C, m_S, m_G, m_L, m_H and m_V are the masses of the six bodies and ${}_C\mathbf{T}_{SC}$, ${}_S\mathbf{T}_{SS}$, ${}_G\mathbf{T}_{SG}$, ${}_L\mathbf{T}_{SL}$, ${}_H\mathbf{T}_{SH}$ and ${}_V\mathbf{T}_{SV}$ are the inertia tensors represented in the respective body-fixed axis system in relation to the respective centers of mass. The generalized mass matrix is symbolically derived with the MATLAB SYMBOLIC TOOLBOX and is represented for further use as function of the generalized coordinates and velocities. The 11 × 11 matrix is almost full, and can be written as

$$\mathbf{M}_{(\mathbf{y},\mathbf{z})} = \begin{bmatrix} m_{All} & 0 & 0 & \cdots \\ 0 & m_{All} & 0 & \cdots \\ 0 & 0 & m_{All} & \cdots \\ \vdots & \vdots & \vdots & \ddots \end{bmatrix} , \tag{4.31}$$

where m_{All} is the sum of the masses of the six bodies. Just the first part, related to the position of the racebike reference point is a 3×3 unity matrix with magnitude m_{All}. The other elements are composed of complicated multiplications of generalized coordinates and angular functions of them.

4.5.7 Generalized Forces and Moments

With reference to Eq. 3.21, the generalized forces can be written as the sum of the following three components

$$\mathbf{q}_{(\mathbf{y},\mathbf{z})} = \mathbf{q}_{act(\mathbf{y},\mathbf{z})} + \mathbf{q}_{app(\mathbf{y},\mathbf{z})} + \mathbf{q}_{gyro(\mathbf{y},\mathbf{z})} \, , \tag{4.32}$$

where $\mathbf{q}_{act}$ are the generalized active forces, $\mathbf{q}_{app}$ are the generalized apparent forces and $\mathbf{q}_{gyro}$ are the generalized gyroscopic forces.

Generalized Active Forces The generalized active forces are denoted as

$$\mathbf{q}_{act(\mathbf{y},\mathbf{z})} = \sum_b \left\{ \mathbf{J}^T_{vz\,b(\mathbf{y},\mathbf{z})}\, {}_I\mathbf{F}^{(a)}_b + \mathbf{J}^T_{\omega z\,b(\mathbf{y},\mathbf{z})}\, {}_b\mathbf{M}^{(a)}_{Sb} \right\}, \tag{4.33}$$

with the Jacobi matrices $J_{vz\,b(\mathbf{y},\mathbf{z})}$ and $J_{\omega z\,b(\mathbf{y},\mathbf{z})}$ and the active forces and moments ${}_I\mathbf{F}^{(a)}_b$ and ${}_b\mathbf{M}^{(a)}_{Sb}$ for the six bodies $b = C, S, G, L, H, V$. The **external active forces and moments** of the racebike model are:

- The weight forces of all single bodies acting in the respective center of gravity positions.
- The tire forces and moments from Fig. 3.11 acting in the wheel contact points of the front and the rear wheel ($b = V, H$).
- The aerodynamic forces and moments of the whole racebike which are assigned to the chassis ($b = C$) in the present model.

The following **active forces and moments act inside** the racebike model:

- The front fork force acts between the upper and lower front assembly ($b = L, G$). The spring force is a function of the front suspension stroke s_G. The damping force is a linear function of the front suspension travel rate $\dot{s}_G$.
- The rear suspension moment is acting between the chassis ($b = C$) and the swingarm ($b = S$). The rear suspension spring moment is a function of the swing arm angle θ_S. The rear suspension damping moment is a function of the swing arm angle velocity $\dot{\theta}_S$.
- The racebike has a rear wheel drive. The drive torque of the engine is acting in the rear wheel center $H1$ around the y-axis of the swingarm ${}_Se_y$.
- The engine supporting torque is acting in the chassis fixed point $C4$ around the y-axis of the chassis ${}_Ce_y$. The influence of the chain is not considered in the present work.
- The racebike has disc brakes at both wheels. The braking torques are acting in the front and rear wheel centers $V1$ and $H1$ around the corresponding y-axis ${}_Se_y$ and ${}_Ge_y$.
- The steering forces of the rider are applied to the handlebars. The forces on the the handlebars are acting as steering moment around the steering axis ${}_Le_z$.
- The steering damper moment is acting in the steering head around the steering axis ${}_Le_z$. The damping moment is a function of the steering angle velocity $\dot{\delta}_L$.

Generalized Apparent Forces Apparent forces like centrifugal and Coriolis forces include the effects of an accelerating frame of reference in the equation of motion. In a generalized way they are defined in accordance with Eqs. 3.21 and 3.22 as

$$\mathbf{q}_{app(\mathbf{y},\mathbf{z})} = \sum_b \left\{ -\,\mathbf{J}^T_{vz\,b(\mathbf{y},\mathbf{z})}\, m_b\, {}_I\dot{\mathbf{v}}^S_{0b} - \mathbf{J}^T_{\omega z\,b(\mathbf{y},\mathbf{z})}\; {}_b\mathbf{T}_{Sb}\; {}_b\dot{\boldsymbol{\omega}}^S_{0b} \right\}, \tag{4.34}$$

with the Jacobi matrices $J_{vz\,b(\mathbf{y},\mathbf{z})}$ and $J_{\omega z\,b(\mathbf{y},\mathbf{z})}$ and the mass and inertia properties m_b and ${}_b\mathbf{T}_{Sb}$ for the six bodies $b = C, S, G, L, H, V$. ${}_I\dot{\mathbf{v}}^S_{0b}$ and ${}_b\dot{\boldsymbol{\omega}}^S_{0b}$ denote the apparent accelerations.

Generalized Gyroscopic Forces The generalized gyroscopic forces are defined by the angular velocity vectors in the body frame of reference and by the inertia tensors of the single bodies, denoted as

$$\mathbf{q}_{gyro(\mathbf{y},\mathbf{z})} = \sum_b \left\{ \mathbf{J}^T_{\omega z\,b(\mathbf{y},\mathbf{z})} \left[-{}_b\boldsymbol{\omega}_{0b} \times {}_b\mathbf{T}_{Sb}\, {}_b\boldsymbol{\omega}_{0b} \right] \right\}, \tag{4.35}$$

for the six bodies $b = C, S, G, L, H, V$. Simply explained, gyroscopic forces are a result of any spinning masses that tends to keep the spinning axis in place. It acts like additional inertia, if the orientation of the axis wants to be changed. For the racebike this applies especially for the engine crankshaft (not considered in the model) and the rotating wheels.

4.5.8 Generalized Inertial Forces

With reference to Eq. 3.19, the term mass times acceleration denotes the generalized inertial forces, just that

$$\mathbf{q}_{inert(\mathbf{y},\mathbf{z})} = \mathbf{M}_{(\mathbf{y})}\dot{\mathbf{z}}\,, \tag{4.36}$$

with the generalized mass matrix $\mathbf{M}_{(\mathbf{y})}$ and the generalized acceleration vector $\dot{\mathbf{z}}$.

4.6 A new Approach for the Assessment of Aerodynamic Characteristics from Racetrack Measurement Data

The equation of motion derived in section 4.5 covers a racebike model with rigid bodies and a rigidly attached rider. Real riding situations of a racebike on a racetrack are strongly driven by rider movements on the racebike.

For a better understanding, the influence is explained by means of a typical riding situation. A good example is a *hanging-off* riding situation (see Fig. 2.8 b, c and f) – the rider is leaning his body into the curve to move the center of gravity in lateral direction into the center of the curve.

The rider body in *hanging-off* or any other riding position on the racebike has a great influence on all elements of the equation of motion.

- The generalized active forces are changed by a different center of gravity position of the cassis-rider body ($b = C$).
- The generalized active forces are influenced by changing aerodynamic forces and moments acting on the rider in *hanging-off* position.
- The generalized apparent forces are affected by varying Jacobi matrices as a result of a changed center of gravity position.
- The generalized gyroscopic forces are influenced by a changing Jacobi matrix and a changed moment of inertia of the chassis-rider body ($b = C$).
- The contact forces between the rider and the chassis on the seat, footrests and handlebars are active forces that act on the chassis body.

The single influences are difficult or impossible to describe for a rider-racebike system on a racetrack.

4.6.1 Aerodynamic Racebike Model – The AIM Approach

The approach presented here combines all influences which are difficult or impossible to describe in one model. The approach is called the *AIM* (=acronym for **A**erodynamic, **I**nertia and **M**ass) approach. The *AIM* model process, shown in Fig. 4.4 combines:

- the aerodynamic forces and moments of the racebike-rider system,
- the inertia changes due to rider movements and
- the center of gravity change (mass) due to rider movements.

The *AIM* approach is implemented by introducing a new term $\mathbf{q}_{aim(\mathbf{y},\mathbf{z})}$ into the equation of motion with reference to Eq. 3.19, just that

$$\underbrace{\mathbf{M}_{(\mathbf{y})}\dot{\mathbf{z}} = \mathbf{q}_{act(\mathbf{y},\mathbf{z})} + \mathbf{q}_{app(\mathbf{y},\mathbf{z})} + \mathbf{q}_{gyro(\mathbf{y},\mathbf{z})}}_{\text{physical racebike model with rigidly attached rider}} + \underbrace{\mathbf{q}_{aim(\mathbf{y},\mathbf{z})}}_{\text{New}} . \tag{4.37}$$

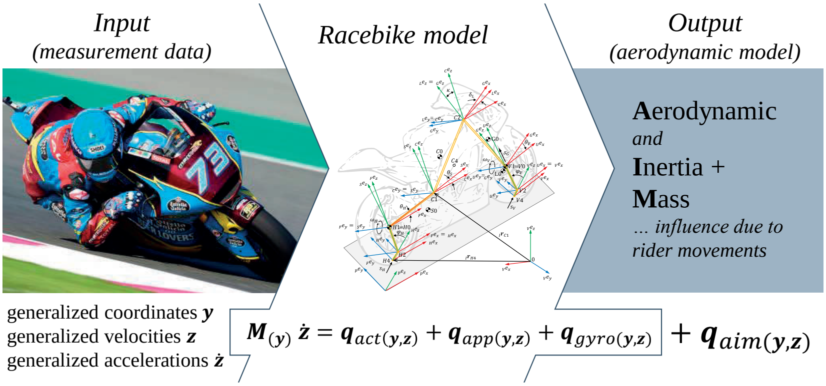

Figure 4.4: A new approach for the assessment of aerodynamic characteristics from racetrack measurement data including inertia and mass property changes due to rider movements on the racebike – The AIM approach (by Christoph Feichtinger – own work).

Transformed according to $\mathbf{q}_{aim(\mathbf{y},\mathbf{z})}$, the equation of motion can be written as

$$\mathbf{q}_{aim(\mathbf{y},\mathbf{z})} = \mathbf{M}_{(\mathbf{y})}\dot{\mathbf{z}} - \mathbf{q}_{act(\mathbf{y},\mathbf{z})} - \mathbf{q}_{app(\mathbf{y},\mathbf{z})} - \mathbf{q}_{gyro(\mathbf{y},\mathbf{z})}\,. \tag{4.38}$$

The terms on the right side of the equation can be calculated from the vectors of the generalized coordinates, velocities, and accelerations ($\mathbf{y}$, $\mathbf{z}$ and $\dot{\mathbf{z}}$). These quantities are known from measurement data of the racebike. The available measurement data and the data preparation are described in chapter 5.

4.6.2 AIM Forces and Moments

The aim forces and moments are active forces in the context of Jourdains principle. With reference to Eq. 4.33, the generalized AIM forces can be written as

$$\mathbf{q}_{aim(\mathbf{y},\mathbf{z})} = \sum_{b=1}^{6}\left\{\mathbf{J}^{T}_{vz\,b(\mathbf{y},\mathbf{z})}\;{}_{I}\mathbf{F}^{(a)}_{aim} + \mathbf{J}^{T}_{\omega z\,b(\mathbf{y},\mathbf{z})}\;{}_{b}\mathbf{M}^{(a)}_{aim}\right\}. \tag{4.39}$$

The AIM forces and moments are exclusively assigned to the chassis body (C) acting in and around the racebike reference point $C1$ in the chassis coordinate system (C). Therefore, Eq. 4.39 simplifies to one body, just that

$$\mathbf{q}_{aim(\mathbf{y},\mathbf{z})} = \mathbf{J}^{T}_{vz\,C(\mathbf{y},\mathbf{z})}\;{}_{I}\mathbf{F}^{(a)}_{aim} + \mathbf{J}^{T}_{\omega z\,C(\mathbf{y},\mathbf{z})}\;{}_{C}\mathbf{M}^{(a)}_{aim}\,. \tag{4.40}$$

With the assumption of assigning the aerodynamic forces and moments to the chassis, the Jacobi matrices for the translational and angular speed derivative after the generalized velocity vector simplify.

The Jacobi matrix for the translational velocity derivative, according to the center of gravity velocity vector (Eq. 4.22), reads

$$\mathbf{J}^T_{vz\,C(\mathbf{y},\mathbf{z})} = \begin{bmatrix} 1 & 0 & 0 & a_{14} & a_{15} & a_{16} & 0 & 0 & 0 & 0 & 0 \\ 0 & 1 & 0 & a_{24} & a_{25} & a_{26} & 0 & 0 & 0 & 0 & 0 \\ 0 & 0 & 1 & a_{34} & a_{35} & a_{36} & 0 & 0 & 0 & 0 & 0 \end{bmatrix}, \tag{4.41}$$

where the factors $a_{ij}\,(i,j = 1,2,3)$ are placeholders for the complicated mathematical expressions.

In the same way, the Jacobi matrix for the angular velocity derivative with respect to Eq. 4.23 is denoted as

$$\mathbf{J}^T_{\omega z\,C(\mathbf{y},\mathbf{z})} = \begin{bmatrix} 0 & 0 & 0 & 1 & 0 & 0 & 0 & 0 & 0 & 0 & 0 \\ 0 & 0 & 0 & 0 & 1 & 0 & 0 & 0 & 0 & 0 & 0 \\ 0 & 0 & 0 & 0 & 0 & 1 & 0 & 0 & 0 & 0 & 0 \end{bmatrix}. \tag{4.42}$$

The AIM force and moment vector in the chassis axis system are shown in Fig. 4.5. The AIM force vector in the chassis axis system is denoted as

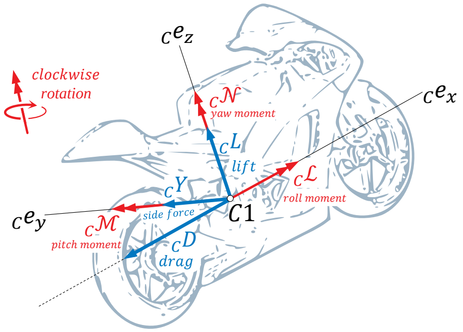

Figure 4.5: Aerodynamic/AIM forces and moments acting in the racebike reference point $C1$ in the chassis axis system (by Christoph Feichtinger – own work).

$${}_C\mathbf{F}_{aim} = \begin{Bmatrix} {}_CD \\ {}_CY \\ {}_CL \end{Bmatrix}. \tag{4.43}$$

The AIM force vector is transformed into the inertial frame of reference, using the rotation matrix $\mathbf{A}_{IC}$, just that

$$
{}_I\mathbf{F}_{aim} = \mathbf{A}_{IC}\,{}_C\mathbf{F}_{aim}\,. \tag{4.44}
$$

The AIM moment vector acting around the racebike reference point $C1$ in the chassis axis system reads

$$
{}_C\mathbf{M}^{(C1)}_{aim} = \begin{Bmatrix} {}_C\mathcal{L} \\ {}_C\mathcal{M} \\ {}_C\mathcal{N} \end{Bmatrix}\,. \tag{4.45}
$$

The AIM moment vector acting in the chassis center of gravity $C0$ in the chassis axis system is given by

$$
{}_C\mathbf{M}^{(C0)}_{aim} = {}_C\mathbf{M}^{(C1)}_{aim} + {}_C\mathbf{r}_{C0C1} \times {}_C\mathbf{F}_{aim}\,. \tag{4.46}
$$

The generalized force vector has 11 elements according to the elements of the generalized velocity vector. Inserting the Jacobi matrices and the forces and moments in Eq. 4.40, the generalized aerodynamic forces in component notation reads

$$
\begin{Bmatrix} q_1 \\ q_2 \\ q_3 \\ q_4 \\ q_5 \\ q_6 \\ q_7 \\ q_8 \\ q_9 \\ q_{10} \\ q_{11} \end{Bmatrix} = \begin{Bmatrix} {}_ID \\ {}_IY \\ {}_IL \\ {}_C\mathcal{L} + a_{14}\,{}_ID + a_{24}\,{}_IY + a_{34}\,{}_IL + {}_IL\,y_{C1C0} + {}_IY\,z_{C1C0} \\ {}_C\mathcal{M} + a_{15}\,{}_ID + a_{25}\,{}_IY + a_{35}\,{}_IL - {}_IL\,x_{C1C0} + {}_ID\,z_{C1C0} \\ {}_C\mathcal{N} + a_{16}\,{}_ID + a_{26}\,{}_IY + a_{36}\,{}_IL + {}_IY\,x_{C1C0} - {}_ID\,y_{C1C0} \\ 0 \\ 0 \\ 0 \\ 0 \\ 0 \end{Bmatrix}\,. \tag{4.47}
$$

Due to the zero elements of the Jacobi matrices (Eqs. 4.42 and 4.42), the generalized forces with index 7 to 11 are zero. Using the MATLAB SYMBOLIC TOOLBOX, the AIM force and moment vectors can be calculated. The AIM force vector results in

$$
\begin{Bmatrix} {}_ID \\ {}_IY \\ {}_IL \end{Bmatrix} = \begin{Bmatrix} q_1 \\ q_2 \\ q_3 \end{Bmatrix}\,. \tag{4.48}
$$

The AIM moment vector becomes

$$
\begin{Bmatrix} {}_C\mathcal{L} \\ {}_C\mathcal{M} \\ {}_C\mathcal{N} \end{Bmatrix} = \begin{Bmatrix} q_4 - a_{14}\,q_1 - a_{24}\,q_2 - a_{34}\,q_3 - y_{C1C0}\,q_3 + z_{C1C0}\,q_2 \\ q_5 - a_{15}\,q_1 - a_{25}\,q_2 - a_{35}\,q_3 + x_{C1C0}\,q_3 - z_{C1C0}\,q_1 \\ q_6 - a_{16}\,q_1 - a_{26}\,q_2 - a_{36}\,q_3 - x_{C1C0}\,q_2 + y_{C1C0}\,q_1 \end{Bmatrix}\,. \tag{4.49}
$$

With this the AIM characteristics can be calculated as function of the generalized coordinate, velocity, and acceleration vectors, $\mathbf{y}$, $\mathbf{z}$ and $\dot{\mathbf{z}}$.

4.6.3 Dimensionless Coefficients

Aerodynamic characteristics are mainly defined, described, or provided as dimensionless force and moment coefficients. They are derived from the dimensional forces and moments by dividing them through the dynamic pressure $q_\infty = q_{dyn}$, a reference area A_x and a reference length l_{ref}, denoted as

$$\begin{aligned} c_D &= \frac{D}{q_\infty\, A_x} & \qquad c_\mathcal{L} &= \frac{\mathcal{L}}{q_\infty\, A_x\, l_{ref}} \\ c_Y &= \frac{Y}{q_\infty\, A_x} & \qquad c_\mathcal{M} &= \frac{\mathcal{M}}{q_\infty\, A_x\, l_{ref}} \\ c_L &= \frac{L}{q_\infty\, A_x} & \qquad c_\mathcal{N} &= \frac{\mathcal{N}}{q_\infty\, A_x\, l_{ref}}\,. \end{aligned} \tag{4.50}$$

All the reference quantities are arbitrary. The traditional choice for the reference area A_x is the projected area in longitudinal direction. The projection area of a racebike depends strongly on the actual position of the rider. The projected area has its minimum when the rider is in top speed position, completely fitted to the racebike. For *hanging-off* riding situations, where the rider is leaning out of the racebike or in braking situations, where the rider is in upright position, the projected area can increase by up to 50%. As the real projected area cannot be measured directly on the racetrack the projected area is hereinafter taken to be $A_x = 1\,m^2$. Therefore, the dimensionless force and moment coefficients are equal to the force and moment areas. The reference length l_{ref} for the moment coefficients is the wheelbase of the racebike, which varies depending on the riding situation.

Chapter 5

From Measurement to Model

5.1 Measurement Environment and Data Acquisition

The motorcycle manufacturer *KALEX* has provided data of one rider from the Moto2 race in Aragon 2019 for the calculation of aerodynamic characteristics using the new approach presented here. The data were handed over in tabular form for every single lap with a sampling rate of $100\,Hz$. The following Tab. 5.2 shows the measurement channels with the descriptive channel names, a short description and the corresponding channel units. The data were recorded during an official race event. The electronics, the sensors and the tires are limited in Moto2. They are supplied by FIM-sanctioned producers Magneti-Marelli and Dunlop.

Table 5.1: Moto2 measurement channels with description, unit and measurement ranges

channel	**description**	**unit**	**min**	**max**
Time	race time	s	0	2431
NTime	lap time	s	0	159.14
NLap	lap counter	#	1	21
vWhF	front circumf. wheel speed	km/h	0	281.9
vWhR	rear circumf. wheel speed	km/h	0	299.5
aLean	lean angle	$^\circ$	-61.88	56.72
cWheelFn	angular front wheel speed	$1/s$	0	40.93
cWheelRn	angular rear wheel speed	$1/s$	0	40.64
xSuspF	front suspension stroke	mm	0	129
xSuspR	rear suspension stroke	mm	0	32
TPMS_FrontPres	tire pressure front tire	bar	2.23	2.48

...to be continued on next page

Moto2 measurement channels with description, unit and measurement ranges - continuation

channel	**description**	**unit**	**min**	**max**
TPMS_RearPres	tire pressure rear tire	*bar*	1.29	1.51
TEng	engine cooling temperature	$°C$	72	89
nEngine720	engine speed	U/min	2861	14840
MRiderTrq	engine torque	Nm	-27.1	81.9
rThrottle1	throttle position	%	-1.5	102
pBrakeF	brake pressure front	*bar*	-0.48	16.36
pBrakeR	brake pressure rear	*bar*	-0.62	33.81
aSteer	steering angle	°	-10.45	14.97
X2_Pub_LastID	SectionID	#	20	34

The time and lap channels are self-explanatory. The wheel speeds *vWhF* and *vWhR* of the front and rear wheel are calculated quantities from the angular wheel speeds *cWheelFn* and *cWheelRn* of the front and rear wheel. The lean angle *aLean* is derived from the inertial measurement unit (IMU) and is calculated in real time in the electronic control unit (ECU). The algorithm to calculate the lean angle in the ECU is not public available. The IMU is mounted fixed to the chassis, $100\,mm$ above the pivot point $C1$ in z-direction.

The suspension travel strokes *xSuspF* and *xSuspR* of the front fork and the rear shock are directly measured by fork and shock mounted linear potentiometers. The tire pressures *TPMS_FrontPres* and *TPMS_RearPres* are measured directly with rim mounted pressure sensors. The engine cooling temperature *TEng* is measured at the inlet of the radiator, where the highest temperature is found. The engine speed *nEngine720* is measured on the crankshaft of the engine. The engine torque *MRiderTrq* is calculated in real-time in the ECU depending on:

- the throttle position *rThrottle1*,
- the engine speed *nEngine720*,
- the barometric pressure in the airbox and much more. These influences are used for internal purposes by exclusive engine supplier Triumph [60] only and cannot be viewed by the race teams.

The brake pressures *pBrakeF* and *pBrakeR* are measured with pressure transducers at the brake cylinders. The front brake cylinder is mounted on the right handlebar lever. The rear brake cylinder is mounted on the right footrest assembly. The steering angle *aSteer* is calculated from the linear potentiometer mounted on the steering damper.

Normalized Measurement Quantities The measurement quantities are hereinafter shown as dimensionless, normalized quantities, derived using the following computation

$$\hat{q}_{meas} = \frac{q_{meas}}{max(|q_{meas}|)} , \tag{5.1}$$

where q_{meas} denotes any quantity. Therefore, quantities like the bike speed ranges from 0 to $+1$, while measured quantities with negative components range from -1 to $+1$.

Leading Measurement Quantities Racebike The lean angle and the speed of the racebike are the leading measurement quantities for the analysis and segmentation of the measurement data (see section 2.3). With reference to Tab. 5.2,

- the lean angle φ_{bike} is the measurement channel $aLean$,
- the racebike reference speed v_{bike} is the front circumferential wheel speed $vWhF$.

Moto2 Race Aragon 2019 The Aragon racetrack map is shown in Fig. 5.1. The course is driven counterclockwise. The map shows numbered points from 1 to 20. The uneven numbers show the points where a Moto2 racebike starts to accelerate. The even numbers mark the points where a Moto2 racebike starts to brake. The data recording on the racebike is started at the starting grid short before the riders start into the warm-up lap. The warm-up lap is not included

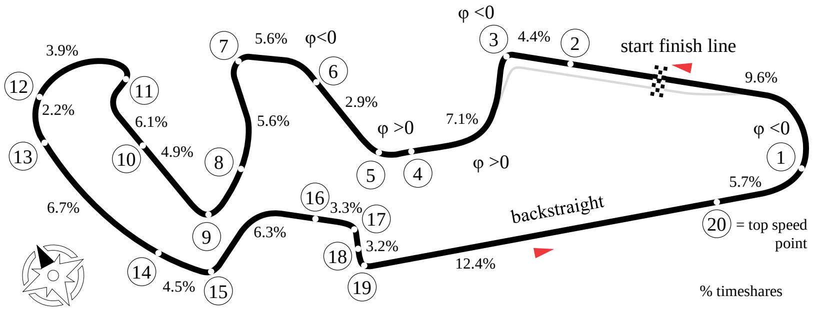

Figure 5.1: Aragon racetrack acceleration (uneven numbers) and braking points (even numbers) for a Moto2 racebike and the time shares of the single longitudinal dynamics' segments.

in the measurements. The normalized racebike speed $\hat{v}_{bike}$ is shown in Fig. 5.2 against the normalized race time $\hat{t}_{race}$. The racebike speed is the ground speed of the racebike with respect to the racetrack. The first part shows the racebike standing in the starting grid at zero speed $\hat{v}_{bike} = 0$. The remaining recordings show the 21 laps of the complete Moto2 race in Aragon 2019. With a track length of $5.078\,km$ the overall race distance was $106.6\,km$. The Moto2 race 2019 was won by Brad Binder with a racetime of $39'45.177$, which is an average speed of 160.9 km/h.

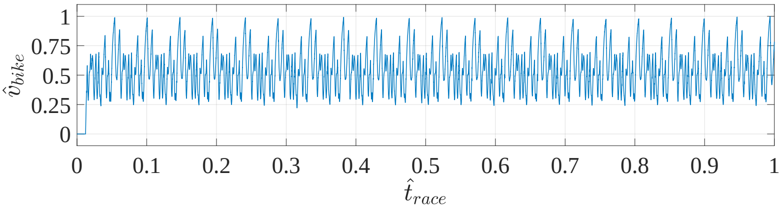

Figure 5.2: Normalized racebike speed $\hat{v}_{bike}$ *raw data readings against the normalized race lap time* $\hat{t}_{race}$*.*

Measurement Data Readings Additional measurement raw data readings are presented in Fig. 5.3 for the time range before the start and the first race lap. The following, normalized raw measurement data are shown with reference to the channels from Tab. 5.2 in brackets:

- the steering angle $\hat{\delta}_{steer}$ ($aSteer$),
- the front and rear suspension strokes $\hat{x}_{suspF}$ and $\hat{x}_{suspR}$ ($xSuspF$, $xSuspR$),
- the engine speed $\hat{n}_{eng}$ ($nEngine720$),
- the engine torque $\hat{M}_{eng}$ ($MRiderTrq$) and
- the front and rear brake pressures $\hat{p}_{brakeF}$ and $\hat{p}_{brakeR}$ ($pBrakeF$, $pBrakeR$).

The steep rise of the engine torque $\hat{M}_{eng}$ marks the race start. The recordings show the highly dynamic movements of the racebike on the racetrack. There is nearly no steady section in any measured quantity visible. If then perhaps on the long back-straight ($\hat{t}_{race} \sim 0.05$) before reaching the top speed of the racetrack. In this area the lean angle tends to be zero in the last part, the rear suspension strokes settle down to a near constant value, while the front suspension stroke slightly increases. This can be an indication for a kind of downforce generation at higher

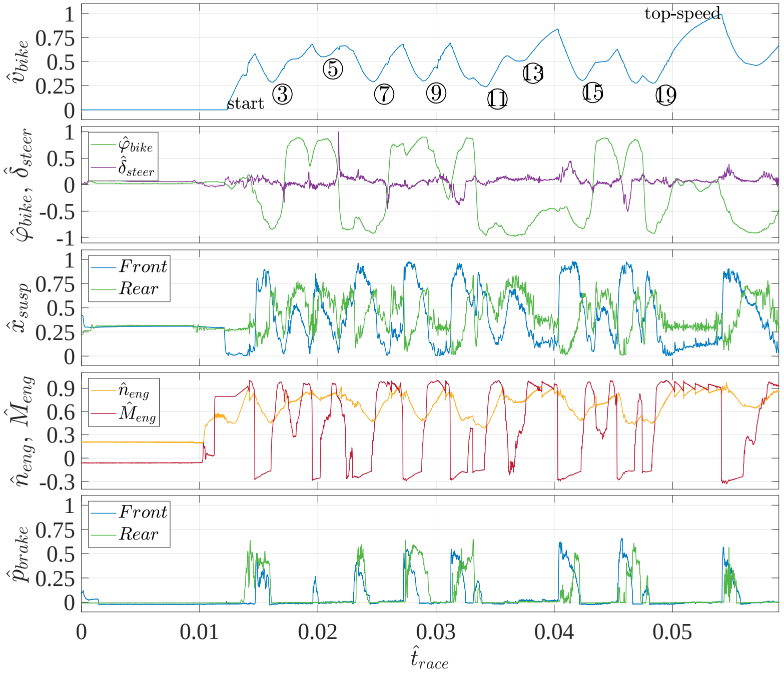

Figure 5.3: Measurement raw data readings with normalized quantities plotted against the normalized race time $\hat{t}_{race}$, showing the time before the start and the first full race lap.

speeds. For a more precise analysis the raw measurement data are segmented and classified in the next sections.

5.2 Data Analysis and Preparation

The aim of the data analysis is to find a meaning in the measurement raw data readings so that the knowledge can be used to make decisions. Therefore, the raw data readings of the whole race are sorted in a first step by the single laps. Afterwards the lap sorted readings are segmented according to the longitudinal acceleration and deceleration of the racebike.

New Lap Counter The original lap length starting point at the start finish line is not ideal for the further segmentation according to the acceleration signal, as the start finish line is traditionally inside an acceleration segment. The top-speed peaks per lap were used to split the complete race data into the single laps. In the case of the Aragon racetrack, the top speed is reached on the backstraight before the last corner, shown in Fig. 5.1. Fig. 5.4 shows the normalized racebike speed $\hat{v}_{bike}$ raw data readings against the normalized lap time $\hat{t}_{lap}$ of the second lap of one rider during real race traffic conditions.

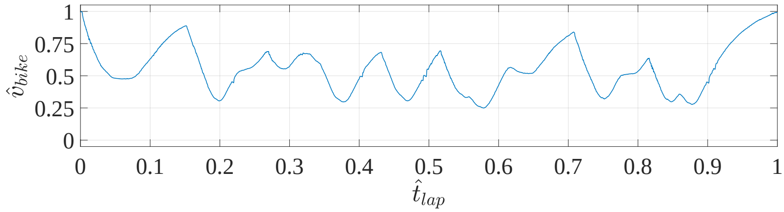

Figure 5.4: Normalized racebike speed $\hat{v}_{bike}$ raw data readings against the normalized lap time $\hat{t}_{lap}$ of the second lap.

Longitudinal Dynamics Segmentation For every single lap, the normalized lap is further subdivided into acceleration and deceleration segments. This is done by an identification of the local speed minima and maxima. For the present Moto2 race data 10 local bike speed maxima and 10 local bike speed minima were identified, see Fig. 5.5. Therefore, the 20 extrema split each lap into 20 acceleration or deceleration segments with different segment times. The single segments for the different laps, slightly differ in terms of segment time and segment length. The normalized times per segment were used to average the raw measurement recordings over all race laps. Fig. 5.6 shows the procedure of filtering and averaging for the segment between the points 19 to 20 for all race laps.

- The left subfigure in Fig. 5.6 shows the normalized racebike speed $\hat{v}_{bike}$ raw data readings against the raw normalized segment time $\hat{t}_{seg}$.
- The middle subfigure shows the normalized racebike speed $\hat{v}_{bike}$ raw data readings against the new, normalized segment time $\hat{t}_{seg}$. Both subfigures show a degressive deflection of the speed signal.
- The right subfigure shows the normalized, cleaned up speed signal $\hat{v}_{bike-cleaned\ up}$.

The deflection in the left and middle subfigures is linked to the front wheel coming off the ground (a so called *Wheelie* or wheel-stand) due to too much torque being

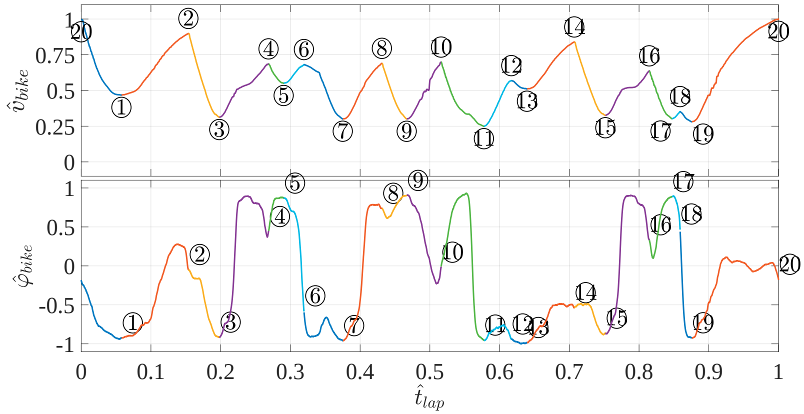

Figure 5.5: Normalized bike speed $\hat{v}_{bike}$ and normalized lean angle $\hat{\varphi}_{bike}$ plotted against the normalized lap time $\hat{t}_{lap}$. This is the representative lap for the physical model derivation.

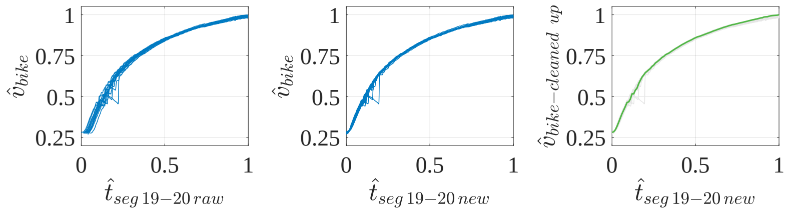

Figure 5.6: The three subfigures show the segment between the points 19 *to* 20 *for all race laps. The left subfigure shows the normalized racebike speed $\hat{v}_{bike}$ raw data readings against the raw normalized segment time $\hat{t}_{seg}$. The middle subfigure shows the normalized racebike speed $\hat{v}_{bike}$ raw data readings against the new, normalized segment time $\hat{t}_{seg}$. The right subfigure shows the normalized, cleaned up speed signal $\hat{v}_{bike-cleaned\ up}$.*

applied to the rear wheel, or due to a rider motion relative to the racebike – We remember that the bike speed is the front wheel circumferential speed. The laps with *Wheelie* are excluded for the representative race laps.

The single averaged segments were afterwards combined to an averaged lap for the whole race. Fig. 5.5 shows the normalized bike speed $\hat{v}_{bike}$ and the normalized lean angle $\hat{\varphi}_{bike}$ plotted against the normalized lap time $\hat{t}_{lap}$.

This averaging procedure was repeated for all raw measurement recordings from Tab. 5.2. The lap and segment averaged measurement channels are stored in a MATLAB table with a sampling rate of 100 Hz. The data table also includes the time and a path signal for further time or path-based use of the race data. The path signal was calculated by integrating the speed signal with time. The raw measurement channels are available in a generic way denoted as

$$q_{meas} = q_{meas(t,s)} \; , \tag{5.2}$$

with t as the time signal and s as the path length. The lap and segment averaged race data is the basis for the analysis of the racebike dynamics.

5.3 Model Data Preparation

The lap averaged measurement data from chapter 5.2 are used to prepare the generalized coordinates, velocities and accelerations. This is the input for the AIM approach, presented in chapter 4.6. Fig. 5.7 shows the scheme for processing the lap averaged measurement data into input data for the AIM approach. The single steps are further explained in the following paragraphs.

The Racebike Position on the Racetrack The racebike position on the racetrack is given by the three-dimensional position vector of the rear wheel road-tire contact point, denoted as

$$_{I}\mathbf{r}_{H4(t)} = \left\{ _{I}x_{H4} \quad _{I}y_{H4} \quad _{I}z_{H4} \right\}^{T} \; . \tag{5.3}$$

The x- and y-position of the racebike in the inertial frame of reference is taken from GPS measurements of the racebike. The altitude information (z-coordinate in the inertial frame of reference) and the orientation of the racetrack surface patch is taken from OpenStreetMap® [47]. The orientation is denoted by the transformation matrix $\mathbf{A}_{Ip(t)}$. The three-dimensional trace of the vector is shown in Fig. 5.8 with the braking and accelerating points.

The Relative Racebike Position on the Racetrack The relative racebike position on the racetrack is mainly defined by the lean angle. The relative position vector $_{C}\mathbf{r}_{H4C1(t)}$ contains a complicated calculation of the local tire angles θ_H and θ_V. The angles are calculated using the MATLAB SYMBOLIC TOOLBOX [41]. With this, the relative position vector can be calculated as function of the raw measurement readings, namely

- the lean angle φ_{bike},

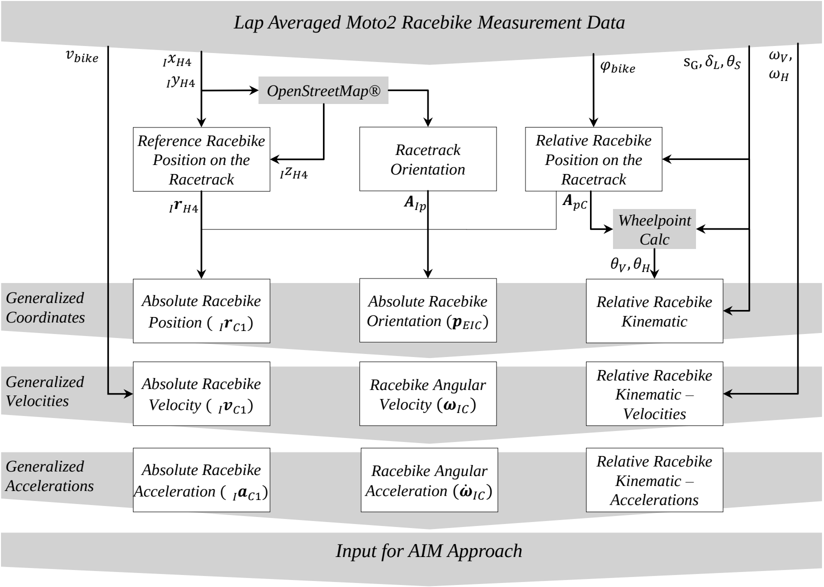

Figure 5.7: Model data preparation – From Moto2 racebike measurement data to generalized coordinates, velocities, and accelerations.

- the front suspension stroke $s_G = xSuspF$,
- the steering angle $\delta_L = aSteer$ and
- the rear suspension stroke $\theta_S \sim xSuspR$. The rear suspension stroke is converted into a angular signal using a kinematic relationship given by *KALEX*.

The transformation matrix $\mathbf{A}_{pC(t)}$ between the road tire contact patch p and the chassis axis system C, is calculated in the same way as a symbolic representation.

Fig. 5.9 shows the normalized, relative racebike quantities and the relative velocities for the representative race lap. It shows that the front and rear suspension is permanently working, except for a small settling section at the end of the lap. The steering angle signal $\hat{\delta}_L$ shows the permanent rider input during a race lap.

The Absolute Racebike Position on the Racetrack The orientation of the racetrack patch together with the relative rotation between the racetrack patch and

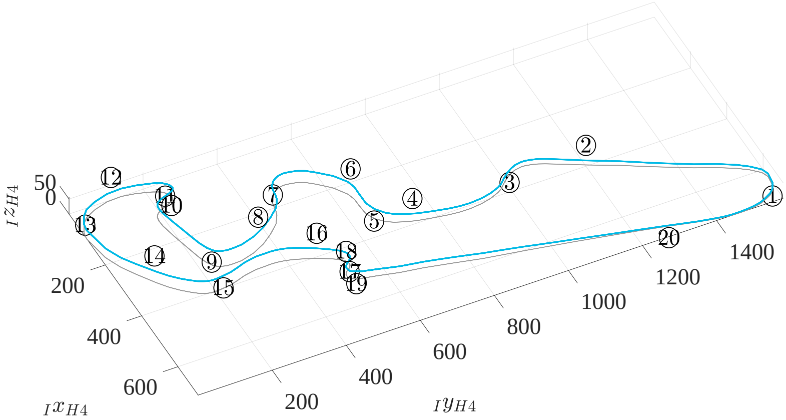

Figure 5.8: Rear wheel road-tire contact point trace of the representative lap. The three-dimensional coordinates are given in m.

the chassis axis systems delivers the transformation matrix between the inertial axis system and the chassis axis system as follows

$$\mathbf{A}_{IC(t)} = \mathbf{A}_{Ip(t)}\ \mathbf{A}_{pC(t)}\,. \tag{5.4}$$

The transformation matrix $\mathbf{A}_{IC(t)}$ is converted into a quaternion representation for the handover to the generalized coordinate vector. The Euler parameters in vector notation are denoted as

$$\mathbf{p}^T_{EIC(t)} = \left\{e_{0IC} \quad e_{1IC} \quad e_{2IC} \quad e_{3IC}\right\}^T = rotm2quat(\mathbf{A}_{IC(t)})\,. \tag{5.5}$$

The position vector of the racebike reference point $C1$ is given as

$$_I\mathbf{r}_{C1(t)} = \left\{x_C \quad y_C \quad z_C\right\}^T = {_I\mathbf{r}_{H4(t)}} + \mathbf{A}_{IC(t)}\ {_C\mathbf{r}_{H4C1(t)}}\,, \tag{5.6}$$

where $_C\mathbf{r}_{H4C1(t)}$ is the relative position of the racebike on the racetrack.

The Racebike Angular Velocity Vector The racebike angular velocity vector can be calculated with reference to Eq. 3.10 from the Euler parameters, just that

$$\boldsymbol{\omega}_{IC} = \left\{\omega_{xC} \quad \omega_{yC} \quad \omega_{zC}\right\}^T = 2\,\mathbf{L}_{IC(\mathbf{p}_{EIC})}\,\dot{\mathbf{p}}_{EIC}\,. \tag{5.7}$$

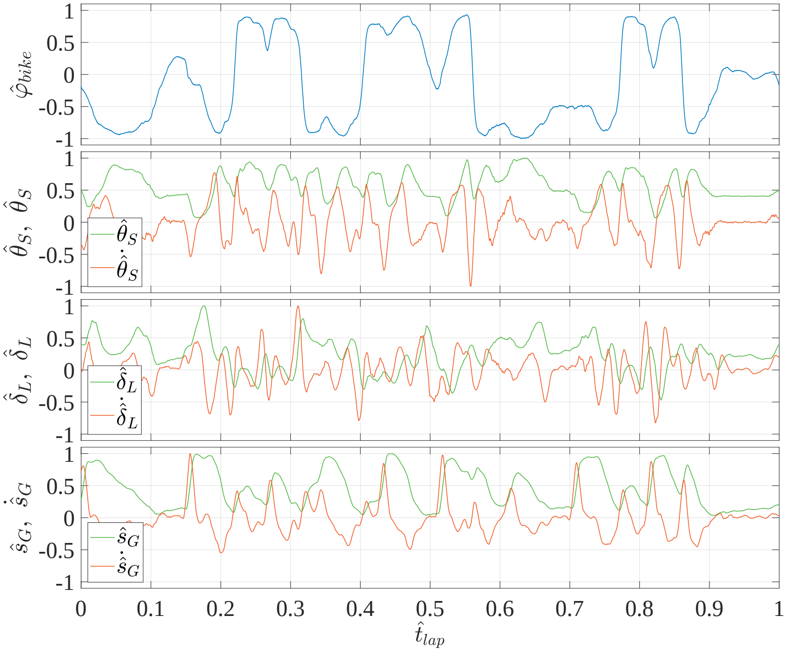

Figure 5.9: Normalized, internal racebike state quantities for the representative race lap.

The angular velocity components are normalized with the maximum magnitude of the vector, just that

$$\hat{\omega}_{iC} = \frac{\omega_{iC}}{max(|\boldsymbol{\omega}_{IC}|)} \quad \text{for} \quad i = x, y, z\,. \tag{5.8}$$

The lower subfigure in Fig. 5.10 shows the three normalized angular velocity components and the normalized lean angle signal. The plot shows mainly leaning movements around the x-axis. The y- and z-components are comparable small, but nevertheless meaningful as they are influenced strongly by relative movements of the racebike bodies.

The Absolute Racebike Velocity Vector The absolute velocity vector of the racebike with reference to Eq. 3.11 is denoted as

$$_I\mathbf{v}_C = \begin{Bmatrix} u_C & v_C & w_C \end{Bmatrix}^T = {}_I\mathbf{v}_{H4} + \mathbf{A}_{IC}\big({}_C\mathbf{v}_{H4C1} + \boldsymbol{\omega}_{IC} \times {}_I\mathbf{r}_{H4C1}\big)\,. \tag{5.9}$$

The relative velocity vector ${}_C\mathbf{v}_{H4C1}$ is the time derivative of the relative position vector ${}_C\mathbf{r}_{H4C1}$. The velocity components are normalized with the maximum magnitude of the vector, just that

$$ {}_I\hat{v}_{Ci} = \frac{v_{Ci}}{max(|{}_I\mathbf{v}_C|)} \quad \text{for} \quad i = x, y, z\,. \tag{5.10}$$

Fig. 5.10 shows the reference bike speed in the upper subfigure and the three velocity components in the middle subfigure. The y-component of the velocity vector is similar to the bike speed in the last part of the lap ($\hat{t}_{Lap} = 0.9 \cdots 1$), as the orientation of the inertial frame of reference axis goes into the direction of the backstraight in riding direction – counter clockwise. The z-velocity component is relatively small compared to the x- and y-components. Therefore, the z-velocity component is displayed with a scaling factor of 10.

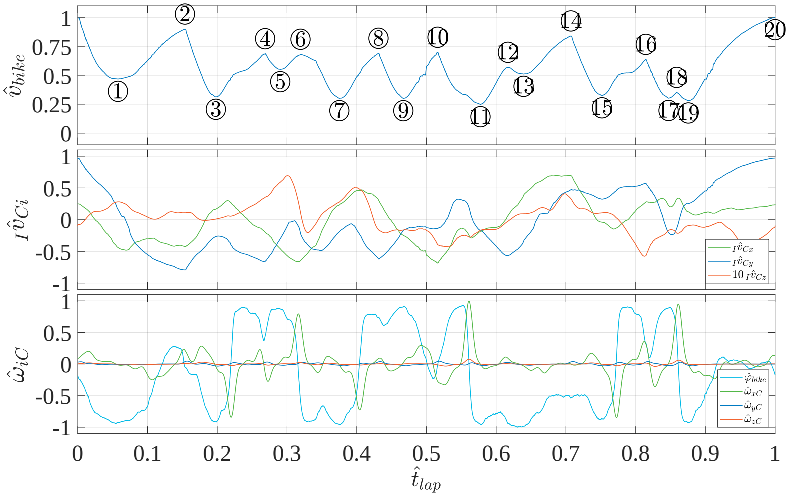

Figure 5.10: Normalized, absolute racebike translational and angular velocity components for the representative race lap.

The Absolute Racebike Acceleration The acceleration vector of the racebike is calculated with reference to Eq. 3.13. Fig. 5.11 shows the translational and angular acceleration components of the racebike. The upper subfigure shows the magnitude of the acceleration vector. The angular acceleration in the lower subfigure shows high values for the lean angle direction changes and moderate values for the y- and z-angular accelerations.

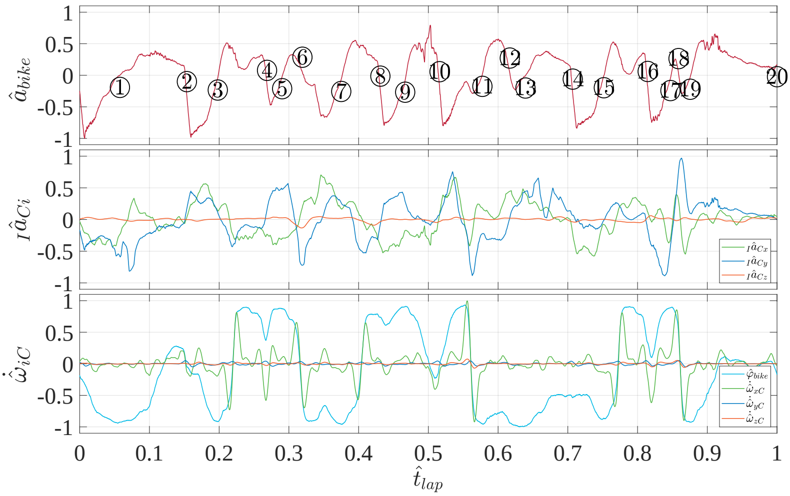

Figure 5.11: Normalized, absolute racebike acceleration quantities for the representative race lap.

Wheel Slip Calculation The local wheel slip quantities in the tire contact points are calculated with reference to section 3.4.2. Fig. 5.12 shows the racebike speed and the normalized engine speed in the upper subfigure. The lower subfigure shows the rear wheel slip and the normalized and scaled rear wheel drive torque. The figure shows drive slip values of up to 0.1 (10%) and brake slip values of up to $-0.2\,(-20\%)$. In the last part of the lap ($\hat{t}_{Lap} = 0.9 \cdots 1$), the acceleration on the backstraight, the drive slip has high values in the beginning when the maximum torque is applied, and then settles down to constant values around 0.04 (4%) until reaching the top speed at the end of the lap.

Wheelbase Calculation The wheelbase is calculated as the magnitude of the distance vector between the front and the rear wheel road-tire contact points, just that

$$l_{ref} = wb = \left|{}_I\mathbf{r}_{V4} - {}_I\mathbf{r}_{H4}\right| . \tag{5.11}$$

Fig. 5.13 shows the normalized reference length for the representative race lap. It has its minimum value in the straight-line acceleration at the end of the representative lap and larger values for the unsteady riding situations during the remaining lap.

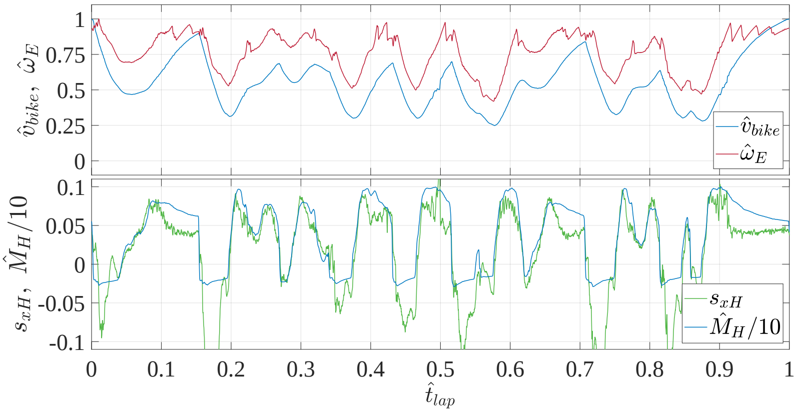

Figure 5.12: Normalized engine speed and bike speed. Rear wheel longitudinal slip and normalized drive torque at the rear wheel for the representative race lap.

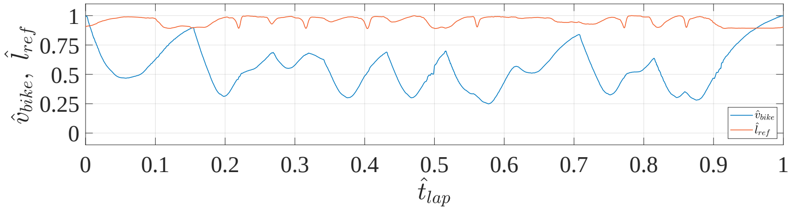

Figure 5.13: Normalized, reference length (wheelbase) for the representative race lap.

Racebike Measurement Table All raw measurements and all calculated variables are stored with a sampling rate of $100\,Hz$ in a MATLAB table. With a lap time of $113.52\,s$ the table has 11352 rows. The tabular presentation enables easy segmentation and further use of all measurement data and derived variables.

5.4 Measurement Data Segmentation

The physical racebike model from chapter 4 aims to cover as many influences as possible. However, there will be no specific racebike and rider model which is able to cover the whole highly dynamic range of motion of a racebike. Therefore, the prepared model data are split into meaningful segments. The segmentation is done by the following measurement and computational channels.

- racebike speed v_{bike},
- racebike lean angle φ_{bike},
- lean angle speed derivative χ,
- acceleration and braking segments.

Thresholds of the channels are furthermore used to exclude certain areas from the measurements.

The speed-lean angle plot for the representative lap of the Moto2 race is shown in Fig. 5.14. The plot shows the colour coded motion profiles for the acceleration and deceleration segments corresponding to Fig. 5.5. The circled numbers show the related starting points of acceleration and braking segments. The racebike is never at rest. The corresponding time shares are 59.3 % for acceleration and 40.7 % for deceleration. The main part of the acceleration segments starts from a negative, maximum lean angle. This corresponds to the counter clockwise racetrack with mostly left-hand corners. The acceleration segments starting from left-hand corners are displayed in Fig. 5.1 by the circled, uneven numbers 1, 3, 7, 11, 13,

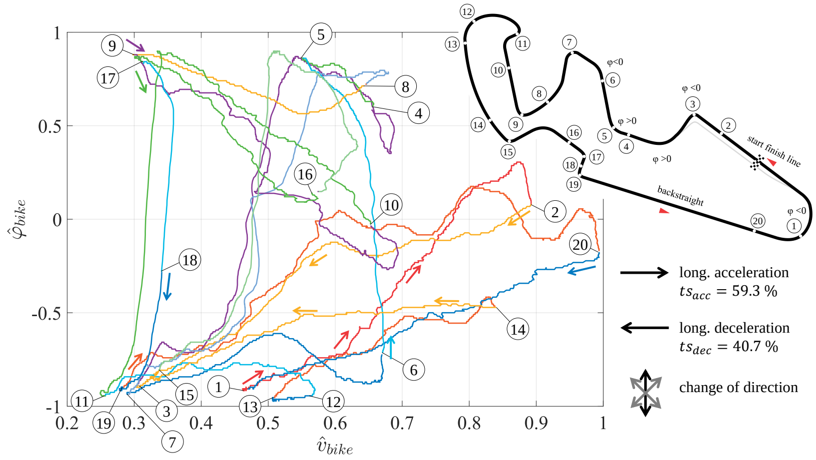

Figure 5.14: Normalized speed $\hat{v}_{bike}$ – normalized lean angle $\hat{\varphi}_{bike}$ plot for the representative lap.

15 and 19. Only the points 5, 9 and 17 indicate an acceleration starting from a right-hand corner.

The combined movements in longitudinal and lateral direction are analysed by the lean angle derivative after the racebike speed, denoted as

$$\chi = \frac{d\varphi}{dv} \quad \text{in} \quad \frac{rad}{m/s}. \tag{5.12}$$

The lean angle speed derivative χ is plotted in Fig. 5.15 together with the normalized lean angle and speed signal. The peaks of χ are related to direction changes, while a longitudinal acceleration at constant lean angle shows smooth, small values around zero. Smaller χ peaks are furthermore visible in braking regions. The calculated χ signal can be also visualized as the gradient in the speed–lean angle plot. The χ value helps in analysing the dynamics of a racebike.

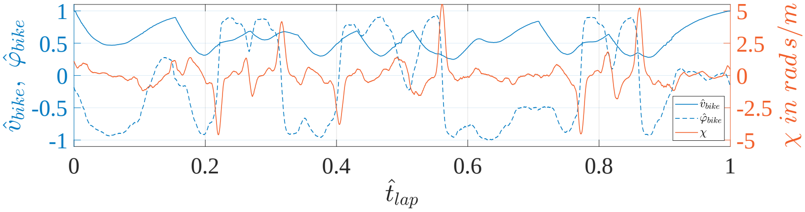

Figure 5.15: Normalized speed and lean angle, and chi signal for the whole representative race lap.

Looking for example at time $\hat{t}_{race} = 0.7$ in Fig. 5.15, the speed signal shows the racebike accelerating and decelerating. The normalized lean angle shows constant values of $\hat{\varphi}_{bike} \sim -0.5$. The derived χ value shows values close to zero, which means a pure longitudinal movement, although the racebike is in leaning conditions.

Chi Groups The value ranges of the magnitude of χ are used to subdivide the acceleration segments. The following three χ-groups are introduced and displayed in Fig. 5.16.

Table 5.2: Chi groups with value ranges, descriptions, interpretations, and the link to figures with corresponding riding situations.

group	$\|\chi\|$	description	interpretation
a	$0 \cdots 0.3$	acceleration segments with little or no change of the lean angle	longitudinal dynamics at constant lean angles; see Fig. 2.8 d & e
b	$0.3 \cdots 1$	moderate lean angle changes during acceleration	lifting up the bike from maximum lean angle into an upright position; see Fig. 2.8 c
c	$1 \cdots \infty$	rapid changes of the lean angle during acceleration	flipping of the racebike; see Fig. 2.8 b & f

The time shares of the single groups for the acceleration segments are shown in Fig. 5.16.

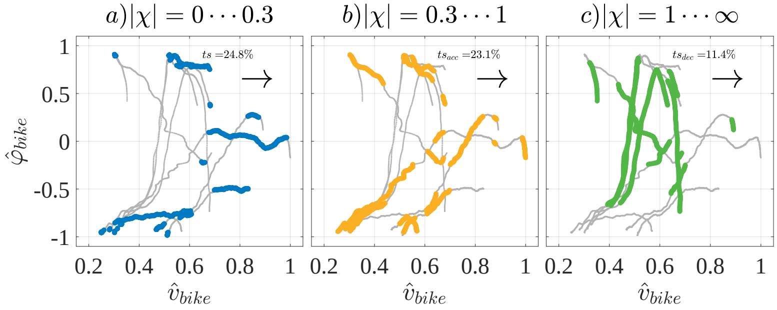

Figure 5.16: Speed–lean angle plot for acceleration segments with three groups a, b and c. Showing small, moderate, and rapid lean angle changes during acceleration.

Absolute Lean Angle Subdivision The χ criterion segmentation from the previous sections, however, does not provide information about the absolute lean angle position. This can be easily seen in Fig. 5.16 a. The subplot shows segments with minor lean angle changes during acceleration at different lean angles. Therefore, the measurement data are subdivided into three absolute lean angle groups:

- Index 1 for: $|\varphi_{bike}| < 20°$,
- Index 2 for: $20° < |\varphi_{bike}| < 40°$ and
- Index 3 for: $40° < |\varphi_{bike}|$.

With this, the three χ subgroups are further divided into the absolute lean angle groups. The resulting, 9 riding segments ($i_{1,2,3}$ for $i = a, b, c$) are shown in Fig. 5.17. The left subfigure shows steady lean angle riding situations. These segments can be used for the analysis of the racebike acceleration performance at different constant lean angles. The chi subgroups b and c are mainly driven by lean angle changes from left to right maximum lean angles or from maximum lean angles to zero. For this groups, the absolute lean angle subdivision does not give much added value.

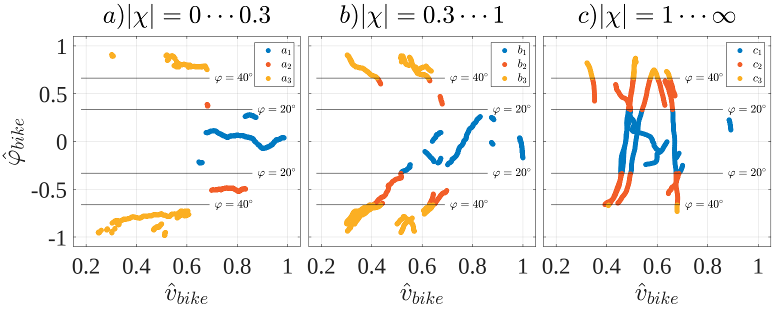

Figure 5.17: Subdivided chi acceleration segments into lean angle subgroups with the shown limits $i_1 < 20° < i_2 < 40° < i_3$ (for $i = a \cdots c$).

5.5 Riding Segments for Derivation of Aerodynamic Racebike Characteristics

The final assessment of the riding segments for the derivation of the aerodynamic racebike characteristics was carried out with the following criteria.

- Racebike acceleration $a_{bike} > 0\,m/s^2$.
- Racebike speed $v_{bike} > 30\,m/s$.

- Magnitude of lean angle – speed derivative, $|\chi| < 1.3\, rad\, s/m$. This criterion excludes the rapid lean angle changes which are mainly caused by the rider.

This value range covers 75% of the acceleration time shares. The corresponding time shares of the racebike speed, the lean angle, and the lean angle – speed derivative is visualized in Fig. 5.18 by the filled areas. Fig. 5.19 shows the riding segments within the criteria ranges in the Aragon track map. The chosen riding segments covers the two long straights:

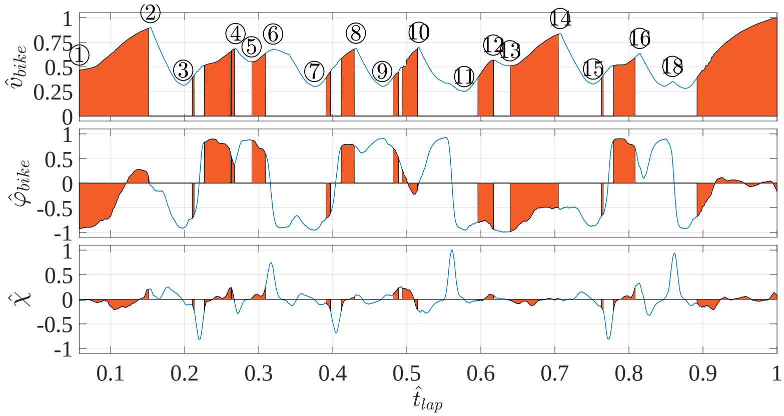

Figure 5.18: Chosen riding segments. The filled areas mark the regions of the racebike speed, lean angle, and lean angle - speed derivative which are inside the defined criteria.

- the start-finish line (points $1 \cdots 2$) and
- the backstraight (points $19 \cdots 20$).

It furthermore covers the shorter, straight segments like between points $9 \cdots 10$ as well as the long-drawn curves where the racebike is accelerating.

5.6 Straight-Line Acceleration Segments

The two longest acceleration segments are described and compared in more detail below. Fig. 5.20 shows the speed-lean angle plot for these acceleration segments. It is interesting to see that although the corner radius in point 1 is much bigger than in point 19, the lifting of the racebike from high lean angles is done over a

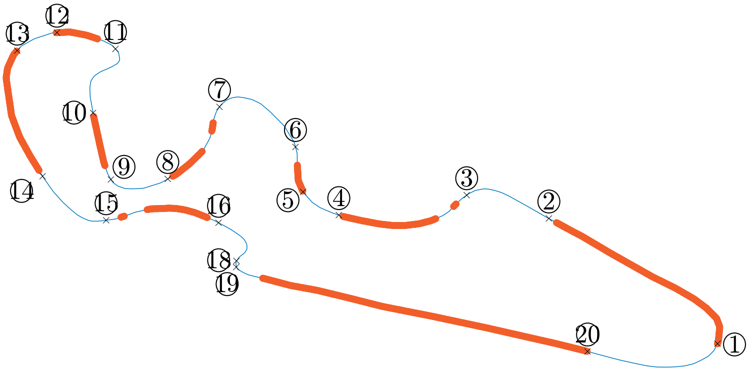

Figure 5.19: Chosen riding segments. The thick orange line indicates the chosen riding segments on the racetrack map.

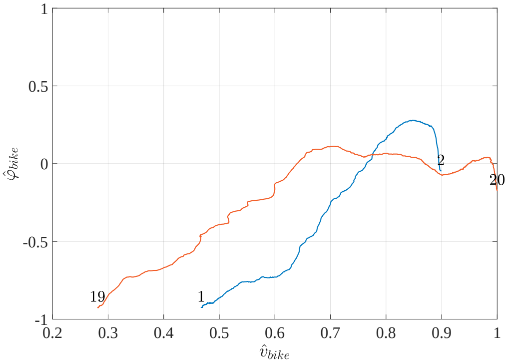

Figure 5.20: Normalized speed $\hat{v}_{bike}$ – normalized lean angle $\hat{\varphi}_{bike}$ plot for the two longest acceleration segments.

similar speed range – both have similar chi values in the beginning of the segment ($\chi \sim -0.3$).

Start-Finish Line (Points 1–2) Fig. 5.21 shows a short section of constant speed in the beginning. In this area the racebike is under a high lean angle. The front fork is compressed half way down, the rear shock is nearly fully compressed. For completeness, the brake is not actuated over the whole acceleration segment.

At $\hat{s}_{seg} \sim 0.1$ the rider opens the throttle. The racebike accelerates and both the front fork and the rear shock expand. The bike is still under a high lean angle. The area of $\hat{s}_{seg} \sim 0.2$ shows the rider steering. Beginning from $\hat{s}_{seg} \sim 0.3$ the rider lifts the bike up into an upright position. The front fork and the rear suspension strokes settle to a constant level over the last part of the acceleration segment. The figure illustrates once again that there are practically no straight riding situations for a racebike. An interesting fact is that the rider is already beginning to lean the bike before start braking.

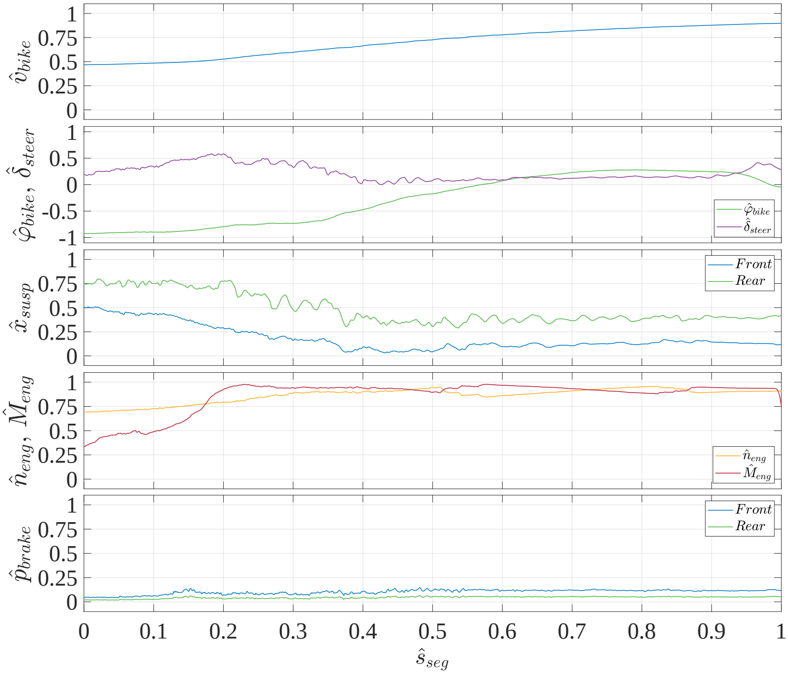

Figure 5.21: Measurement readings of the acceleration segment between points 1 and 2 – start-finish line.

Backstraight (Points 19–20) The second acceleration segment starts out of a tight curve onto the longest straight of the racetrack. The racebikes accelerates from a low speed and reaches the top speed of the whole lap at the end of this segment. The lean angle is close to zero over the largest part of the segment. This

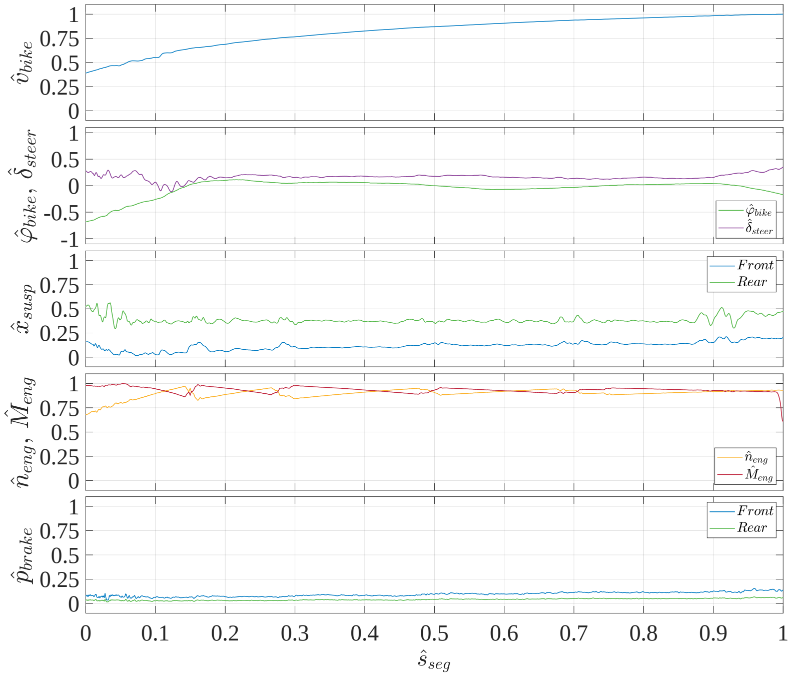

Figure 5.22: Measurement readings of the acceleration segment between points 19 and 20 – backstraight.

segment is most likely to be quasi-stationary, at least from $\hat{s}_{seg} \sim 0.2$ onwards.

Both acceleration segments will be used at the end of the next chapter to show the direct comparison with literature data to emphasize the soundness of the results.

Chapter 6

Results and Discussion

The aerodynamic characteristics are calculated with reference to chapter 4 for the prepared and segmented measurement data from chapter 5.

6.1 Calculated AIM Forces and Moments

The AIM forces and moments can be calculated for the complete representative lap with reference to Eqs. 4.48 and 4.49. The forces and moments are presented with reference to Fig. 3.4 in the moving racetrack patch axis system, indicate by p. In this axis system the x-direction is the direction of motion. The y-direction is the lateral motion, and the z-direction is the vertical movement. The calculated, normalized AIM forces and moments are shown in Fig. 6.1 together with the normalized bike speed and lean angle signal for the representative lap.

Forces The AIM force in x-direction consists, among other influences, of the drag resistance force (= acting against the direction of motion). Therefore, the x-force is negative over the largest range of the lap. Some positive values of the x-force are related to braking manoeuvre with a weight transfer of the rider. The force in z-direction shows negative values, which means a downward pointing force. The side force in y-direction shows a direct correspondence with the change of direction from the lean angle signal. It is assumed that the large y-force deflections are caused by the shifting of the rider's weight during changes in lean angle. A good check of the side force validity is the fact, that the side force is zero for the zero lean angle part at the end of the representative lap. This area is a straight line, where the racebike is in upright position.

Moments The lower subplot in Fig. 6.1 shows a dominating roll moment (x-moment) characteristic. The yaw moment (z-moment) and the pitch moment

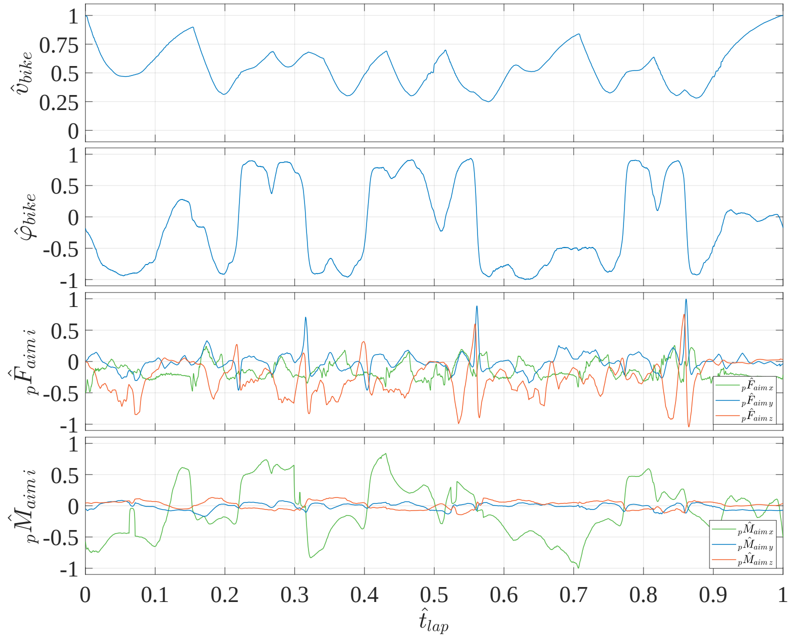

Figure 6.1: Normalized, AIM force and moment characteristics for the representative race lap.

(y-moment) show only small magnitudes in this overall picture.

Dimensionless Coefficients With reference to Eq. 4.50, the dimensionless force and moment coefficients are calculated from the AIM forces and moments. The following sections focus on the x-force. The x-force coefficient is used in the following as drag coefficient.

6.2 Drag Coefficient vs. Racebike Speed

The derived drag coefficients ${}_pc_D$ are displayed for the three χ subgroups a, b and c in Fig. 6.2 against the normalized racebike speed $\hat{v}_{bike}$. The subfigures show the derived raw data and a user defined regression curve of the form

$$ {}_{p}c_D = d + k\, e^{b\, v_{bike}}, \tag{6.1} $$

where k is a scale for the exponential function, b is a measure for the sharpness of the exponential function and d marks the saturation value of the regression curve. In other words, this is the constant drag coefficient part (${}_{p}c_{D\,const} = d$). The coefficient of determination of the regression curve R^2 is displayed in the subfigures as statistical measure of how close the data are fitted to the user defined regression curve. The high R^2 values indicate a good fit of the chosen regression curve.

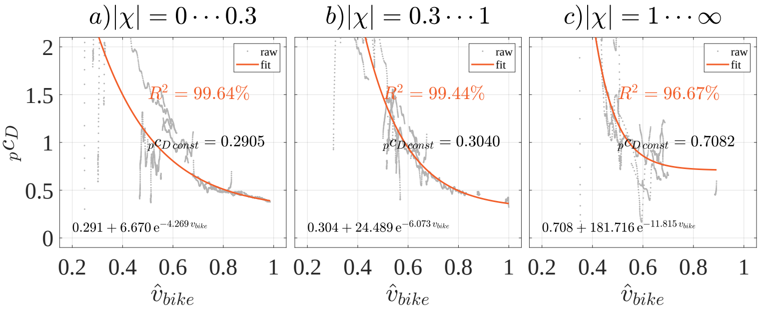

Figure 6.2: Drag coefficients $_{p}c_D$ vs. reference racebike speed v_{bike} for the χ acceleration subgroups a, b and c.

The results shown contradict the widely used assumption, that the drag coefficient is constant and independent of the racebike speed. The reasons for the speed dependency shown here are multifaceted and a superimposition of several effects. Known or already discussed effects are:

- Reynolds number effects with reference to Fig. 3.9,
- higher drag area values for riding situations at lower speeds during cornering due to the rider in *hanging-off* positions,
- lower drag area for higher speeds due to the rider in aerodynamically optimal low drag position and
- much more, highly dynamic effects, which are not yet known or researched in detail.

6.3 Drag Coefficient vs. Racebike Lean Angle

Here and in the following, only acceleration segments are discussed. The calculated drag coefficients ${}_p c_D$ are displayed for the three χ subgroups a, b and c in Fig. 6.3 against the normalized lean angle $\hat{\varphi}_{bike}$. The subfigures show the derived raw data and a user defined regression curve of the form

$$ {}_p c_D = a\, e^{b\,\varphi_{bike}} + c\, e^{-b\,\varphi_{bike}}\,, \tag{6.2} $$

where a and c are scales of the exponential functions and b is the measure of the sharpness of the exponential functions. The sum of a and c for the case of zero lean angle $\varphi_{bike} = 0$ describes the drag coefficient ${}_p c_{D0}$, just that

$$ {}_p c_{D0} = {}_p c_{D(\varphi_{bike}=0)} = a + c\,. \tag{6.3} $$

The drag coefficient for zero lean angles ${}_p c_{D0}$ is displayed in the subfigures for the three χ subgroups. The drag coefficient characteristics against the racebike lean angle looks at first sight quadratic. The quadratic shape was not able to cover the asymmetric characteristics of the drag coefficient in a sufficient way. An asymmetric drag characteristic is the result of a non-symmetric racebike due to packaging reasons and due to a never fully symmetrical rider behaviour in left and right-hand corners. Additionally, the non-aerodynamic effects of the AIM force can be responsible for the shown characteristics. The lean angle – drag coefficient plots show a high coefficient of determination R^2 for the chi group a and c. A closer look at the raw data nevertheless shows a large scatter of values, which is why the high coefficient of determination is somewhat misleading. For chi group

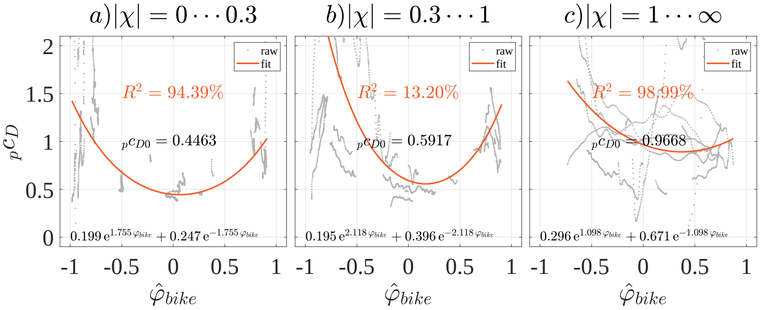

Figure 6.3: Drag coefficients ${}_p c_D$ vs. racebike lean angle φ_{bike} for the χ acceleration subgroups a, b and c.

b, the regression curve was not able to cover the drag characteristics. The reasons therefore are superimposed effects of rider movements and racebike speeds.

Therefore, the regression curve with reference to Eq. 6.2 cannot cover the drag coefficient – lean angle dependency for all single chi groups. For a more accurate modelling, the measurement data must be further segmented and subdivided.

6.4 Drag Coefficient for Chi and Lean Angle Subgroups

The drag coefficients are analysed for the 9 riding segments from Fig. 5.17. The corresponding drag coefficients are displayed in Fig. 6.4 against the normalized racebike speed. The regression curves are based on Eq. 6.1. To recap, the letters denote the χ groups (a, b, c), the indices $(1, 2, 3)$ denote the absolute lean angle ranges.

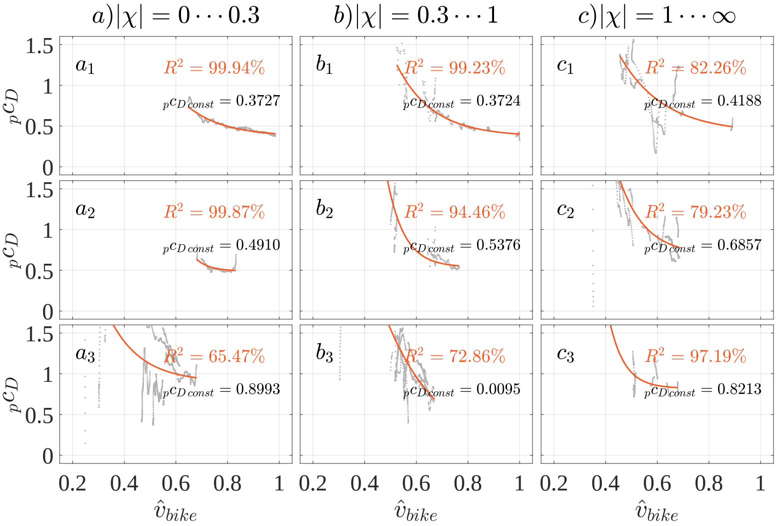

Figure 6.4: Drag coefficients $_pc_D$ vs. reference racebike speed v_∞ for the χ acceleration subgroups a, b and c.

- Riding segments a_1, b_1 and c_1 show independent of the χ range a high degree of certainty and similar saturation values $_pc_{D0}$. In this small lean angle range (index 1), the dynamic of the racebike is mainly the longitudinal dynamic. In any case, the dependence of the drag coefficient on the speed, is also evident here.

- The medium lean angle range case for small χ values a_2 shows a mainly constant drag coefficient and therefore, a good coefficient of determination.
- The other subgroups show high drag coefficients for low velocities and small or no saturation areas. This implies, that the dynamic in this riding segments is high, and that the rider movement has a major effect in these segments.

6.5 Force and Moment Coefficients for Acceleration Riding Segments

The detailed analysis of the drag coefficient in the previous sections showed, that there are partially meaningful relations to the racebike speed and the lean angle. No segmentation and modelling of the drag coefficients could present a satisfactory picture for the overall acceleration segments.

Based on the conclusions of the previous segmentation, the following criteria were used for the final modelling of the acceleration segments with reference to section 5.5. As a reminder the segmentation criteria are:

- $a_{bike} > 0\,m/s^2$
- $v_{bike} > 30\,m/s$
- $|\chi| < 1.3\,rad\,s/m$

With this, the aerodynamic force and moment coefficients for the selected racedata set are calculated. The results are presented as function of the racebike lean angle in Fig. 6.5.

The curves in the single subfigures show the regression curves with the related measure of determination R^2. After careful examination of various types of regression curves, three types have emerged as particularly suitable to cover the lean angle characteristics of all six aerodynamic coefficients.

The **lean angle force** characteristics are represented by a user-defined function, written as

$$c_f = a\,e^{b\varphi_{bike}} + c\,e^{-b\varphi_{bike}} \quad \text{for} \quad f = D, Y, L\,, \tag{6.4}$$

where a and c are scales of the exponential functions and b is the measure of the sharpness of the exponential functions.

The **lean angle roll- and pitch-moment** characteristics is represented by a third order *Polynom* written as

$$c_m = p_1\,\varphi_{bike}^3 + p_2\,\varphi_{bike}^2 + p_3\,\varphi_{bike} + p_4 \quad \text{for} \quad m = \mathcal{L}, \mathcal{M}\,, \tag{6.5}$$

where p_1, p_2, p_3 and p_4 are the coefficients of the polynom.

The **lean angle yaw-moment** characteristics is represented by a linear regression curve written as

$$c_m = p_1 + p_2\,\varphi_{bike} \quad \text{for} \quad m = \mathcal{N}\,, \tag{6.6}$$

where p_1, p_2 are the coefficients of the curve.

The complete set of the parameters for the aerodynamic force and moment characteristics is given in Appendix B. A detailed discussion of the single aerodynamic force and moment coefficients from Fig. 6.5 is given in the following paragraphs.

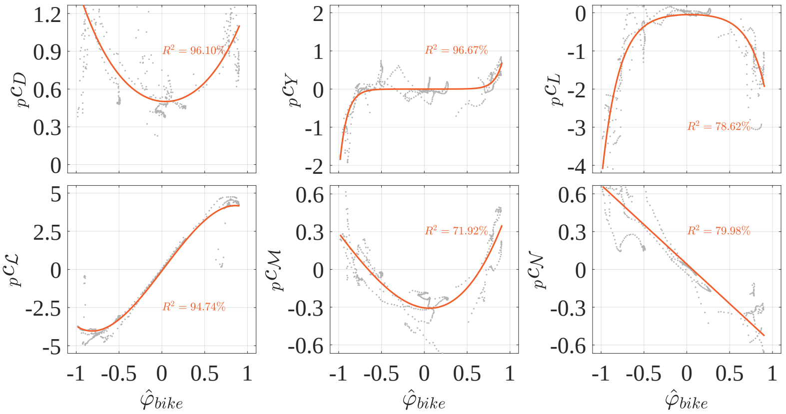

Figure 6.5: Aerodynamic force and moment coefficients vs. racebike lean angle for the defined acceleration segments.

Drag Coefficient ($_pc_D$) The drag coefficient characteristics shows a high coefficient of determination $R^2 = 96.1\%$ for the chosen riding segment. For the racebike in upright position, the drag coefficient from the regression curve shows minimum values of $_pc_D = 0.5020$. Looking at the raw calculated drag coefficients, the drag coefficient for zero lean angles is somewhat smaller. This region corresponds to subplot a_1 in Fig. 6.3. Considering the speed dependency from there, the minimum drag coefficient for small lean angles is $_pc_D = 0.3727$.

For higher lean angles, the drag coefficient reaches values of up to ${}_pc_D = 1.2$ for maximum lean angles. The calculated raw data show peaks at maximum lean angles of 1.5 and higher. A plausibility check of the high drag coefficients is made in paragraph 6.6.

Side Force Coefficient (${}_pc_Y$) The side force coefficient shows a flat characteristic for small lean angles and a sharp increase towards maximum lean angles. The characteristics is asymmetric showing positive side forces for positive lean angles and vice versa, like expected.

Lift Coefficient (${}_pc_L$) The lift coefficient is zero or negative over the whole lean angle range, which would mean a downforce in the aerodynamic context. For the racebike in upright position $\varphi \sim 0$, the overall lift coefficient is close to zero. This fits together with the experience of the author.

For higher lean angles, the lift coefficient reaches high values of up to -4. Lift, or downforce coefficients with a magnitude of $2 \cdots 4$ are not explainable by known aerodynamic mechanisms. Therefore, it is suspected that the high downforce coefficients are related to center of gravity and moment of inertia changes due to the rider in cornering situations.

Roll Moment Coefficient (${}_pc_{\mathcal{L}}$) The roll moment coefficient characteristics shows a close to linear behaviour over a wide lean angle range between $-0.5 < \hat{\varphi}_{bike} < 0.5$. For larger lean angles, the roll moment characteristics flatten out, reaching a maximum value of ${}_pc_{\mathcal{L}} = \pm 4$ at normalized lean angles of $\hat{\varphi}_{bike} = \pm 0.75$. The roll moment at higher lean angles is a result of the rider in *hanging-off* and the related aerodynamic, mass and inertial forces.

Pitch Moment Coefficient (${}_pc_{\mathcal{M}}$) The pitch moment coefficient is next to the drag and the lift force the important measure for the longitudinal racebike dynamics. The pitch moment is negative for small lean angles and positive for higher lean angles, crossing zero at lean angle values of $\varphi \sim 45°$.

- For small lean angles, the pitch moment is acting as a backward rotating moment which tends to lift the racebike at the front.

- For higher lean angles, the pitch moment is acting as a forward rotating moment which tends to press the front of the racebike down.

The pitch moment characteristics is close to symmetric with respect to the lean angle.

Yaw Moment Coefficient ($_pc_\mathcal{N}$) The yaw moment characteristics shows a linear behaviour over the whole lean angle range. For positive lean angles, the yaw moment shows negative values. Positive lean angles indicate a right-hand corner. Looking from top onto a riding situation in a right-hand corner, a negative yaw moment is acting as a left turning moment. This means, the yaw moment is trying to rotate the racebike out of the corner. The small offset of the regression line is caused by the unequal weighting of left- and right-hand corners.

6.6 Straight-Line Acceleration Drag Areas

For a final validation of the results with literature the straight-line acceleration segments from section 5.6 are used. Fig. 6.6 shows drag coefficients plotted against the racebike lean angle. The two solid lines are the derived drag coefficients from the AIM methodology for the two longest acceleration segments.

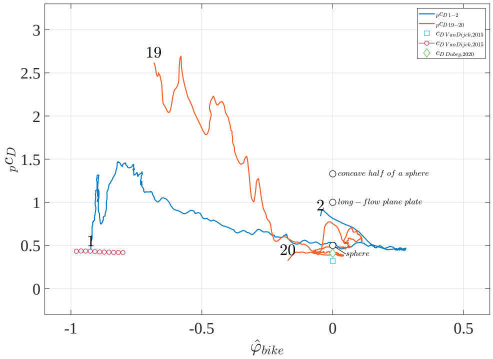

Figure 6.6: Aerodynamic drag coefficient vs. racebike lean angle. Calculated data for the start-finish line and the backstraight. Reference data from Van Dijk [13] and Dubey [16].

Comparison with Literature Results There is very few literature data available for racebike aerodynamic characteristics. Selected comparative measurements have been made for the drag area – reminder, in the present work, the drag coefficient is equivalent to the drag area. Van Dijk [13] did numerical flow simulations for the evaluation of aerodynamic forces on a racebike during cornering. The baseline simulations for the racebike in upright position at zero lean angle show a good match to the results from the AIM methodology at zero lean angle. Simulations carried out by Dubey [52] confirm valid drag coefficients for zero lean angle.

Comparison with Lean Angle Results Fig. 6.6 shows drag coefficients from numerical flow simulations for high lean angles carried out by Van Dijk [13]. There is a large discrepancy between the results. The difference comes through the fact that the flow simulations deliver just aerodynamics drag forces while the AIM derived drag coefficient also include the inertia and the mass of the rider and the racebike in the lean angle riding situations. The AIM methodology would just deliver pure aerodynamic forces if there would be no dynamic movement by the racebike or the rider itself.

Plausibility Check of the Drag Coefficient Taking the worst-case shape of a body, a cross-flow plane plate (shown in Fig. 3.7) or the concave half of a sphere, the theoretical drag coefficient is between 1 and 1.33, respectively. The projected area of a racebike with rider is between $0.5\,m^2$ for the rider in top speed position and up to $1\,m^2$ for the racebike rider combination in *hanging-off* or braking situations. Thus, the theoretical achievable drag areas $c_D\,A_x$ for a racebike rider combination are between $0.5 \cdots 1.33\,m^2$.

With the defined reference area of $1\,m^2$ for the analysis, the presented drag coefficients ${}_pc_D$ can be also interpreted as drag area. Therefore, the initial statement, that the high drag coefficient values are related to rider movements and changed geometry shapes can be confirmed with the values of the theoretically achievable drag coefficients. To recap, the individual components included in the here calculated drag coefficient are:

- the drag coefficient itself,
- the projected area,
- the center of gravity change due to rider movements and
- the change of the moment of inertia due to rider movements.

Although the effects cannot be resolved in detail, the presented drag coefficients are plausible based on the above explanations.

In summary it can be said that the AIM methodology shows a good match with literature results for zero lean angle case. For higher lean angles, the dynamic of the racebike and rider itself does not allow a direct comparison.

Chapter 7

Conclusions and Outlook

Within the framework of the thesis, a physical racebike model was created. The model was used to determine aerodynamic forces and moments in combination with mass- and inertia changes due to the highly dynamic rider movements of the racebike. The analyses is based on real racetrack measurements of a complete Moto2 world championship race.

The new approach was able to show plausible aerodynamic characteristics for various racetrack segments and rider positions. The aerodynamic force and moment coefficients were presented as function of the racebike speed and lean angle.

The approach allows the assessment of aerodynamic characteristics and rider dynamics relative to the racebike from real racetrack riding situations. The initial stated *bike aero tool* (see Fig. 2.14 and Fig. 4.4) helps engineers in the aerodynamic development of racebikes:

- to **validate** CFD simulations and windtunnel tests against each other,
- to validate CFD simulations and windtunnel tests against racetrack measurements,
- to check the **plausibility** of racetrack measurements and
- to **monitor** and track the aerodynamic development progress.

The *bike aero tool* can do much more. It can be used as *bike aim tool* – AIM: Aerodynamic, Inertia, Mass – for the analysis of aerodynamics and rider dynamics of a racebike riding on a racetrack. The tool can help engineers in the development and on racetracks to analyse and understand highly dynamic riding situations on racetracks. Thus, it supports in the permanent development of the racebike and in the optimization for minimum lap time.

In the course of the work, the new size $\chi = d\varphi/dv$ was introduced, which proved to be particularly practical in the representation and segmentation of real-world racetrack riding situations. This quantity is a measure for the dynamic of the racebike. It helps in identifying situations like changes of direction or quasi-steady riding situations.

To get a deeper insight into the individual components of the aerodynamic forces and moments for future work, additional measurement parameters would be helpful. Information about the exact rider position and the resulting center of gravity and inertia change can be gathered with rider motion capturing systems. With this information an extended multibody model can be built up and used for an enhanced model approach.

Additional measurements of the upstream flow conditions on the racebike can be used to validate the influence of the environmental wind conditions on the aerodynamic characteristics of the racebike. Feichtinger [20] presented a novel approach for the direct upstream flow measurement on moving objects, which can be used for aerodynamic measurements on racebikes in the future.

A deeper understanding of the aerodynamics of a racebike and combined rider-bike dynamics will be a major task for future developments. The present work provides a model basis for this and supports the development of future innovative concepts in the field of motorcycle racing.

Bibliography

[1] E. Achenbach and E. Heinecke. On Vortex Shedding from Smooth and Rough Cylinders in the Range of Reynolds Numbers 6e3 to 5e6. *Journal of Fluid Mechanics*, 109:239–251, 1981.

[2] S. Ahmed, G. Ramm, and G. Faltin. Some Salient Features Of The Time-Averaged Ground Vehicle Wake. *SAE International Congress and Exposition*, page 34, 1984.

[3] J.R. Alembert. *Essai d'une nouvelle theorie de la résistance des fluides*, volume V. Opuscules mathematiques, Paris, 1752.

[4] I.Y. Bar-Itzhack. New method for extracting the quaternion from a rotation matrix. *Journal of Guidance, Control, and Dynamics*, 23(6):1085–1087, 2000.

[5] R.H. Bartels, J.C. Beatty, and B.A. Barsky. Bézier Curves. In *An Introduction to Splines for Use in Computer Graphics and Geometric Modelling*, chapter 10, pages 211–245. San Francisco, 1998.

[6] G.K. Batchelor. *The Theory of Homogeneous Turbulence.* Cambridge University Press, Cambridge, 1953.

[7] P.W. Bearman. Some Effects of Free-Stream Turbulence and the Presence of the Ground on the Flow around Bluff Bodies. In G. Sovran, editor, *Aerodynamic Drag Mechanisms of Bluff Bodies and Road Vehicles*, pages 95–127. Plenum Press, London, 1976.

[8] P.J. Blau. Amontons' Laws of Friction. In Q Jane Wang and Yip-Wah Chung, editors, *Encyclopedia of Tribology*, page 71. Springer US, Boston, MA, 2013.

[9] BMW Motorcycle. Upside-Down Fork. Available at https://www.bmwmotorcycles.com/en/discover/engineering/technology-detail/suspension/usd-fork.html#/section-even-more-technology-in-detail, 2020. Accessed on 23 June 2020.

[10] M.E. Browne. *Schaum's outline of theory and problems of physics for engineering and science.* McGraw Hill, New York, 1999.

[11] K.R. Cooper. Atmospheric Turbulence with Respect to Moving Ground Vehicles. *Journal of Wind Engineering and Industrial Aerodynamics*, 17(2):215–238, 1984.

[12] V. Cossalter. *Motorcycle Dynamics.* LULU, second edition, 2006.

[13] Tom Van Dijck. Computational Evaluation of Aerodynamic Forces on a Racing Motorcycle during High Speed Cornering. *SAE Technical Paper 2015-01-0097*, 2015.

[14] Dorna. Dorna Photos. Available at https://www.motogp.com/en/photos, 2019. Accessed on 22 December 2020.

[15] P. Drage, A. Gabriel, G. Lindbichler, T. Hörmann, G. Brenn, and W. Meile. Efficient Use of Computational Fluid Dynamics for the Aerodynamic Development Process in the Automotive Industry. *AIAA Journal*, 6735, 2008.

[16] Feng Dubei, Jin Xuwei, Ge Jinrong, and Yang Jizhong. Analysis of Vibration Propagation Law of Rail Transit Underpassing Large-Span Building Structure. *Lecture Notes in Mechanical Engineering*, 2:963–969, 2020.

[17] A. Eichberger, W. Hirschberg, and H.M. Waser. *VO Fahrzeugdynamik.* Graz University of Technology, Graz, 2017.

[18] G. Eiffel. *Recherches expérimentales sur la résistance de l'air exécutées à la tour Eiffel.* Nabu Press, 2012, Paris, 1910.

[19] C.S. Feichtinger. Aerodynamics of the TERA Fennek: CFD based Optimization of the Aerodynamics of a low fuel consumption Vehicle, Master Thesis, Graz University of Technology, 2010.

[20] C.S. Feichtinger. Vorrichtung zur Geschwindigkeitserfassung mit einer Kielsonde (patent submitted), A50263/2020, 2021.

[21] C.S. Feichtinger and P. Fischer. SAE 2020-01-06: Uncertainty Quantification of Motorcycle Racing Upstream Flow Conditions. *SAE Technical Papers*, 2020.

[22] C.S. Feichtinger and P. Fischer. Stochastic Sensitivity of External Impact Factors on the Straight-Line Performance of a Generic Motorbike. In *Advances in Dynamics of Vehicles on Roads and Tracks*, pages 1222–1229. 2020.

[23] C.S. Feichtinger and P. Fischer. SAE 2021-01-0372: Some Basic Investigations into the Principles of Race Bike Aerodynamics for Real-World Racetrack Scenarios. *SAE Technical Papers*, 2021.

[24] Y.C. Fung. Fluctuating Lift and Drag Acting on a Cylinder in a Flow at Supercritical Reynolds Numbers. *Journal of the Aerospace Sciences*, 27(11), 1960.

[25] G. Rill. TMeasy - Tire Model easy to use. Available at http://www.tmeasy.de/, 2018. Accessed on 11 April 2021.

[26] COESA Working Group. *US standard atmosphere, 1976.* NOAA, technical edition, 1976.

[27] N. Grün. Motorradaerodynamik. In T. Schütz, editor, *Hucho – Aerodynamik des Automobils*, pages 727–798. Springer Vieweg, Wiesbaden, 2013.

[28] H. Herwig. *Strömungsmechanik – Einführung in die Physik von technischen Strömungen.* Vieweg+Teubner Verlag, Wiesbaden, first edition, 2008.

[29] W Hirschberg. TMsimple : A Simple to Use Tyre Model. Technical report, Institute of Automotive Engineering, Graz University of Technology, Graz, 2009.

[30] S.F. Hoerner. *Fluid-Dynamic Drag.* Hoerner Fluid Dynamics, New York City, 1965.

[31] W.H. Hucho. *Aerodynamik der stumpfen Körper.* Vieweg und Sohn Verlagsgesellschaft, Braunschweig, first edition, 2002.

[32] Verein Deutscher Ingenieure. *VDI 2206:2004-06 Design methodology for mechatronic systems.* Beuth Verlag GmbH, 2004.

[33] W. Kamm, C. Schmid, and P. Riekert. Einfluss der Reichsautobahn auf die Gestaltung der Kraftfahrzeuge. *Automobiltechnische Zeitschrift*, 37:341–354, 1934.

[34] W. Klemperer. Luftwiderstandsuntersuchungen an Automodellen. *Zeitschrift Flugtechnische Motorluftschiffahrt*, 13:102–106, 1922.

[35] KTM Sportmotorcycle GmbH. KTM RC16 2019. Available at https://media.ktm.com/assetbank-ktm/action/viewHome, 2019. Accessed on 22 December 2020.

[36] C. Lanczos. *The Variational Principles of Mechanics*. Dover Publications Inc., Toronto, 1986.

[37] J.H. Lienhard. *Synopsis of lift, drag and vortex frequency data for rigid circular cylinders*. Washington State University, Washington, 1966.

[38] D. J. N. Limebeer and M. Massaro. *Dynamics and Optimal Control of Road Vehicles*. Oxford University Press, sep 2018.

[39] M. Andretti. Quote by Mario Andretti. Available at https://www.marioandretti.com, 2020. Accessed on 22 June 2020.

[40] MagentaGreen. According to MagentaGreen and construction plans by Colin Chapman, CC BY-SA 3.0. https://commons.wikimedia.org/w/index.php?curid=62595383, 2017. Accessed on 20 February 2021.

[41] MATLAB Symbolic Toolbox 2020a, 2020. The MathWorks, Natick, MA, USA.

[42] Merriam-Webster. Aerodynamics decription. Available at https://www.merriam-webster.com/dictionary/aerodynamics, 2020. Accessed on 04 April 2020.

[43] P.S. Newnham. *The Influence of Turbulence on the Aerodynamic Optimisation of Bluff Body Road Vehicles*. PhD thesis, Loughborogh University, 2007.

[44] I. Newton. *Philosophiae Naturalis Principia Mathematica*. London, book ii edition, 1726.

[45] P.E. Nikravesh. *Computer-aided analysis of mechanical systems*. Englewood Cliffs, New Jersey, 1988.

[46] A. Nitsche and W. Brunn. *Strömungsmesstechnik*. Springer Verlag, Berlin Heidelberg New York, second edition, 2006.

[47] OpenStreetMap. OpenStreetMap Foundation (OSMF). https://www.openstreetmap.org/, 2021. Accessed on 18 March 2021.

[48] Hans B. Pacejka. Motorcycle dynamics. *Tyre and Vehicle Dynamics*, pages 517–585, 2006.

[49] H. Parkus. *Mechanik der festen Körper*. Springer-Verlag, second edition, 2005.

[50] L. Piegl. *Fundamental Developments of Computer Aided Geometric Design*. Academic Press, San Diego, 1993.

[51] L. Prandtl and A. Betz. *Ergebnisse der Aerodynamischen Versuchsanstalt zu Göttingen - III. Lieferung.* 2010.

[52] B. T. Kannan Pujan Dubey, Malandkar Yash Pramod, Aravind Satheesh Kumar. Numerical simulation of flow over a racing motorbike using OpenFOAM®. In *AIP Conference Proceedings 2277*, 2020.

[53] G. Rill and T. Schaeffer. *Grundlagen und Methodik der Mehrkörpersimulation.* Springer Fachmedien Wiesbaden, Wiesbaden, 2017.

[54] B. Robins. *An account of the experiments, relating to the resistance of the air, exhibited at different times before the Royal Society, in the year 1746.* Mathematic edition, 1761.

[55] A. Roshko. *On the development of turbulent wakes from vortex streets.* California Institute of Technology, 1952.

[56] G. Shen and Q. Li. Research on Railway Vehicle Stability Control Utilizing Mass Inertia Method. *Lecture Notes in Mechanical Engineering*, 2:40–46, 2020.

[57] V. Strouhal. *Ueber eine besondere Art der Tonerregung, Annalen der Physik und Chemie.* Verlag von Johann Ambrosius Barth, Leipzig, 1878.

[58] Suzuki. Suzuki RG500. Available at https://selvedgeyard.com/2010/12/20/the-magnificent-seven-british-racing-legend-barry-sheene/, 1979. Accessed on 22 December 2020.

[59] The Editors of Encyclopaedia Britannica. Motorcycle racing. Available at https://www.britannica.com/sports/motorcycle-racing, 2015. Accessed on 06 October 2020.

[60] Triumph Moto2 engine. The Triumph Moto2™ 765CC triple engine. https://www.triumphmotorcycles.com/moto2/engine, 2021. Accessed on 20 March 2021.

[61] Vitko. Aerofoil Vitko TZ750a. Available at https://www.speedzilla.com/attachments/2706-aerofoil-viko-tz750a-jpg.23181/, 1977. Accessed on 22 December 2020.

[62] S. Wordley. On-road Turbulence. *SAE International Journal of Passenger Cars - Mechanical Systems*, 1(1):341–360, 2009.

List of Figures

List of Tables

X

Curricula Vitae

Christoph Simon Feichtinger

Gartenweg 12
4920 Schildorn, Austria

Phone: 0043 664 884 214 48
Email: c.feichtinger@windpuls.com
URL: https://www.windpuls.com

Born: May 15, 1984—Ried im Innkreis, Austria
Nationality: Austria

Areas of specialisation

Aerodynamics; Vehicle Dynamics; Windtunnel; Numerical Flow Simulation; Design; Racebikes; Data Analytics

Appointments held

2003–2004	Scheuch, Aurolzmünster
2010–2014	qpunkt, Graz
2014–2019	KTM Factory Racing, Munderfing
2019–now	Digitrans, Linz
2021–now	Windpuls, Linz

Education

1998–2003 Mechanical Engineering, Higher Technical School, Wels
2005–2010 Dipl.-Ing. in Mechanical Engineering, Graz University of Technology
2017–2021 PhD in Mechanical Engineering, Graz University of Technology

Certificates

2014 16.101x: Introduction to Aerodynamics – MIT (Massachusetts Institute of Technology) edx. Certificate ID number: 1b90d4f5140948d09d16decdb5e6b61d

Publications & talks

Journal articles

2020 Stochastic Sensitivity of External Impact Factors on the Straight-Line Performance of a Generic Motorbike. Advances in Dynamics of Vehicles on Roads and Tracks. pages 1222-1229. 2020

2020 SAE 2020-01-0667 Uncertainty Quantification of Motorcycle Racing Upstream Flow Conditions. SAE Technical Papers. 2020

2021 SAE 2021-01-0372 Some Basic Investigations into the Principles of Race Bike Aerodynamics for Real-World Racetrack Scenarios. SAE Technical Papers. 2021

Lectures

2016 Automotive Simulation World Congress & ANSYS Electronics Simulation Expo, Automated workflow for the drag reduction of racing motorcycles, Munich

2016 Ansys Conference & 11. CADFEM Austria Users' Meeting, Keynote: Automatisierter Workflow zur Bestimmung der aerodynamischen Eigenschaften von Motorrädern im Motorsport, Linz

2017 ÖVK Vortrag, KTM MOTOGP – Technik und Aerodynamik – Ready to Race, Graz

2019 ÖVK Vortrag, KTM MOTOGP – Technik und Aerodynamik – Ready to Race, Steyr

2021 SAE World Congress, Some Basic Investigations into the Principles of Race Bike Aerodynamics for Real-World Racetrack Scenarios, Virtual Event

Books

2010 Aerodynamics of the TERA Fennek: CFD based Optimization of the Aerodynamics of a low fuel consumption Vehicle, Master Thesis, Universtity of Technology, Graz, 2010

Appendix A

Motorcycle Model Parameter

The following paragraphs show the geometric, mass and inertia parameters for the six bodies of the racebike multibody model in SI Units.

Chassis (C) Parameters

Table A.1: Chassis (C) Parameters)

parameter	value	unit	parameter	value	unit
m_C	180	kg	κ_F	-22	°
Θ_{Cxx}	11	kgm^2	Θ_{Cxy}	0	kgm^2
Θ_{Cyy}	22	kgm^2	Θ_{Cyz}	0	kgm^2
Θ_{Czz}	15	kgm^2	Θ_{Czx}	-4	kgm^2
x_{C10}	0.102	m	z_{C10}	0.203	m
x_{C12}	0.542	m	z_{C12}	0.404	m

With κ_F as the steering head angle.

Swingarm (S) Parameters

Table A.2: Swingarm (S) Parameters)

parameter	value	unit	parameter	value	unit
m_S	8	kg	θ_{S0}	-12	°
Θ_{Sxx}	10	kgm^2	Θ_{Sxy}	0	kgm^2
Θ_{Syy}	20	kgm^2	Θ_{Syz}	0	kgm^2
Θ_{Szz}	10	kgm^2	Θ_{Szx}	0	kgm^2
x_{S10}	-0.202	m	z_{S10}	-0.050	m
x_{S12}	-0.570	m	z_{S12}	0.000	m

With θ_{S0} as the swingarm angle in static position.

Upper Front Assembly (L) Parameters

Table A.3: Upper Front Assembly (L) Parameters

parameter	value	unit	parameter	value	unit
m_L	5	kg	l_{G0}	0.135	m
Θ_{Lxx}	1.5	kgm^2	Θ_{Lxy}	0	kgm^2
Θ_{Lyy}	1.5	kgm^2	Θ_{Lyz}	0	kgm^2
Θ_{Lzz}	1	kgm^2	Θ_{Lzx}	0	kgm^2
x_{L10}	0.050	m	z_{L10}	-0.200	m
x_{L13}	0.050	m	z_{L13}	-0.580	m

With l_{G0} as the fully extended front fork length.

Lower Front Assembly (G) Parameters

Table A.4: Lower Front Assembly (G) Parameters

parameter	value	unit	parameter	value	unit
m_G	4	kg			
Θ_{Gxx}	1	kgm^2	Θ_{Gxy}	0	kgm^2
Θ_{Gyy}	1	kgm^2	Θ_{Gyz}	0	kgm^2
Θ_{Gzz}	0.5	kgm^2	Θ_{Gzx}	0	kgm^2
x_{L10}	0.025	m	z_{L10}	-0.020	m
x_{L12}	0.000	m	z_{L12}	-0.033	m

Rear Wheel (H) Parameters

Table A.5: Rear Wheel (H) Parameters

parameter	value	unit	parameter	value	unit
m_H	15	kg			
Θ_{Hxx}	0.2	kgm^2	Θ_{Hxy}	0	kgm^2
Θ_{Hyy}	0.5	kgm^2	Θ_{Hyz}	0	kgm^2
Θ_{Hzz}	0.2	kgm^2	Θ_{Hzx}	0	kgm^2
x_{H10}	0.000	m	z_{H10}	0.000	m
x_{H12}	0.000	m	z_{H12}	-0.215	m
x_{H23}	0.000	m	z_{H23}	-0.114	m

With the tire geometry of the Dunlop 200/75R17 Moto2.

Front Wheel (V) Parameters

Table A.6: Front Wheel (V) Parameters

parameter	value	unit	parameter	value	unit
m_V	12	kg			
Θ_{Vxx}	0.15	kgm^2	Θ_{Vxy}	0	kgm^2
Θ_{Vyy}	0.40	kgm^2	Θ_{Vyz}	0	kgm^2
Θ_{Vzz}	0.15	kgm^2	Θ_{Vzx}	0	kgm^2
x_{V10}	0.000	m	z_{V10}	0.000	m
x_{V12}	0.000	m	z_{V12}	-0.215	m
x_{V23}	0.000	m	z_{V23}	-0.082	m

With the tire geometry of the Dunlop 125/75R17 Moto2.

Appendix B

Aerodynamic Force and Moment Model Parameter

Model parameters for the aerodynamic force and moment coefficients from section 6.5 for segmentation criteria:

- $a_{bike} > 0\,m/s^2$
- $|\chi| < 1.3\,rad\,s/m$
- $v_{bike} > 30\,m/s$

Drag Coefficient

$$_{p}c_D = a\,\mathrm{e}^{b\,x} + c\,\mathrm{e}^{-b\,x} \tag{B.1}$$

$R^2 = 0.96104$
Coefficients (with 95% confidence bounds):
$a = 0.23403\ (0.23172,\ 0.23634)$
$b = 1.6511\ (1.6378,\ 1.6643)$
$c = 0.26795\ (0.26539,\ 0.2705)$

Side Force Coefficient

$$_{p}c_Y = a\,\mathrm{e}^{b\,x} + c\,\mathrm{e}^{-b\,x} \tag{B.2}$$

$R^2 = 0.96674$
Coefficients (with 95% confidence bounds):
$a = 1.9505e-05\ (1.6663e-05,\ 2.2347e-05)$
$b = 11.5619\ (11.3962,\ 11.7276)$
$c = -2.1464e-05\ (-2.4768e-05,\ -1.816e-05)$

Lift Force Coefficient

$$ {}_{p}c_{L} = a\,\mathrm{e}^{b\,x} + c\,\mathrm{e}^{-b\,x} \tag{B.3} $$

$R^2 = 0.78616$
Coefficients (with 95% confidence bounds):
$a = -0.0202\ (-0.022792,\ -0.017608)$
$b = 5.0371\ (4.8879,\ 5.1863)$
$c = -0.02892\ (-0.032709,\ -0.025131)$

Roll Moment Coefficient

$$ {}_{p}c_{\mathcal{N}} = p_1\,x^3 + p_2\,x^2 + p_3\,x + p_4 \tag{B.4} $$

$R^2 = 0.94742$
Coefficients (with 95% confidence bounds):
$p_1 = -3.5106\ (-3.69,\ -3.3312)$
$p_2 = 0.2424\ (0.17516,\ 0.30964)$
$p_3 = 7.3654\ (7.2473,\ 7.4836)$
$p_4 = -0.096583\ (-0.12916,\ -0.064007)$

Pitch Moment Coefficient

$$ {}_{p}c_{\mathcal{M}} = p_1\,x^3 + p_2\,x^2 + p_3\,x + p_4 \tag{B.5} $$

$R^2 = 0.71925$
Coefficients (with 95% confidence bounds):
$p_1 = 0.20366\ (0.17023,\ 0.23709)$
$p_2 = 0.7109\ (0.69837,\ 0.72343)$
$p_3 = -0.087883\ (-0.10991,\ -0.065856)$
$p_4 = -0.30586\ (-0.31193,\ -0.29979)$

Yaw Moment Coefficient

$$ {}_{p}c_{\mathcal{L}} = p_2 + p_1\,x \tag{B.6} $$

$R^2 = 0.79982$
Coefficients (with 95% confidence bounds):
$p_1 = -0.62749\ (-0.63629,\ -0.61869)$
$p_2 = 0.041773\ (0.036444,\ 0.047103)$

Appendix C

Upstream Flow Conditions on a Racetrack

A racebike on a racetrack is exposed to a variety of environmental conditions. The wind environment and the flow conditions induced by the wake areas of other riders on the racetrack. Therefore, the upstream flow conditions of a racebike are influenced by the same conditions. These conditions are mainly turbulent flow conditions which are subject to great fluctuations.

Turbulent Flow Regime For a turbulent wind field, respectively the turbulent flow regime, Batchelor [6] stated three principal difficulties by a solution to the problem of homogeneous turbulence:

- The three-dimensional character of the velocity field,
- The non-linearity of the equation of motion, and
- The random variation of the velocity and the need for statistical methods.

This leads to a higher effort for the modelling of a turbulent environment, compared to the modelling of a uniform wind field. Fig. C.1 shows the three-dimensional velocity components of a given fluid element B in a turbulent flow field. The most common approach for turbulent flow modelling is the so-called Reynolds decomposition, which splits the instantaneous flow variables into an averaged and a fluctuating component, written as

$$u = \bar{u} + u', \, v = \bar{v} + v', \, w = \bar{w} + w', \, p = \bar{p} + p' \, , \tag{C.1}$$

with the velocity components u, v, w in x, y and z direction. The first component is the averaged value, the second the fluctuating term. The derivatives of the

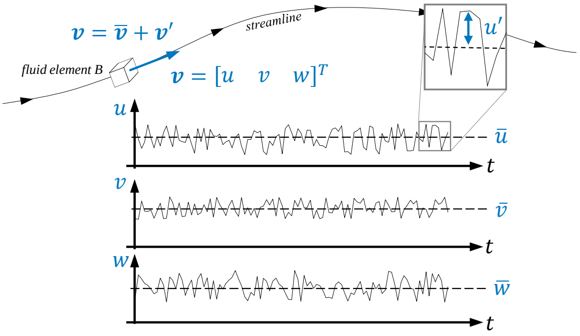

Figure C.1: Velocity components at a given point in a turbulent flow field with respect to Herwig [28].

fluctuating component lead to the *scale providing* quantities like the turbulent kinetic energy

$$k = \frac{1}{2}\overline{u'_k\, u'_k}\,, \tag{C.2}$$

and the turbulent energy dissipation, written as

$$\varepsilon = \nu\, \overline{\frac{\partial u'}{\partial x_k} \frac{\partial u'}{\partial x_k}}\,. \tag{C.3}$$

Both quantities are used as scale variables for the description of the turbulent flow field. The turbulent kinetic energy and the turbulent energy dissipation are used for the calculation of the turbulent velocity scale

$$\mathcal{U}_{turb} \approx \sqrt{k}\,, \tag{C.4}$$

and the turbulent length scale

$$\mathcal{L}_{turb} = \frac{\sqrt[3]{k}}{\varepsilon}\,, \tag{C.5}$$

respectively. Another *scale providing* quantity is the characteristic frequency, defined as

$$\omega_{turb} = \frac{\varepsilon}{k}\,. \tag{C.6}$$

Using this quantity, the turbulent length scale can be alternatively calculated by

$$\mathcal{L}_{turb} = \frac{\sqrt{k}}{\omega_{turb}}\,. \tag{C.7}$$

The turbulence intensity of the environmental wind field

$$Tu_{wind} = \frac{1}{|\mathbf{v}_{wind}|}\sqrt{\frac{2}{3}k}\,, \tag{C.8}$$

is a normalized turbulence quantity which describes the turbulent kinetic energy with reference to the magnitude of the oncoming wind speed $|\mathbf{v}_{wind}|$. For a general definition of the turbulence intensity the magnitude of the upstream flow vector is used as reference velocity as follows

$$Tu_{us} = \frac{1}{|\mathbf{v}_{us}|}\sqrt{\frac{2}{3}k}\,. \tag{C.9}$$

The turbulence intensity with reference to the upstream flow conditions Tu_{us} is therefore different compared to the turbulence intensity of the environmental wind field Tu_{wind}.

Turbulent Flow Field The turbulent flow field is three-dimensional, non-linear and has a random variation. Therefore, the flow field can be modelled for the complete three-dimensional operational domain using Taylors' hypothesis of 'frozen turbulence', mentioned by Cooper [11]. The wind velocity at a fixed point has components in x, y and z direction (see Fig. C.1) for the averaged wind vector and the fluctuation velocity components. The whole turbulent wind velocity vector is defined as

$$\mathbf{v}_{wind_i} = \overline{\mathbf{v}}_{wind_i} + \mathbf{v}'_{wind_i}\,, \tag{C.10}$$

with $\overline{\mathbf{v}}_{wind_i}$ as the averaged wind vector and $\mathbf{v}'_{wind_i}$ as the absolute value of the fluctuation velocity. The fluctuation velocity can be defined as

$$\mathbf{v}'_{wind_i} = 2\,\mathbf{v}'_{wind_{i(max)}}\left(LHS_i - \frac{1}{2}\right)\,, \tag{C.11}$$

with the maximum absolute value of the fluctuation velocity and the LHS-Function (Latin Hypercube Sampling) implemented in MATLAB. The LHS is a statistical method to generate near-random samples between 0 and 1. The fluctuating wind component is an absolute value, therefore 0.5 must be subtracted in Eq. C.11 to get a positive and negative fluctuating component. For each grid point in the turbulent flow domain the *scale providing* quantities can be calculated using equations C.2 to C.8. To understand the effects of turbulence, Bearman [7] proposed to differentiate between *passive* and *active* parts of the turbulence spectrum.

The *passive* parts are related to large-scale eddies, large compared to the size of the vehicle. The large-scale eddies have a *quasi-steady* effect on the aerodynamics as they change the magnitude and direction of the approaching wind.

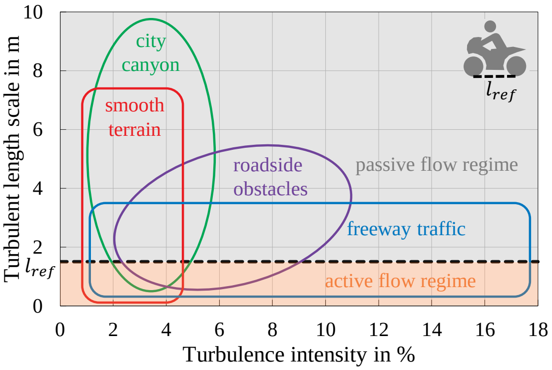

Figure C.2: Turbulent length scale versus turbulence intensity. The boxes show reference values from on-road turbulence measurements carried out by Wordley [62]. The dashed line shows the reference length l_{ref} of the racebike, which is the wheelbase.

The *active* parts represent the smaller scales of turbulence which can interact with the flow field directly, due to a high content of kinetic energy. Therefore, they have large influence on the overall flow as these high energy eddies may affect boundary layer separation and reattachments, like published by Newnham [43]. He showed drag coefficients over Reynolds numbers for different turbulence intensities, highlighting the effect on the critical Reynolds number. Fig. C.2 shows the turbulent length scale versus turbulence intensity with reference values for city canyon, smooth terrain, roadside obstacles and freeway traffic measured by Wordley [62]. Furthermore, it shows the wheelbase of the racebike as reference length. The reference length splits the turbulent flow regime into the *active* and *passive* parts.

Though there is a strong, known influence of the *active* parts and the corresponding critical Reynolds number they are not considered within the present thesis. A deeper insight into the effect of the upstream flow conditions is given by Feichtinger [22] and [21].

Monographic Series TU Graz

Reihe Fahrzeugtechnik

Vol. 1 Haymo Niederkofler
Analyse radselektiv eingreifender Fahrdynamikregelsysteme für die Anwendung in Elektromechanischen Corner-Modulen
2012
ISBN 978-3-85125-220-0

Vol. 2 Andrés Eduardo Rojas Rojas
Passenger Vehicles with In-Wheel Motors
2012
ISBN 978-3-85125-234-7

Vol. 3 Daniel Wallner
Experimental and Numerical Investigations on Brake Squeal
2013
ISBN 978-3-85125-269-9

Vol. 4 Alexander Harrich
CAD-basierte Methoden zur Unterstützung der Karosseriekonstruktion in der Konzeptphase
2015
ISBN 978-3-85125- 420-4

Vol. 5 Cornelia Lex
Maximum Tire-Road Friction Coefficient Estimation
2015
ISBN 978-3-85125-422-8

Vol. 6 Stefan Bernsteiner
Integration of Advanced Driver Assistance Systems on Full-Vehicle Level
2016
ISBN 978-3-85125-468-6

Monographic Series TU Graz

Reihe Fahrzeugtechnik

Vol. 7 Patrick Rossbacher
Beitrag integrierter Konzeptmodelle
zur virtuellen Gesamtfahrzeugentwicklung
in der frühen Entwurfsphase
2020
ISBN 978-3-85125-730-4

Vol. 8 Andreas Hackl
Enhanced Tyre Modelling for Vehicle
Dynamics Control Systems
2020
ISBN 978-3-85125-728-1

Vol. 9 Christoph Feichtinger
Racebike Dynamics
2021
ISBN 978-3-85125-860-8